Photodynamic and Photothermal Human Cancer Cell Killing Using Gold Nanoparticles

Thesis submitted in accordance with the requirements of the University of Liverpool for the degree of Doctor in Philosophy by:

Samantha Chadwick

September 2015

Acknowledgments

First and foremost, my appreciation and greatest thanks goes to my Ph.D. supervisors, Mathias Brust and Martin Volk. Over the last four years they have provided continual support, guidance, enthusiasm and have kept me positive when it felt like everything was failing! I have learned so much and I am truly grateful. Also, thank you to Martin for the simulation work that has contributed to this thesis.

Next, I would like to thank past, present and visiting members of the Brust group, I have met so many lovely people who have made the last few years lots of fun. A special thanks to my current group, not only for the encouragement and help over the last few months but for the fun evenings out and the laughter in the office! A special thank you to Dina Salah. I also couldn't have done this without my friends Jane, Helen and Hannah.

I would like to thank Ian Prior and everyone in physiology for all of their help over the last few years, especially Ali Beckett who made the stressful times in the EM unit quite enjoyable! I would also like to thank Mike Davidson, Simona Kalarova, Flavia Mesquita Cabrini, and Penny Livesey for their contributions to this thesis through their undergraduate research projects.

Finally, a huge thank you to my family, especially my Mum and Dad, I am so lucky to have your support and encouragement all of the time and to Karl, thank you for everything, especially over the last few months, I couldn't have done it without you!

Abstract

Cells from a human fibroblast cell line (HeLa) were used to explore the role of photothermal and photodynamic effects of laser irradiation using plasmonic gold nanoparticles. The two types of spherical gold nanoparticles used were (i) citrate-stabilised and (ii) peptide stabilised particles. These particles were prepared following standard protocols and characterised by a range of methods including TEM, UV-vis spectroscopy and dynamic centrugal sedimentation. Different sizes of particles were prepared and the effect of size was investigated. Cellular uptake of the nanoparticles prior to exposure to laser light was quantified by TEM and by ICP-AES. Cell cultures were exposed to a laser of a wavelength within the plasmon band of the gold nanoparticles (520 nm), and cell death was monitored by optical microscopy using the standard Trypan blue exclusion assay. The total energy transfer from the laser to the cell culture was estimated based on the extinction coefficient of the nanoparticles and also measured directly by UV-vis spectroscopy. Heating profiles for a range of laser intensities and exposure times were calculated. The temperature at which thermal cell death occurs was estimated by exposing the cells to a heated water bath and monitoring viability. Conditions were established to demarcate photothermal from photodynamic cell death, and a photodynamic mechanism was suggested based on the photochemical production of singlet oxygen. The plausibility of this mechanism was demonstrated by quantitative studies of singlet oxygen formation by laser irradiation of gold nanoparticles dispersed in water.

Contents Page

Abbreviations

AB	Antibody
EM	Electron Microscopy
EGFR	Epidermal Growth Factor
FDA	Food and Drug Administration
HER	Human Epidermal Recepetor
ICP-AES	Inductively Coupled Plasma Atomic Emission Spectroscopy
NP	Nanoparticle
NR	Nanorod
NIR	Near Infrared
OD	Optical Density
PDT	Photodynamic Therapy
PS	Photosensitizer
PTT	Photothermal Therapy
RT	Room Temperature
SPR	Surface Plasmon Resonance

Chapter 1

Introduction

Photodynamic therapy (PDT)[1, 2] offers a less invasive and more selective cancer treatment over traditional methods, such as, surgical removal of the tumour and chemotherapy, which suffer from multiple problems including tumour accessibility and collateral damage to healthy cells.

PDT involves a photosensitizer (PS) which is administered to the tumour site and then excited by a specific wavelength of light. Once excited to its triplet state, the PS transfers its energy to the surrounding oxygen yielding reactive oxygen species (ROS),[1] mainly, singlet oxygen ($^1O_2$), responsible for cytotoxicity.[3]

Oxygen ($^3\Sigma_g^-$) has two singlet excited states $^1\Delta_g$ and $^1\Sigma_g^+$. The $^1\Sigma_g^+$ state is very short lived as it relaxes to the lower energy singlet state, $^1\Delta_g$, which is the state normally referred to as $^1O_2$. Figure 1.1 shows the molecular orbital (MO) diagram of O_2 and $^1O_2$ ($^1\Delta_g$).

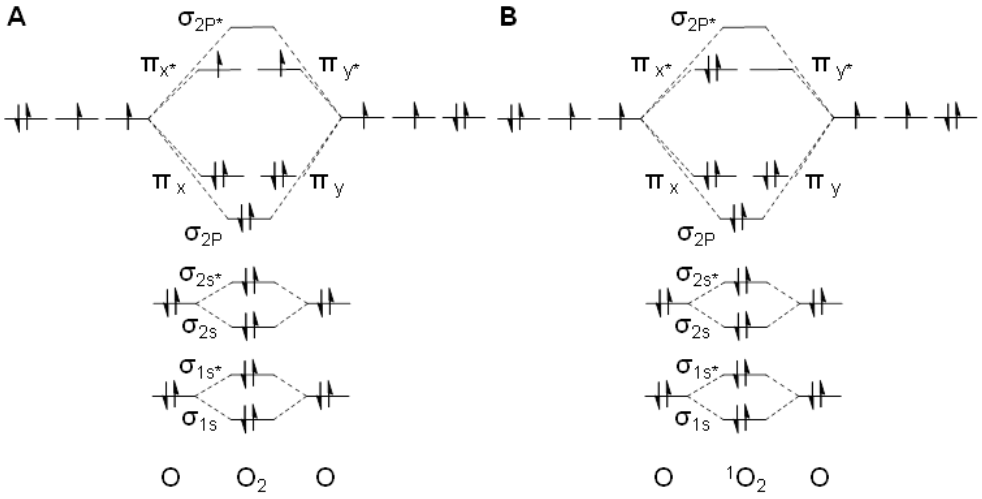

Figure 1.1: The MO's of oxygen A) in the triplet state ($^3\Sigma_g^-$) and B) in the singlet state ($^1\Delta_g$)[3]

The most commonly used PS are porphyrin based compounds.[4] The first Food and Drug Administration (FDA) approved PS was photofrin® (porfimer sodium) which is used to treat multiple cancers including bladder, lung and cervical.[4] The disadvantages of photofrin® which absorbs light at 632 nm are that it has a low absorption coefficient of *ca.* 3000 M^{-1} cm^{-1}, exists as complex mixtures of monomeric, dimeric, and oligomeric structures, and suffers from photobleaching. A second generation of PS has been developed including FDA approved Foscan® (meta-tetra(hydroxyphenyl)chlorine – m-THPC) used to treat neck and scalp cancer.[5] It absorbs light at 652 nm and has a higher absorption coeffiecient (35,000 M^{-1} cm^{-1}) than photofrin® but its main disadvantage is that some patients can suffer from high skin photosensitivity.

In general, the drawbacks of organic dyes such as PS are that they suffer from photobleaching, cannot specifically target cancer cells, they have low extinction coefficients and long circulation times in the body.

An alternative to PDT is the use of gold nanoparticles (NPs) in photothermal therapy (PTT), *i.e.* the use of optical heating for the ablation of tumours. This form of therapy, pioneered by El Sayed and co-workers,[6-9] is not yet clinically used. It is based on the strong light absorption by gold NPs, which enables them to act as local heat sources that can destroy cancer cells. Key to understanding these phenomena are the optical properties of gold NPs.

Optical Properties of Gold Nanoparticles

For a spherical NP much smaller than the wavelength of light, an electromagnetic field at a certain frequency induces a resonant, coherent, oscillation of the metal free electrons across the NPs (Figure 1.2). This oscillation is known as the surface plasmon resonance (SPR).[10-12] This is quantitatively described by Mie theory.[13]

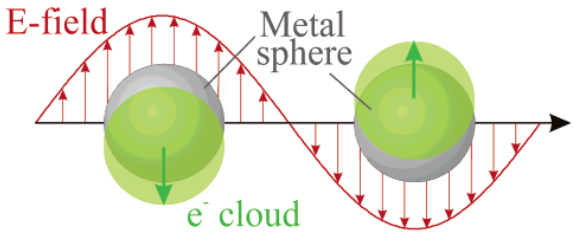

Figure 1.2: Schematic of the interaction of gold NPs with light. The electromagnetic field of the light induces a coherent dipolar oscillation of the metal conduction electrons across the NP.[10]

The surface plasmon oscillation results in the enhancement of the absorption and scattering of electromagnetic radiation in resonance with the NP SPR. [14-16] The position of the SPR band depends on the NP size, shape and surrounding dielectric medium.[10, 14, 17-20] A typical absorption spectrum of 15 nm spherical gold NPs is shown in Figure 1.3 with the absorption maximum at 520 nm. Aggregation of the NP causes the SPR band to broaden and red shift.

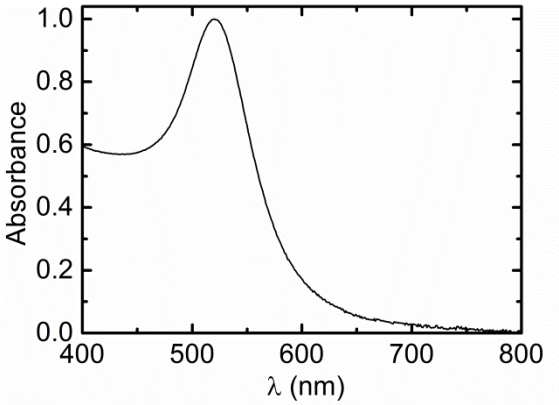

Figure 1.3: UV-Vis absorbance spectrum of 14 nm spherical gold NPs, λ_{MAX} = 520 nm

Changing the NP shape from spherical to rods dramatically changes their absorption spectrum.[16, 19, 20] Gold nanorods (NRs) have two bands in their absorbance spectrum, one that centres around 530 nm due to oscillation along their transverse axis and a stronger band in the near infrared (NIR) region about 800 nm due to oscillation along their longitudinal axis (the exact positions depend on the aspect ratio). The ability to tune the wavelength of light that the NPs absorb is important for biological applications, green

light has a penetration depth of a few millimetres and so can be used to treat skin lesions whereas longer wavelength light can penetrate tissue up to a few centimetres and so can be used for tumours inside the body. The "biological window" (Figure 1.4) which arises from the combination of the absorption of lower λ of light by the important tissue chromophores (oxy and deoxyhemoglobin and melanin) together with the occurrence of water absorption at λ greater than 1300 nm is usually quoted as between 600 – 1300 nm.[21, 22]

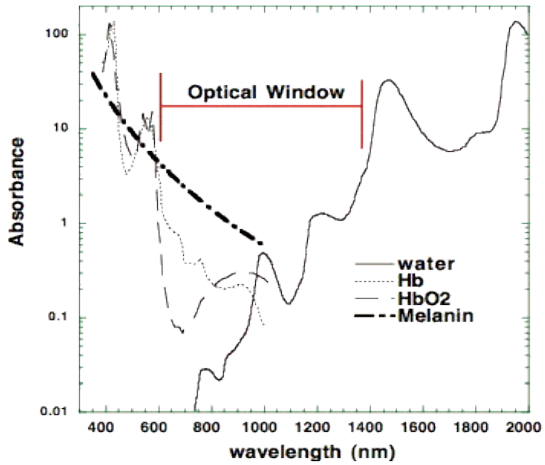

Figure 1.4: Optical window in tissue. Absorption spectra of important tissue chromophores such as water, oxy- and deoxyhemoglobin and melanin are plotted.[21]

As well as SPR enhanced absorption and scattering, gold NPs have the advantage of not being affected by photobleaching.

Cell Uptake and Cytoxicity

It is not just the unique size and shape dependent optical properties of gold NPs that have made them increasingly popular in biology and medicine[23, 24], they can also be easily synthesised and their surface functionalised with a variety of ligands. Monodisperse spherical gold NPs can be made in a range of sizes using the reduction of gold salt by trisodium citrate, as pioneered by Turkevich[25, 26], where citrate ions adsorb to the surface of the NPs resulting in a charged stabilised colloid. The surface can be

further modified using ligands that adsorb to the NP surface or using ligands with a thiol group, utilising the strong affinity of gold for sulfur.[27] Ligands can provide additional functionality such as the ability to target cells. Gold NPs can be bioconjugated to an antibody (AB) specific to a cancer associated protein, for example, breast cancer cells overexpress human epidermal receptor-2(HER2), conjugating anti-HER2 to NPs allows them to selectively target the cancerous cells.[28]

The cell uptake and cytotoxicity of gold NPs have been examined, and gold NPs are generally regarded as biocompatible. Studies using a variety of different NP sizes and surface coatings report no toxicity to cells[29-31] unless the NP size is reduced to < 2 nm.[32] Gold NPs are readily taken up by cells via endocytosis with a dependence on their size, shape and surface chemistry and once internalised they remain in vesicles.[33-35] Endocytosis takes place by multiple mechanisms that can be divided into two broad categories, phagocytosis and pinocytosis. Phagocytosis is mainly conducted by specialist mammalian cells to engulf solid particles >750 nm[36], whilst smaller particles can be endocytosed by pinocytosis which takes place in all cells (Figure 1.5). [37]

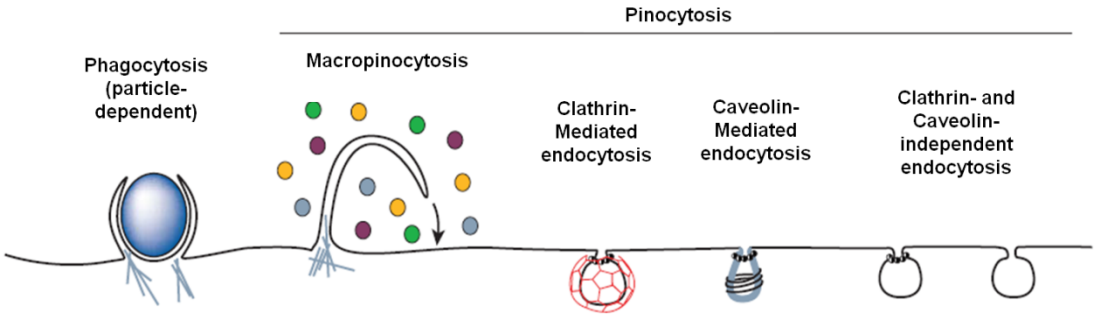

Figure 1.5: Schematic of the endocytic pathways[37]

Pinocytosis takes place by four mechanisms; firstly, macropinocytosis is a regulated form of endocytosis that mediates the non-selective uptake of solute molecules, nutrients and antigens. It is an actin-dependent process initiated from surface membrane ruffles that give rise to large endocytic vacuoles called macropinosomes. Next clathrin-

mediated (also known as receptor mediated) is a process by which cells absorb metabolites, hormones, other proteins the inward budding of plasma membrane vesicles containing proteins with receptor sites specific to the molecules being absorbed. Caveolea are defined as flat-shaped invaginations in the plasma membrane that project into the cytosol, the range between 50-70 nm but there composition varies with cell type.[37-39]

Gold Nanoparticles and Photothermal Therapy

The SPR excitation of the NPs is followed by the rapid conversion (~1 ps) of the absorbed light energy to heat,[12, 14, 40, 41] which is transferred to the surroundings by conduction, allows for the exploitation of NPs in Photothermal therapy. This has been reported using nanospheres,[8, 42-46] nanorods,[47-49] nanoshells[28, 50, 51] and nanocages.[52]

El-Sayed and co workers[8] incubated three types of cells, two cancerous that overexpress EGFR (Epidermal Growth Factor Receptor) and one healthy cell line with 40 nm gold NPs bioconjugated to anti-EGFR. The gold NP loading was obtained by measuring the absorbance of the cells after NP incubation, the cancerous cells had optical densities (OD) of 0.1 and 0.16 whereas the healthy cells had a much lower OD of 0.025. This is due to the specific binding of the anti-EGFR conjugate NPs to the cancerous cell membranes with only a few non-specific interactions resulting in a few NPs attached to healthy cell membranes. [9]

Irradiation of these cells for 4 minutes with a cw laser at 514 nm required a power of 150-200 mW to kill the cancerous cells and 450 mW for the healthy cells.[8] Numerical simulations were performed[46] to estimate minimum temperature rise necessary to kill the cells, the temperature rise during irradiation shows a linear dependence on incident power for a given OD, and so, lower irradiation power is required to reach a temperature that results in cell killing for highly loaded (i.e. the cancerous) cells. The threshold

temperature required to kill the cells was calculated to be 70-80°C under these conditions.

Using near infrared light is advantageous as the light in this region has a higher penetration depth in tissue. Hirsch et. al.[50] showed that incubating silica gold nanshells with human breast carcinoma cells resulted in a high density of NPs binding to the cell surface. Irradiation with laser light at 820 nm (in the SPR band of the nanoshells) for 7 minutes with a power density of 35 Wcm^{-2} results in the cells dying. Extending this to *in vivo* studies,[53] PEG conjugated nanoshells were injected into the tumour volume of mice, irradiation at 820 nm at 4 Wcm^{-2} for 4-6 minutes resulting in a temperature rise of 37.4 +/- 6.6 °C (above room temperature) measured using magnetic temperature resonance imaging, and sufficient enough to induce irreversible tissue damage.

Another *in vivo* experiment [52] involving gold nanocages capped with PEG ligands injected into the tumour of mice and irradiated at 800 nm (SPR λ maximum of the nanocages) with a power of 0.7 Wcm^{-2}, for ten minutes resulted in tumour damage, the recorded temperature using an IR camera was 54°C and was reached after two minutes of the laser exposure.

An alternative to using cells that are densely loaded with NPs is to use pulsed laser irradiation, damage to cells has been reported after just 15-30 minutes of incubation, when only a few particles were attached to the cell membrane or could penetrate into the cell.[43] When NPs are irradiated by short laser pulses, the energy absorbed does not have time to diffuse away from the NP before the next photon is absorbed, this leads to an extremely high local temperature. A number of reports show Photothermal killing of cells using short laser pulses of gold NPs attached to cell membranes or inside cells.[42, 51, 54]

Gold Nanoparticles and Photodynamic Therapy

Previous work published by the Brust group[55] shows that exposure of intracellular 15 nm spherical gold NPs to low power continuous irradiation results in cell death, the temperature rise under these conditions is only a few degrees and not sufficient to cause hyperthermia.

HeLa cells were incubated with 15 nm citrate gold NPs which resulted in uptake into intracellular vesicles with approximately 34,000 NPs per cell. The cells were then irradiated with a cw 514 nm laser, close to the absorption maximum of the NPs (520 nm). Irradiation at different power densities caused different degrees of damage, at 30 Wcm^{-2} there were a few surviving cells and at the highest power 55 Wcm^{-2} all of the cells were dead.

Using TEM the internal damage of the cell was assessed and it is apparent that the laser power and exposure time have an effect on the degree of damage, however, the visible damage is limited to the endosomes which under these conditions are the only organelle containing NPs (Figure 1.6).

The mechanism of the irradiation causing damage to the intracellular vesicles containing NPs and cell death was investigated. The calculated local temperature (using dynamic simulations discussed in chapter 3) rise above background was estimated to be a fraction of a degree and this resulted in the overall temperature of the sample during irradiation being only a few degrees above room temperature (RT). Any damage or cell death cannot be due to thermal effects and is ascribed to a photochemical mechanism.

The differences between this experiment[55] where local heating is limited to a fraction of a degree, and the experiments described above that cause local heating of several degrees, and overall temperature rises of at least 54°C are; there are fewer NPs and so

the amount of light absorbed by the cell monolayer is less and thus lower heating, in this case *ca*. 0.5% of the light it absorbed, for work by El-Sayed[8] approximately 25% was absorbed at similar power density. Another factor is that the NPs are smaller, after excitation of the SPR electrons, cooling occurs by heat transfer to the solvent and diffusion on the time scale of 10 to a few 100 picoseconds, strongly depending on NP size,[56] the dissipation of heat is much faster for smaller NPs and so overall local heating is lower.

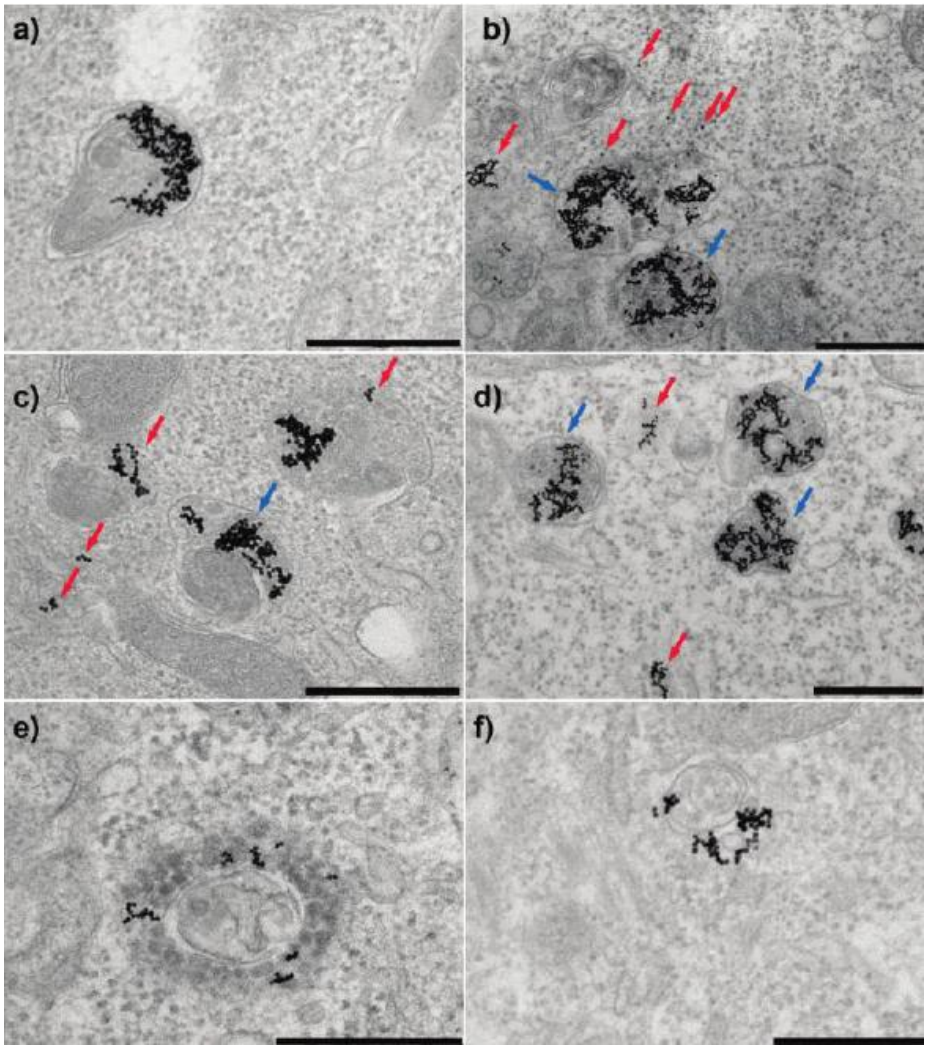

Figure 1.6: Laser inflicted subcellular damage. TEM micrographs of gold nanoparticles in HeLa cells before (a) and after (b-f) laser irradiation showing examples of the damage to the endosomes; (b-d) dissolution of the membrane of endosomes filled with fewer particles (red arrows) while endosomes filled with more particles tend to remain intact or suffer only minor damage (blue arrows); (e,f) escape of nanoparticles into the cytosol after surgical rupture of the endosomal membrane. Laser power density and exposure time: (b) 6 Wcm^{-2}, 7 min; (c,f) 20 Wcm^{-2}, 1 min; (d) 20 Wcm^{-2}, 2 min; (e) 6 Wcm^{-2}, 3 min. Scale bars are 500 nm.[55]

Early work in understanding this non-thermal photochemical method has shown *in vitro* singlet oxygen ($^1O_2$) photogeneration by irradiation of gold NPs[57-61], suggesting that singlet oxygen, which is widely used in photodynamic therapy, may be involved in the photochemical pathway responsible for cell killing.

The main subject of his thesis is to conduct a critical mechanistic study of this approach and to distinguish between photothermal and photodynamic effects are responsible for cell killing.

Thesis Outline

Chapter 2: The synthesis and characterisation of the NPs used are given at the beginning of this chapter. Next, the quantitative analysis of the cell uptake, after HeLa cells are incubated with 14 nm citrate- or CALNN- gold NPs is shown, different concentrations and incubation times investigated.

Chapter 3: A comparison between the effect of continuous irradiation on HeLa cell viability after incubation with citrate- or CALNN- gold NPs is presented. The effect of laser power, exposure time and cell confluency is shown and analysis of the results includes dynamic simulations calculating the temperature rise during irradiation.

Chapter 4: Using the singlet oxygen trap, DPBF, the yield of singlet oxygen produced when gold NPs are irradiated *in vitro* is determined. The investigation includes NPs of different sizes, shapes and ligand shells as well as continuous and pulsed laser irradiation.

Chapter 5: Conclusion and future work

Chapter 2

Gold Nanoparticles – Preparation and Cell Uptake

Chapter 2 begins with a description of the synthesis and characterisation of gold nanoparticles (NPs) used in this work. Next, the quantitative uptake results and NP localisation after HeLa cells are incubated with gold NPs are given.

It is extremely important to determine the number of NPs and their localisation after incubation with HeLa cells, as this will affect the outcome of cell irradiation experiments (Chapter 3). The amount of light absorbed and thus the temperature rise during irradiation is directly related to the number of NPs per cell, if it is not heat that is killing the cells in Chapter 3, then a proposed photochemical reaction would depend on the intracellular location of the NPs, reactive oxygen species have a short lifetime which limits diffusion and so the damage will occur very close to the NP.

The quantitative uptake and localisation of NPs by cells is dependent on a huge number of factors, including the cell type[62], the NPs size, shape and ligand shell[33-35] as well as the incubation conditions including cell medium choice.[63] As there are so many parameters that affect cell uptake it makes comparing experiments and following protocols of those reported in the literature very difficult. In this work three methods were chosen to investigate cell uptake, Inductively Coupled Plasma – Atomic Emission Spectroscopy (ICP-EAS), Electron Microscopy (EM) and UV-Vis spectroscopy.

ICP-AES determines the amount of gold in a given sample, it does not give any information about where the gold is with respect to the cells, however, a large number of cells can be analysed and there is no self-selection. To compliment this technique electron microscopy can be used, although this technique is not quantitative, you infer

the number of cells from only a relatively few number of cell sections, the localisation of the NPs can clearly be seen. Finally, measuring the absorbance of the cells without removing the cells from the culture dish has the advantages of being able to determine the number of NPs, however, again, with this technique the NPs location is not know. All three of these techniques are used to thoroughly investigate cell uptake and the experimental procedure and results are discussed in this chapter.

2.1. Experimental

2.1.1. Gold Nanoparticle Preparation

Milli-Q (MQ) water produced via distillation, followed by Millipore reversed osmosis in a system with UV steriliser, was used for all NP syntheses. All glassware was washed with Aqua Regia (3:1 HCl:HNO_3) followed by MQ-H_2O before use. All chemicals were obtained from Sigma-Aldrich and used as supplied unless otherwise stated.

2.1.1.1. Citrate Gold Nanoparticle Preparation

13-15 nm Citrate-stabilised gold nanoparticles were prepared by reducing tetrachloroaurate with citrate according to the Turkevich-Frens method.[25, 26] 50 µmol (19.7 mg) $HAuCl_4 \cdot 3H_2O$ in 150 mL MQ-H_2O was heated to boiling in a round-bottom flask under reflux while being continuously stirred using a magnetic stirrer bar. Once boiling, 4.5 mL of 34 mM aqueous trisodium citrate dihydrate solution was added rapidly, the colour of the mixture changed immediately from pale yellow to colourless, then to deep purple and finally ruby red, as citrate reduces the gold from Au(III) to Au(0). The mixture was refluxed for 30 minutes, allowed to cool to room temperature and stirred overnight. The ruby red sol was filtered through fluted filter paper and characterised.

45 nm Citrate-Stabilised gold nanoparticles were synthesized following a kinetically controlled seeded growth strategy via the reduction of $HAuCl_4$ by sodium citrate.[64] The seeds were produced by heating a solution of 2.2 mM sodium citrate in MQ H_2O (150 mL) in a three-necked round-bottom flask for 15 min. under vigorous stirring. A condenser was used to prevent evaporation of the solvent. Once boiling, 1 mL $HAuCl_4$ solution (25 mM) was injected. The colour of the solution changed from yellow to bluish grey and then to soft pink in 10 min.

The seeds were cooled to 90°C and 1 mL $HAuCl_4$ solution (25 mM) was added, the solution was stirred for 30 min. The process was repeated. The sample was then diluted by removing 55 mL and then adding warm MQ H_2O (53 mL) and sodium citrate solution (2 mL, 60 mM) to the remaining solution. The two 25 mM gold additions were then repeated with this solution to produce spherical NPs of approximately 45 nm diameter.

5 nm citrate gold NPs were synthesised using a reverse Turkevich method.[65] 90 mL MQ H_2O was heated to boiling in a round-bottomed flask containing a magnetic stirrer bar, 2 mL aqueous trisodium citrate (71 mM) was added and the solution stirred for 1 min followed by the addition of 1 mL $HAuCl_4$ solution (30 mM) and stirring for 5 min. 19 mg $NaBH_4$ was dissolved in 25 mL aqueous trisodium citrate (71 mM) and 1 mL of this was added to the reaction mixture and stirred for 5 min. A colour change from pale yellow to colourless, to dark purple and finally deep ruby red was observed. The colloid was stirred for a further 10 min while cooling to room temperature and the NPs characterised.

2.1.1.2. Ligand Exchange

13-15 nm CALNN Gold Nanoparticles: Briefly, 100 µL of an aqueous 1 mg/mL solution of CALNN (Peptide Protein Research Ltd.) (Figure 2.1) was added to 900 µL 2

nM citrate gold nanoparticle solution, mixed well and left overnight at room temperature. The obtained nanoparticles were purified from excess ligand by centrifuging 3 times (12,000 rpm, 20 min, 15°C), discarding the supernatant and resuspending in MQ H_2O after each cycle.

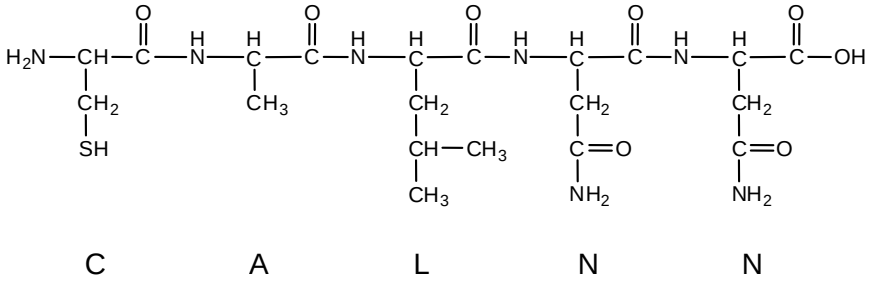

Figure 2.1: CALNN Peptide, consisting of;
Cysteine (C), Alanine (A), Leucine (L), Asparagine (N), Asparagine (N)

13 -15 nm PEG Gold NPs: To 12 mL of 14 nm citrate gold NP solution, 86 µL of PEG-OH (prochimia) (Figure 2.2) solution (0.01 M in methanol) was added (20,500 PEG ligands per NP), mixed well and left overnight. The obtained PEG-functionalised gold NPs were purified from excess ligand by centrifuging 3 times (13,000 rpm, 15 min, 15°C), discarding the supernatant and resuspending in H_2O after each cycle.

Figure 2.2: PEG-OH, MW 380.58 gmol^{-1}

2.1.1.3. Gold Nanoparticle Characterisation

UV-Vis Spectroscopy – Spectra were recorded on a spectrophotometer (Thermo Scientific Genesys 10S), using a cuvette with a path length of 1 cm.

Differential Centrifugal Sedimentation (DCS) - Particle size distributions were measured using a DCS disc centrifuge DC24000 (CPS Instruments Inc.). Freshly prepared gradient fluids starting at 8 wt. % sucrose in MQ H_2O and increasing to 24 wt.

% over 9 additions were filled successively into the disc rotating at 24,000 rpm. To calibrate the machine before each sample measurement, 0.377 μm poly(vinyl chloride) particles (Analytik Ltd.) were used. Each sample was analyzed three times to verify data reproducibility.

Transmission Electron Microscopy - Samples for TEM imaging were prepared by placing *ca.* 1.5 μL of the colloidal dispersion onto piloform-coated copper grids (Agar Scientific, 400 hexagonal mesh) and waiting for the solvent to evaporate before the sample was imaged with a FEI Tecnai Spirit TEM at 120 kV using AnalySIS software (Soft Imagine Systems). Size distributions were done using TEM micrographs and imageJ using the: analyze – measure function, after setting the scale using the image scale bar.

2.1.2 Cell Culture and Nanoparticle Incubation

2.1.2.1. HeLa Cell Culture and Nanoparticle Incubation

HeLa Cell Culture - HeLa cells were cultured in either 100 mm or 35 mm cell culture dishes in Dulbecco's Modified Eagle Medium (DMEM) supplemented (with 10% heat-inactivated fetal bovine serum, 1% non-essential amino acids and 1% streptomycin, at 37°C in a humidified atmosphere of 5% CO_2. Passages 4 – 29 were used for experiments and cells were typically grown to 70-80% confluency before splitting and re-seeding one or two days before an experiment.

Nanoparticle Incubation – 2 or 10 mL of NP solution and DMEM (1:1), mixed thoroughly, were added to cells cultured in 35 or 100 mm dishes, respectively. The final concentration of NPs was either 2 or 4 nM and the incubation time was 3 or 24 hours. After incubation the cells were washed 3 times with 1 mL (35 mm dish) or 5 mL (100 mm dish) warmed phosphate buffered saline (PBS), pH 7.4, to remove the excess NPs.

Images of the cells were taken using a GX Optical light microscope with an attached digital camera controlled using GX Capture software.

2.1.2.2. Electron Microscopy

Cells in a 35 mm culture dish were washed with warmed PBS before being fixed with a 1 mL solution containing 4% paraformaldehyde and 2.5% glutaldehyde (taken from 16 and 25% stock solutions, respectively) in 0.1 M phosphate buffer (PB), pH 7.4 for 1 hour. The cells were then rinsed with room temperature 1 mL PB twice and post-fixed using reduced OsO_4 (2% OsO_4, 1.5% potassium ferrocyanide in 0.1 M PB) by adding a few drops to cover the bottom of the dish for 1 hour before being washed 5 times with 1 mL MQ-H_2O for at least 3 minutes per wash. 1 mL aqueous 2% OsO_4 solution was then added to the cells for 40 minutes and a second set of 5 x 1 mL MQ-H_2O washes was performed before leaving the cells in 1 mL 1% aqueous uranyl acetate solution at 4°C overnight. On the second day the cells were washed with MQ-H_2O (3 x 1 mL, 15 minutes washes) and dehydrated gradually using a series of ethanol solutions (1 mL) in water (30, 60, 70, 80 and 100%) and finally the cells were embedded in epoxy resin. The resin was polymerised at 60°C for at least 48 hours. Ultrathin sections (*ca.* 70 nm) were cut using a diamond knife on a Leica Ultramicrotome and mounted on piloform coated 200 hexagonal mesh copper grids. The sections were then post stained with 5% uranyl acetate in 50% ethanol and 2% aqueous lead citrate solution and imaged with an FEI Tecnai Spirit TEM at 120kV or FEI 250 Quanta FEG-ESEM at 30kV in STEM mode.

2.1.2.3. ICP-AES: Determination of Intracellular Gold Content

Cells grown to approximately 70% confluency in 35 mm or 100 mm cell culture dishes were incubated with gold nanoparticles and then washed with 1 mL PBS (described above). The cells were then detached from the dish using 0.150 mL (35 mm dish) or 1 mL (100 mm dish) of trypsin at 37°C for 5 minutes before being collected with DMEM

at a final volume of 2 mL or 10 mL, mixed well and counted using a haemocytometer. The cell suspension was centrifuged, the supernatant removed and the cell pellet digested in 5 mL *aqua regia*.

2.1.2.4. Measuring the Absorbance of Intracellular Nanoparticles

To measure the absorbance of intracellular NPs an Ocean Optics USB2000 + UV-Vis-ES was used, the corresponding flexible optical fibre allowed for an easy custom built set-up (Figure 2.3). The set up was constructed so that a cell culture dish was placed on a stage with the halogen lamp light source underneath and the optical fibre above the dish. To avoid heating a UV/IR filter was placed in the light path before the sample and a fan was used for further cooling. This limited the temperature of the sample to a maximum value of 27.5°C.

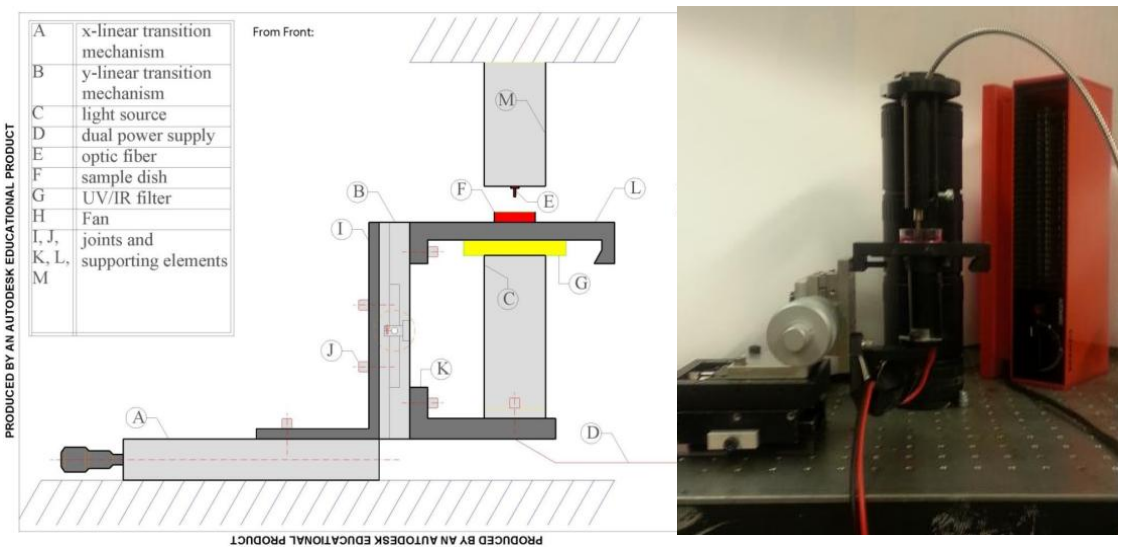

Figure 2.3: A) Schematic- and, B) Image of the UV-Vis set up
(taken from S. Kolarova – Chem 366 Project, University of Liverpool, 2013)

After incubation of a 35 mm dish of cells with either citrate or CALNN gold NPs, the cells were washed 3 times with 1 mL warmed PBS before 600 µL of fresh PBS was added to the dish for the measurement. The absorbance was calculated using 600 µL of PBS in a 35 mm culture dish as a reference sample.

2.2. Gold Nanoparticle Characterisation

The characterisation of all gold NPs is presented here. However, only 13-15 nm citrate- and CALNN- gold NPs were used for the experiments described in Chapters 2 and 3. Experiments with other NPs are described in chapter 4.

2.2.1 Citrate Gold Nanoparticle Preparation

Citrate gold NPs with different core sizes were prepared and characterised. 13-15 nm NPs were prepared using the Turkevich-Frens method,[25, 26] the use of the reversed Turkevich method[65] resulted in NPs with a diameter of 5 nm and, to increase the size to 45 nm, seeded-growth was used.[64] (All methods of preparation are described in the experimental section 2.1.1.).

The typical surface plasmon band, observed at 520 nm for 13-15 nm NPs, is responsible for the ruby red colour of the sol. As the exact position of the absorbance band depends on the size of the NPs, decreasing the NP diameter to 5 nm causes a slight blue shift to 518 nm, whereas increasing the NP size to 45 nm red shifts the absorbance maximum to 538 nm (Figure 2.4(A)).

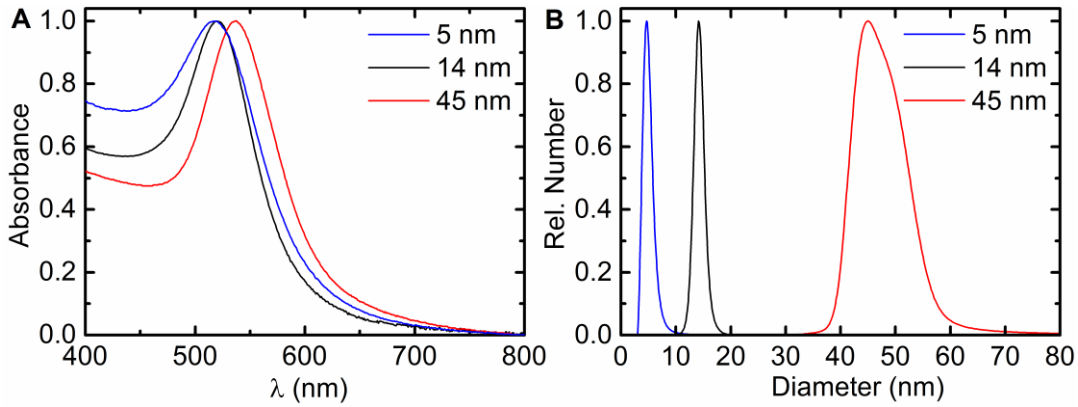

Figure 2.4: A) Uv-Vis spectra of 5, 14 and 45 nm NPs with λ_{max} at 518, 520 and 538 nm, respectively, and, B) Differential centrifugal sedimentation results of 5, 14 and 45 nm NPs

Figure 2.4(B) gives the results of differential centrifugal sedimentation (DCS) experiments used to measure the size distribution of NPs. DCS separates particles of the same density by mass, but the reported result must be corrected as the method assumes that the density of the entire NP (including the capping layer) is that of gold (19.3 g cm^{-3}), ignoring the fact that the ligand shell has a much lower density. For citrate NPs, the effect is on the order of ~ 1 nm,[66] (the results shown in Figure 2.4 have not been corrected).

Figure 2.5 shows TEM micrographs of the 5, 14 and 45 nm NPs, and their size distribution obtained by measuring the particles in the images using imageJ. The results imply that the NPs have larger diameters than those reported by DCS (after correction – which for those reported in Figure 2.4 would be 6, 15 and 46 nm).[66] However, as using TEM means smaller sampling size, potentially selective sample sections and limited resolution which has been reported in detail;[66] so from this point onwards the size reported for the NPs used in various experiments is the corrected DCS value.

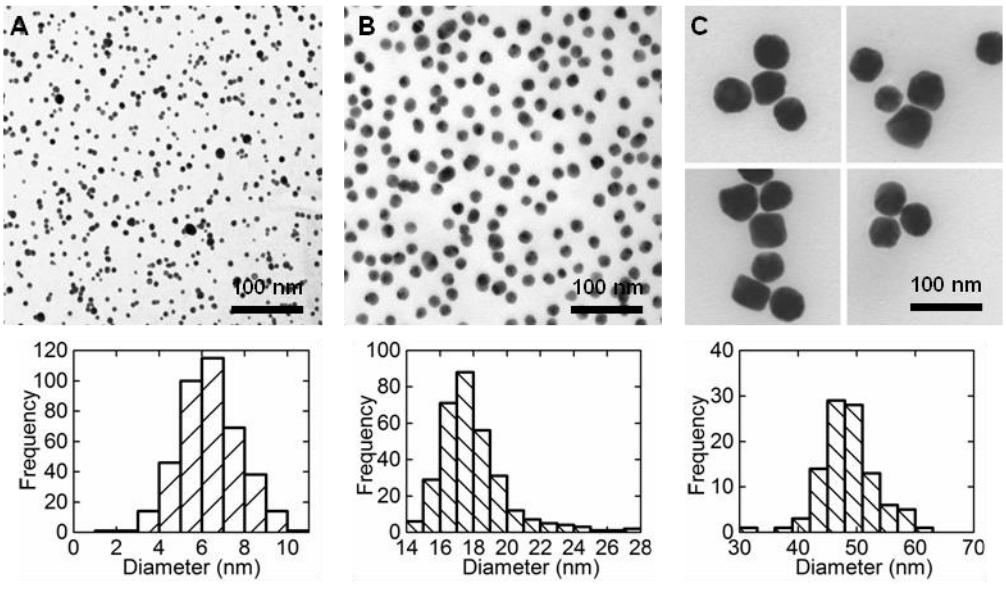

Figure 2.5: TEM micrographs and their corresponding size distributions for spherical gold NPs of diameter A) 5 nm, B) 14 nm and C) 45 nm

2.2.2. Ligand Exchange

Citrate gold NPs are easily functionalised by substitution of the citrate ligands by ligands forming a strong gold-thiol bond. Citrate can be replaced by covalently bonding the pentapeptide CALNN (Figure 2.1) through the side chain of the N-terminal cysteine, as demonstrated by Lévy *et. al.*[67] or by thiolated poly(ethylene) glycol - PEG-OH (Figure 2.2).

After addition of the ligands to the citrate NPs and multiple centrifugation cycles (as described in 2.1.2.), the NPs were characterised using UV-Vis spectroscopy and DCS. The UV-Vis spectrum (Figure 2.6(A)) of CALNN and PEG-OH 14 nm gold NPs shows a shift in the plasmon band from 520 nm to 523 and 524 nm, respectively. This indicates the presence of the ligands on the NPs surface, the shift in the absorbance is due to the change of the refractive index of the medium surrounding the metal core. [17]

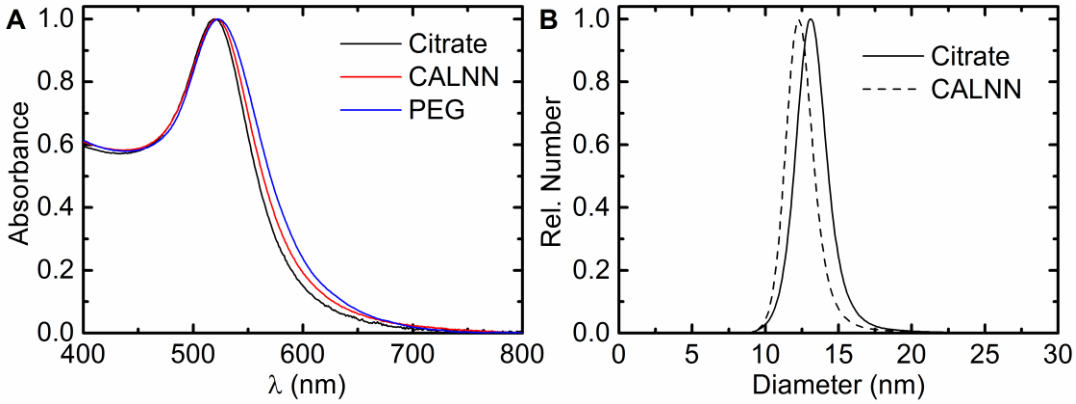

Figure 2.6: A) Uv-Vis absorbance spectra of 14nm- citrate, -CALNN and -PEG gold NPs with λ_{MAX} at 520, 523 and 524 nm, respectively, and B) DCS results of 14 nm citrate gold NPs (solid line) and the same NPs after exchanging the citrate with CALNN ligands (dotted line).

DCS was also used to confirm that CALNN was covalently bound to the NP surface. Figure 2.6(B) shows the DCS results, as expected there is a decrease in reported size, (from 13 nm to 12.25 nm), this is because CALNN is a larger ligand than citrate and so the average density of the CALNN gold NPs is further from the average density of 19.3g/cm^3 than citrate gold NPs, hence it appears smaller.[66] The same method was also

used for PEG-capped gold NPs, a shift of 0.2 nm vs. citrate NPs was seen when 14 nm gold NPs were capped with PEG-OH (results not shown).

2.3. Quantifying Cell Uptake of Gold Nanoparticles

Endocytosis of NPs is size, shape and surface chemistry dependent[68] with incubation conditions also playing a key role in the amount of cell uptake, which ranges from a few hundred[33, 35] to tens of thousands[69] NPs per cell.

2.3.1. Cell Culture and Nanoparticle Incubation

HeLa cells, an immortal epithelial cancer cell line derived in 1951, were incubated with either citrate- or CALNN- gold NPs. The NPs were pre-mixed with cell medium and added to the dish before incubating the cells at 37°C (see 2.1.2). After washing to remove excess NPs, the amount of NPs per cell and their localisation was determined using ICP-AES, electron microscopy and UV-Vis spectroscopy.

2.3.1.1. ICP-AES: Determination of Intracellular Gold Content

After incubation, the cells were detached from the dish using the enzyme trypsin, counted and digested in aqua regia before the gold content was analysed by ICP-AES (see section 2.1.3.). Multiple dishes prepared on the same date were analysed, as well as the experiment being repeated several times; the exact size of the NPs was determined by DCS for each experiment. A summary of the results is shown in Figure 2.7 for cells incubated with citrate NPs using different incubation conditions (individual experimental results are given in appendix 2 – table 2.1).

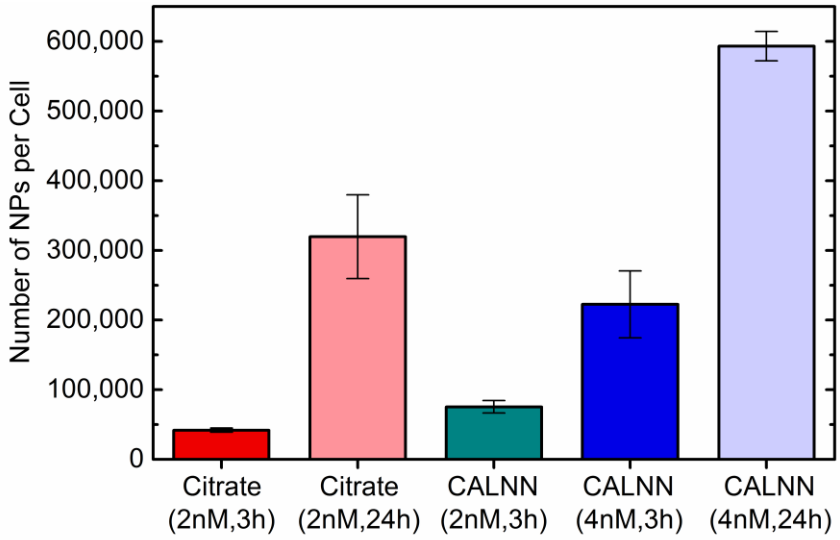

Figure 2.7: The number of NPs per cell calculated from the gold content analysed by ICP-AES after HeLa cell incubation with NPs at a final incubation concentration of 2 or 4 nM and an incubation time of 3 or 24 hours. Error bars are calculated using the standard deviation of results from multiple experiments which are shown in Appendix 2.

Figure 2.7 shows that there is a dependence on the incubation time and concentration of the amount of NPs per cell and that there are more NPs per cell for incubations with CALNN gold NPs than for citrate using the same incubation conditions.

For an incubation of 3 hours with citrate NPs at a final concentration of 2 nM, there are approximately 42,000 NPs per cell, increasing the incubation time to 24 hours at the same concentration gives approximately 320,000 NPs per cell indicating that cell uptake is roughly proportional to incubation time.

For an incubation of 3 hours with CALNN NPs at a final concentration of 2 nM, there are approximately 75,000 NPs per cell, increasing the incubation concentration to 4 nM gives 220,000 NPs per cell, indicating that cell uptake is roughly proportional to concentration. Finally, increasing the incubation time at 4 nM to 24 hours yields approximately 593,000 NPs per cell.

2.3.1.2. Electron Microscopy

To determine the localisation of the NPs, electron microscopy was used. An attempt was also made to quantify the number of NPs per cell using TEM/STEM. The cells were cut into sections with a thickness of *ca.* 70 nm, a chosen cell on a section was imaged at high enough magnification so that individual NPs could be seen. The number of NPs in that section of the cell were counted and the number multiplied by 5000/70 to give the number of NPs per cell, assuming a cell thickness of 5 μm.

3 hour Incubation of HeLa Cells with Citrate gold NPs (2 nM)

Figures 2.7 and 2.8 are electron microscopy images of different sections of two different cells. They show that, once internalised, the NPs remain in intracellular vesicles[33] that vary in size from containing a few NPs up to containing about 100 NPs in a 70 nm section. The approximate number of NPs in each endosome section is given in the figures.

The number of NPs in the cell section shown in Figure 2.7(A and B), summed over all parts (intracellular and those bound to the surface), is 361 and the sum of the NPs in the section shown in 2.8 is 683, multiplying these numbers to account for the whole cell yields approximate values of 25,600 and 48,500 NPs per cell. This is in semi-quantative agreement with the ICP-AES result of 42,000 NPs per cell (2.3.1.1) taking into consideration the uneven distribution of NPs through the cell sections, the difficulty in counting NPs in densely packed endosomes and the averaging of the value in one section over the whole cell.

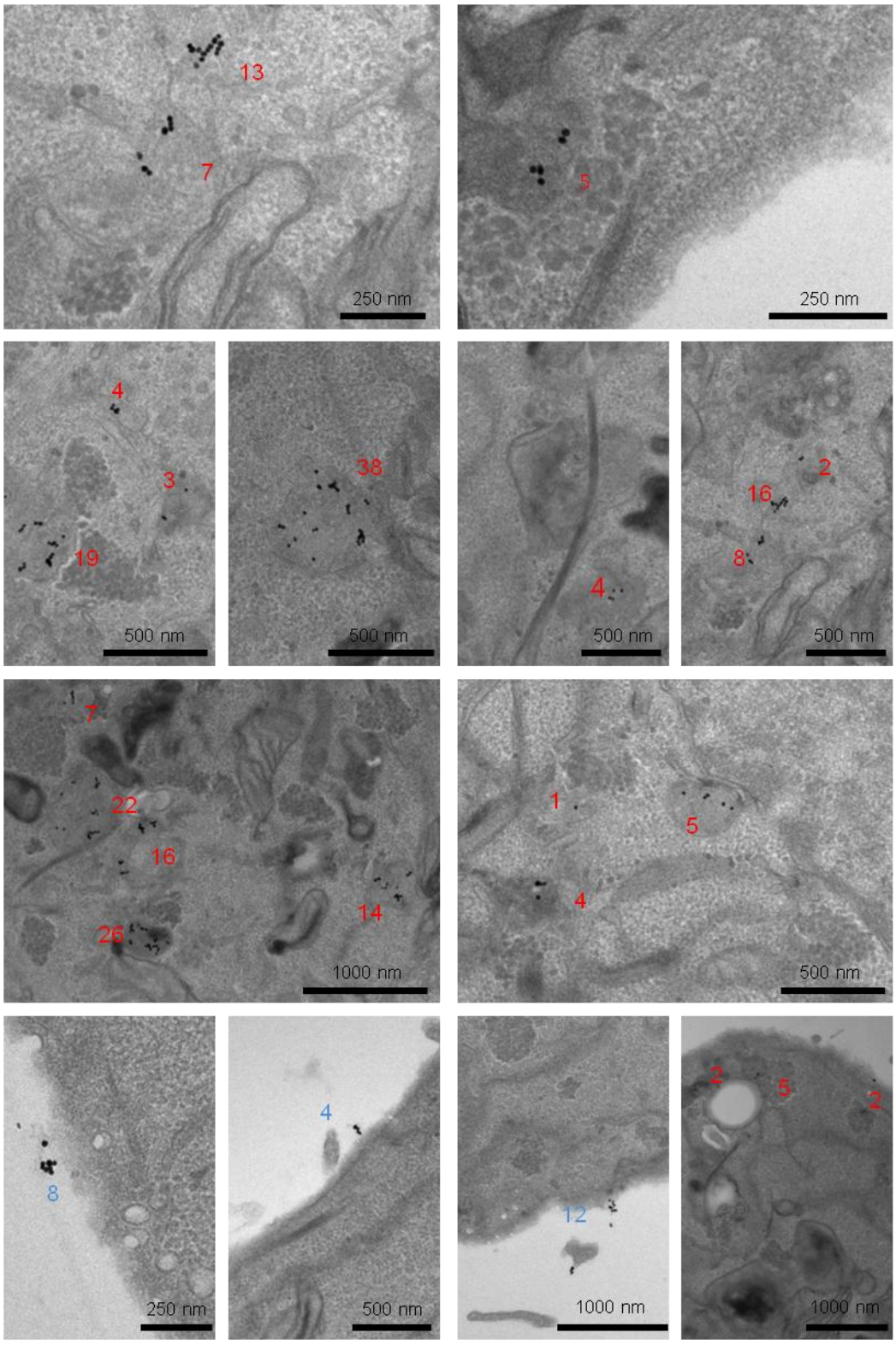

Figure 2.7(A): TEM images of a HeLa cell after incubation with 14 nm citrate gold NPs (3 hours, 2 nM). The images are from the same section of one cell. The numbers shown are the amount of NPs in that section each endosome (red) and the NPs attached to the surface of the cell (blue).

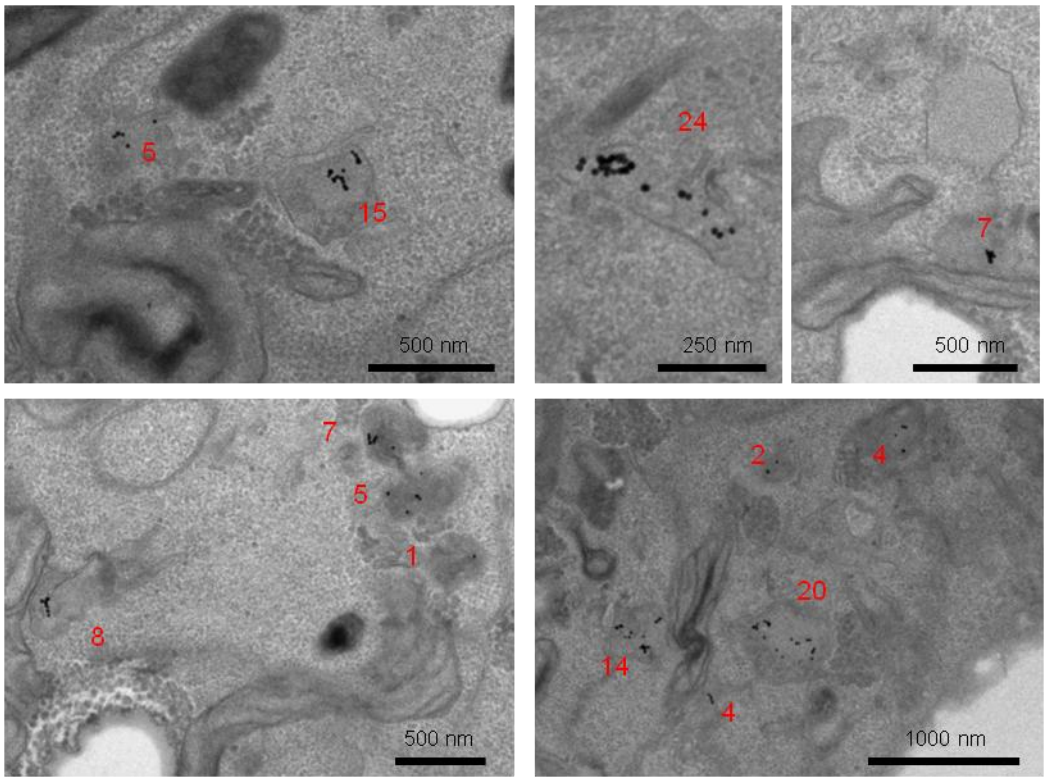

Figure 2.7(B): TEM images of a HeLa cell after incubation with 14 nm citrate gold NPs (3 hours, 2 nM). The images are from the same section of one cell. The numbers shown are the amount of NPs in that section each endosome (red).

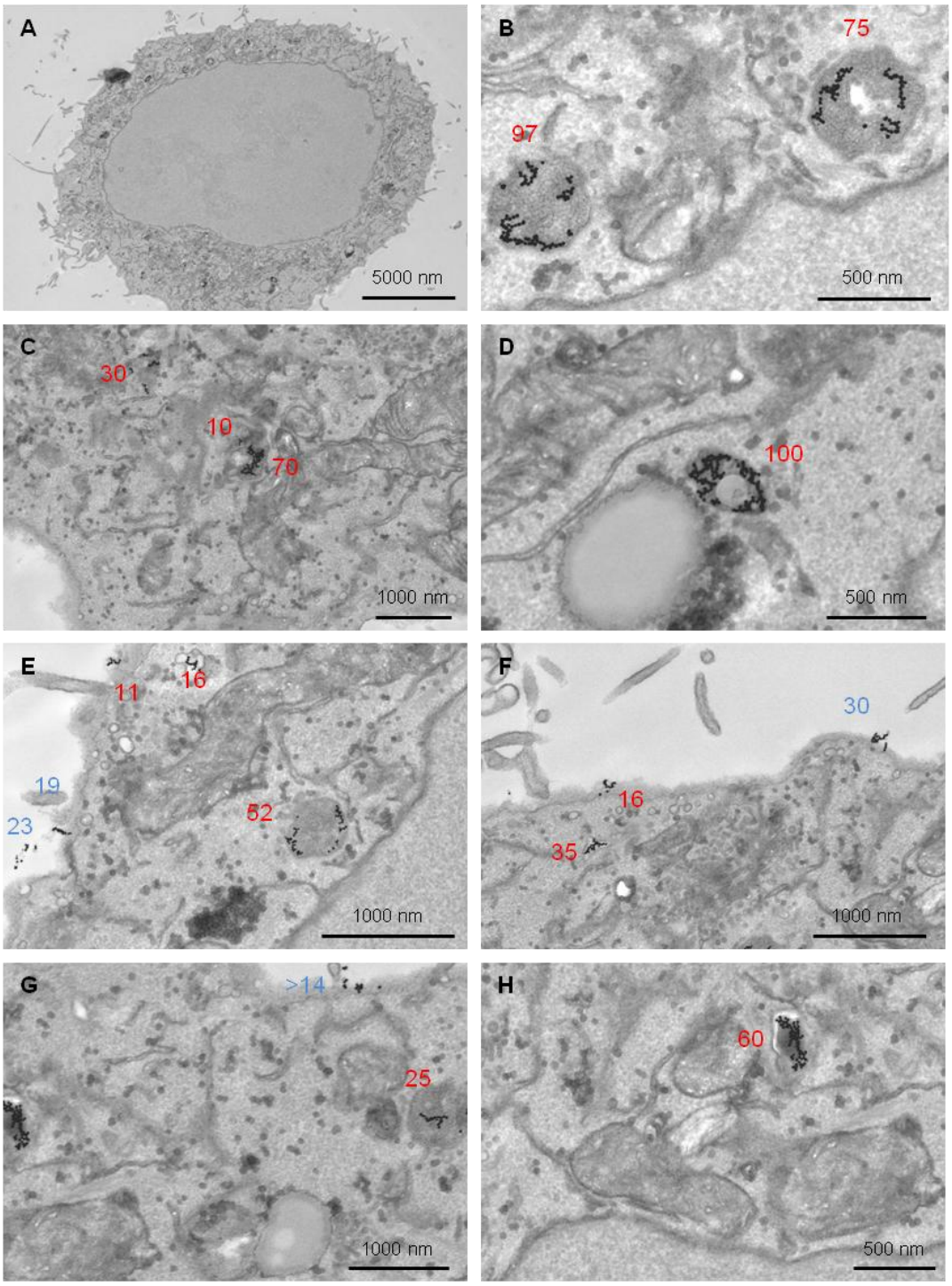

Figure 2.8: STEM images of a HeLa cell after incubation with 14 nm citrate gold NPs (3 hours, 2 nM) A) the whole cell section at low magnification and B-H) images of the same cell section at higher magnification. The numbers shown are the amount of NPs in that section for each endosome (red) and the NPS attached to the surface of the cell (blue).

3 hour Incubation of HeLa Cells with CALNN gold NPs (4 nM)

After incubation with CALNN gold NPs, the STEM images (Figure 2.9) show that there are more NPs attached to the cell membrane than after incubation with citrate NPs. This example shows that there are approximately 230 NPs in endosomes in this section and 1800 NPs attached to the cell membrane. This gives approximately 145,000 NPs per cell, again this is in agreement with the ICP-AES results (Section 2.3.1.1.).

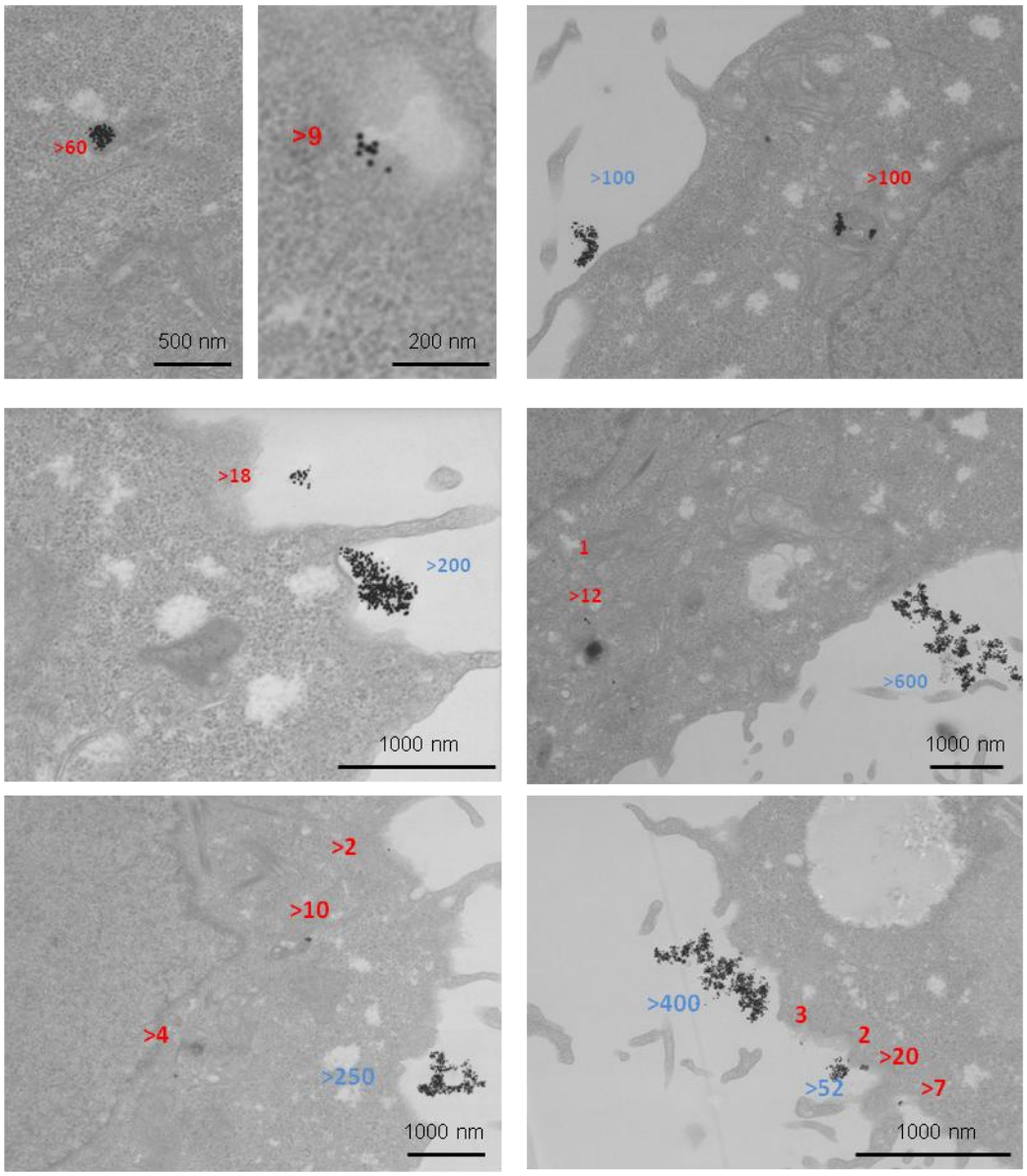

Figure 2.9: STEM images of a HeLa cell after incubation with 14 nm CALNN gold NPs (3 hours, 4 nM). The images are from the same section of one cell. The numbers shown are the amount of NPs in that section in each endosome (red) and the NPs attached to the surface of the cell (blue).

24 hour Incubation of HeLa Cells with Citrate gold NPs (2 nM)

Figure 2.10 shows sections of HeLa cells after incubation with 2 nM 14 nm citrate gold NPs for 24 hours; increasing the incubation from 3 to 24 hours results in a higher number of NPs endocytosed, in agreement with the ICP-AES results in section 2.3.1.1. It reduces the number of NPs found in smaller vesicles and increases the number found in larger vesicles, indicating intracellular trafficking from primary endocytic vesicles towards late endosomes and lysosomes.[35] As the vesicles in the cell are so densely packed after 24 hour incubation, no attempt was made to approximate the amount of NPs per cell using TEM.

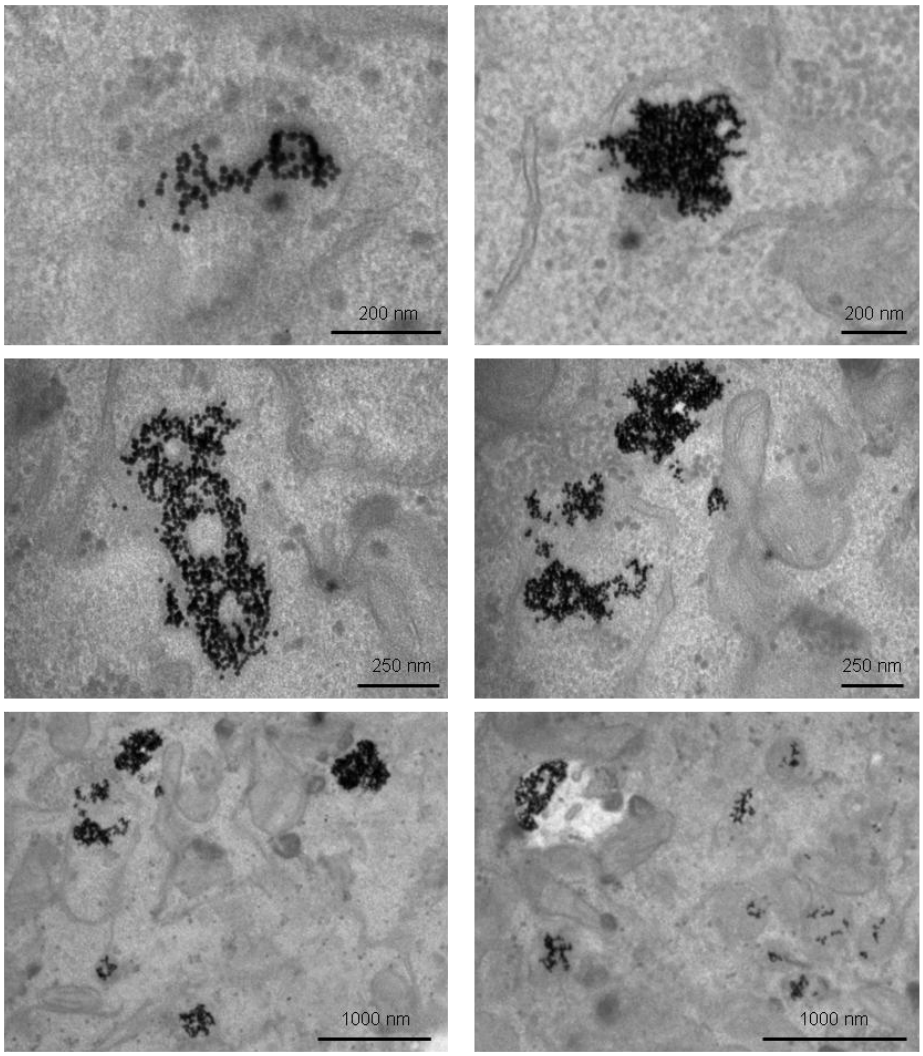

Figure 2.10: TEM images of HeLa cells after incubation with 14 nm citrate gold NPs for 24 hours (2 nM).

2.3.1.3. Measuring the Absorbance of HeLa Cells after Incubation with Gold Nanoparticles

An important parameter in photodynamic therapy is how much incident light is absorbed by the NPs associated with the cells after incubation. This is also an important factor in calculating the temperature rise during irradiation of the cells (Chapter 3).

To measure the absorbance of the HeLa cell monolayer after incubation with CALNN or citrate gold NPs a UV-Vis spectrometer was set up as described in 2.1.2.4.

HeLa Cells and CALNN Gold Nanoparticles

HeLa cells in a 35 mm culture dish with a confluency of *ca.* 900 cells per mm^2 were incubated with CALNN gold NPs (4 nM, 3 hours), Figure 2.11 shows the UV-Vis absorbance spectra taken on two different areas on the dish. All of the UV-Vis spectra show that the plasmon band is broader than that of the gold NPs in Figure 2.4(A), with the maximum absorbance shifted from 520 to *ca.* 535 nm. This is expected as the electron microscopy images show that the NPs are either aggregated in densely packed endosomes or are aggregated on the cell surface. The measurements here are underestimating the absorbance because there is a scattering component of the spectra which is stronger at lower wavelenghts. The dotted lines shown in the spectra are used to approximate this, but ignore the fact that the absorbance spectra do not go to zero between 400 and 500 nm. The absorbances measured in the plasmon resonance band are 8.6 and 8 mOD (Figure 2.11).

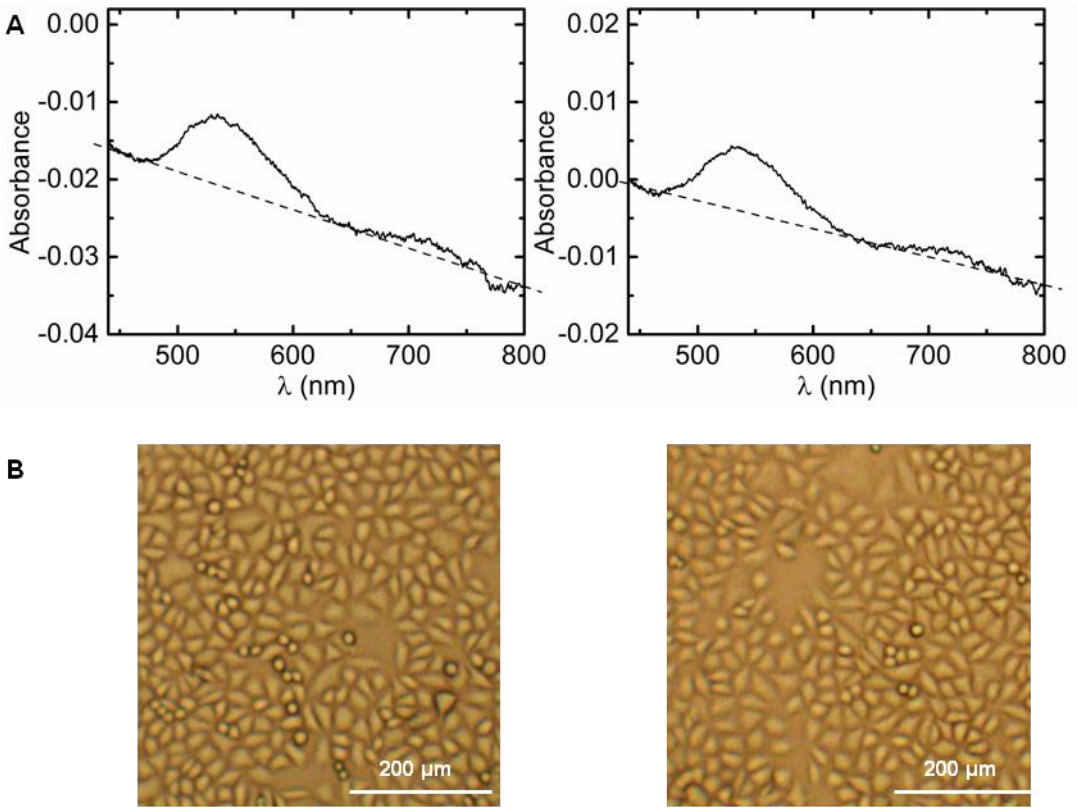

Figure 2.11: A) UV-Vis absorbance spectra of HeLa cells with a confluency of approx. 900 cells per mm^2 after incubation with CALNN gold NPs (3 hours, 4 nM), and B) Images of the cell culture that the measurements were recorded from.

An absorbance of 3.8 mOD was measured (Figure 2.12(A)) for cells incubated using the same conditions (CALNN, 3 hours, 4 nM), but at a lower confluency of *ca.* 500 cells per mm^2 (Figure 2.12(B)).

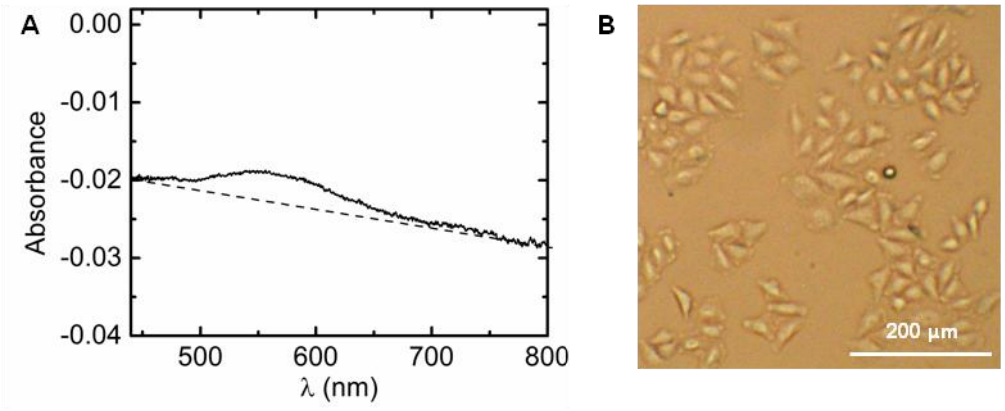

Figure 2.12: A) UV-Vis absorbance spectra of HeLa cells with a confluency of approx. 500 cells per mm^2 after incubation with CALNN gold NPs (3 hours, 4 nM), and B) Images of the cell culture that the measurements were recorded from.

The expected absorbance of the HeLa cell monolayer can be estimated using the number of cells per mm^2, the number of NPs per cell (220,000, as determined by ICP-AES for HeLa cells incubated with CALNN gold NPs for 3 hours at a final concentration of 4 nM, see 2.3.1.1.) and extinction coefficent of 14 nm NPs (ε_{14} = 2.85x10^8 M^{-1} cm^{-1}).[70] The cells at higher confluency are expected to have an absorbance of *ca.* 9 mOD and the lower confluency cells *ca*. 5 mOD, which agrees reasonably well with the measured values of 8 and 3.8 mOD.

HeLa Cells and Citrate Gold Nanoparticles

After incubation of HeLa cells with citrate NPs (2 nM, 3 hours), no absorbance was recorded even when cell confluency was relatively high at *ca*. 880 cells per mm^2 (Figure 2.13). The two measurements were recorded in different areas of the same dish.

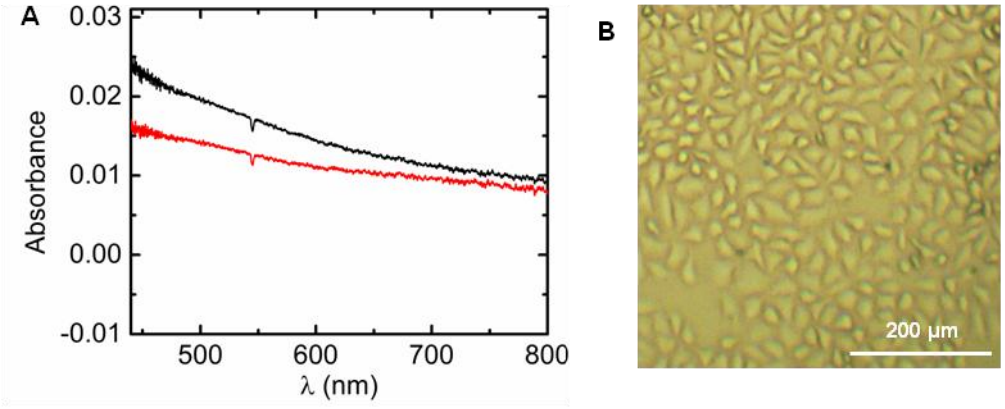

Figure 2.13: A) UV-Vis absorbance spectra of HeLa cells with a confluency of approx. 880 cells per mm^2 after incubation with citrate gold NPs (3 hours, 2 nM), and B) Images of the cell culture that the measurements were recorded from.

The expected absorbance of the cell monolayer with confluency of *ca.* 880 cells per mm^2 and 42,000 NPs per cell, is estimated at 1.7 mOD, but, as shown in Figure 2.13, the SPR is not detectable. This is because the aggregation state of the NPs leads to broadening of the plasmon band and so a decrease in the maximum absorbance and the NP absorbance at 450 nm is not zero and so the plasmon band versus the baseline is somewhat smaller

than estimated from the extinction coefficient of the NPs. As the cells in Figure 2.13 are almost 100% confluent (and this is the highest confluency used for experiments) then it is not surprising that for all UV-Vis measurements no detectable absorbance was recorded. The measured spectra are in full agreement with the uptake results obtained from ICP-AES (see 2.3.1.1).

2.4. Summary of Cell Uptake

As mentioned in the introduction to this chapter, comparing cell uptake results is difficult because of the number of factors that effect the process. There are a couple of reports that give a quantitative analysis of HeLa cell uptake of citrate NPs, Chan et. al. [33] report that the uptake is size dependent with the most efficient size being 50 nm gold NPs (compare to 14, 30, 50 and 100 nm). However, they report that the maximum uptake is on the order of a few thousand which is much lower than the uptake reported here. An uptake of approximately 34,000 NPs per cell when using a final concentration of 5 nM for 2 hours[69] which is similar to the conditions used here (3 hours, 2 nM) has been reported, although this is somewhat lower than 42,000 NPs per cell obtained in these experiments this could be because the number of cells was estimated from cell confluency and not counted. These reports and others[35, 71] show that once gold NPs with a variety of ligands such as citrate and CALNN are internalised by cells they remain in endocytic vesicles, they do not escape these endosomes which is in agreement with the work shown here. Cell uptake studies done at 4°C[62], a temperature low enough to stop endocytosis, confirm that these are endocytic vesicles as no uptake was seen at using these conditions.

Under the conditions used here, incubating HeLa cells with 14 nm citrate gold NPs for 3 hours results in 42,000 NPs per cell, with the majority of the NPs contained in intracellular endosomes, increasing the incubation time to 24 hours (2 nM) increases the

number of NPs to 320,000 NPs per cell, with the NPs in large intracellular vesicles. Incubating HeLa cells with 14 nm CALNN gold NPs for 3 hours at a 4 nM results in 220,000 NPs per cell, with a large proportion of the NPs attached to the cell membrane; these three conditions will be used for irradiation experiments in Chapter 3.

Chapter 3

Photochemical *vs*. Photothermal Cancer Cell Killing

Chapter 3 discusses the differences between photothermal and photodynamic effects. These are manifested when comparing cell killing using citrate gold NPs with the observation made with CALNN gold NPs. While the determination of whether cell killing under these conditions is photochemical or photothermal is mostly based on dynamic simulations to estimate the temperature of the sample during irradiation, a phenomenological comparison of the distribution of dead cells is also included.

3.1. Experimental

3.1.1. Irradiation Setup

After HeLa cells cultured in 35mm dishes were incubated with 13 -15 nm gold NPs and washed with PBS to remove the excess of NPs, as described in Chapter 2.1.2 (Incubation time, NP concentration and NP type will be stated for each experiment), 2 mL of PBS (at room temperature) was added to the dish.

To decide which areas of cells on the dish were going to be irradiated, a mark was made on the dish which was aligned with a marker on the microscope and irradiation stages, this indicated the Y-direction (Figure 3.1). The dish centre was marked with a sticker with a hole and, using a digital camera attached to an optical microscope (GX Optical Microscope and GX Capture), images of the sticker area and areas at +/- 5 mm in the Y and X direction (Areas 1 – 4, Figure 3.1) were taken. The area in the sticker was used as a (not irradiated) control and the other areas exposed to the laser beam.

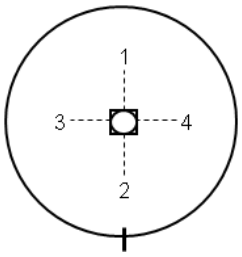

Figure 3.1: Schematic of the areas marked on the cell culture dish prior to laser irradiation

Protocol development: The initial protocol was to mark the irradiation area with a sticker with a hole that was slightly larger than a laser beam. This was compared to areas (on the same dish and on different dishes) where a large circle had been drawn to mark the irradiation area and there were always significantly more cell deaths in the stickered areas. This effect could be due to the additional scattering of light and/or the sample could be heated due to the additional absorbance of light by the sticker. In light of this discovery, the method described above was developed and used for all experimental results reported.

After imaging, the culture dish was placed on an X-Y-translational stage in front of the laser (Figure 3.2) and using low laser power (15 mW) the laser beam was aligned to the sticker. Using the translational stage the dish was moved so that areas 1-4, (Figure 3.1) were irradiated consecutively. There is a large aperture underneath the cell dish so that the translation stage is not heated during irradiation. The laser is a diode-pumped solid state continuous wave laser at 532 nm with a $1/e^2$ beam diameter of 1.85 mm (Laser Quantum Opus 532). The exposure time and laser power will be given for each experiment in the results section.

After the cells were exposed to the laser, the PBS was replaced by 2 mL fresh, warmed medium (37°C) and the cells returned to the incubator.

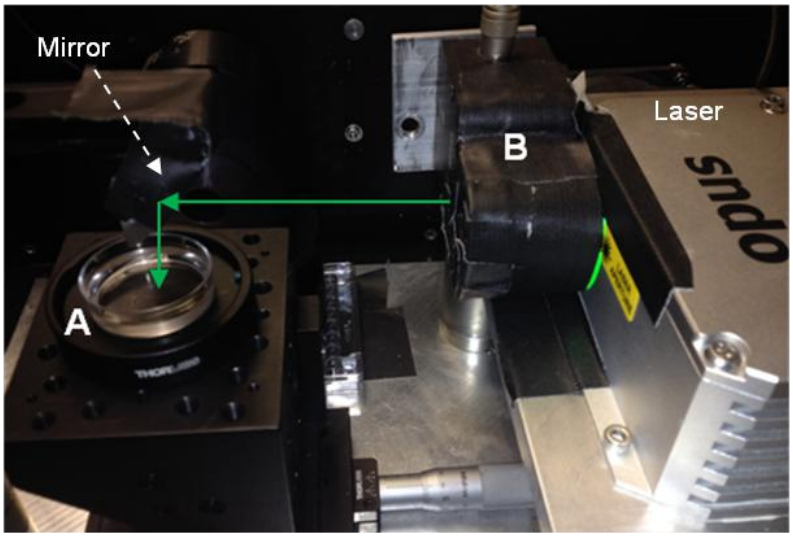

Figure 3.2: Laser Irradiation set-up (A) Cell culture dish placed on the translational stage; (B) Shutter; and the laser beam (green arrow) which hits a mirror and is directed vertically through the sample. There is a large aperture underneath the sample so that the beam is directed away and does not heat any part of the translational stage

3.1.2. Determining Cell Viability

Cell viability was determined using trypan blue, an exclusion assay. 1 mL of trypan blue (0.4% solution – Sigma Aldrich UK) was diluted with 1 mL (37°C) medium (DMEM – see Chapter 2.1.2), and after removing the medium that is already in the cell dish, this dye/medium mixture was added and the cells are put back in the incubator. After 5 minutes the dye/medium mixture was replaced with 2 mL fresh warmed medium (37°C), this washing step was repeated and the cells imaged using an optical microscope (as above). Cells with an intact membrane will exclude the dye, leaving only the dead cells dyed blue. However, blue colour is not the only criterion for cell death. Cells with significant morphological change are counted as dead, and some cells detach from the dish and so, using the images taken before the irradiation, these are also be counted as dead cells (examples of this are given in the results section).

The main analysis of the results will focus on the cells in the central 0.5 mm diameter (0.2 mm^2 area) of the area exposed to the laser beam. The laser intensity in this area is

relatively constant, as the intensity only drops to 86% of its maximum value at a distance of 0.25 mm from the centre of the beam (Figure 3.3).

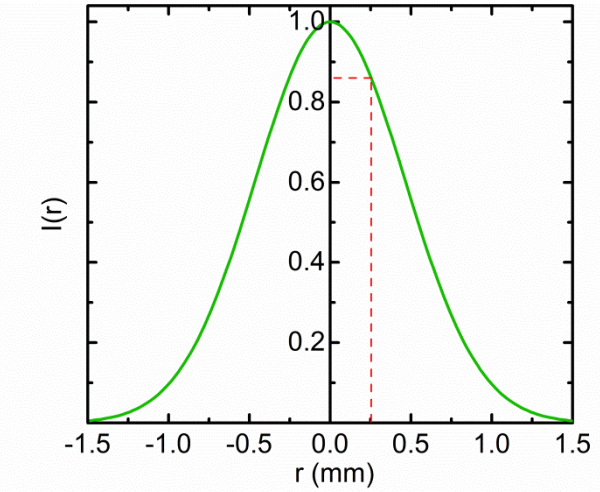

Figure 3.3: Typical Gaussian laser beam intensity profile
(Red dotted line indicates radial position 0.25 mm from beam centre)

The relevant area was defined by looking at the image of the cells taken after the trypan blue treatment and drawing a circle with a diameter of 0.5 mm around the centre of the dead cells; this is relatively easy when there is 100% cell death in the centre of the irradiated area, but becomes less reliable when there are only a few dead cells (examples of this are shown in the results section 3.2.2.). Once the area is defined, the corresponding area on the image taken before irradiation is marked and cells in both areas are counted and compared by hand.

Protocol development: The standard protocol was to determine cell viability 24 hours after laser irradiation. In some cases, cell viability was determined at regular intervals after irradiation; however, it was found that this repeated treatment with trypan blue could cause an extra 10% of the cells to die and so the standard protocol was to wait for 24 hours and it will be clearly stated if another protocol was used.

3.2. Results of HeLa Cell Irradiation

3.2.1. Control Experiments

3.2.1.1. Incubation of HeLa Cells with Gold Nanoparticles without Irradiation

The centre of the marker sticker described above (section 3.1.1.) was not only used for aligning purposes, but also used as a control area for each experiment. Images of the cells in this area (A) before, and (B) 24 hours after irradiation were taken. The expected cell proliferation (doubling time for HeLa cells is 24 hours) in this non-irradiated control area was always seen (Figure 3.4), this cell growth was visible at the edges of the irradiated areas (shown in the results below). This clearly shows that any cell death in the irradiated area is due to the irradiation.

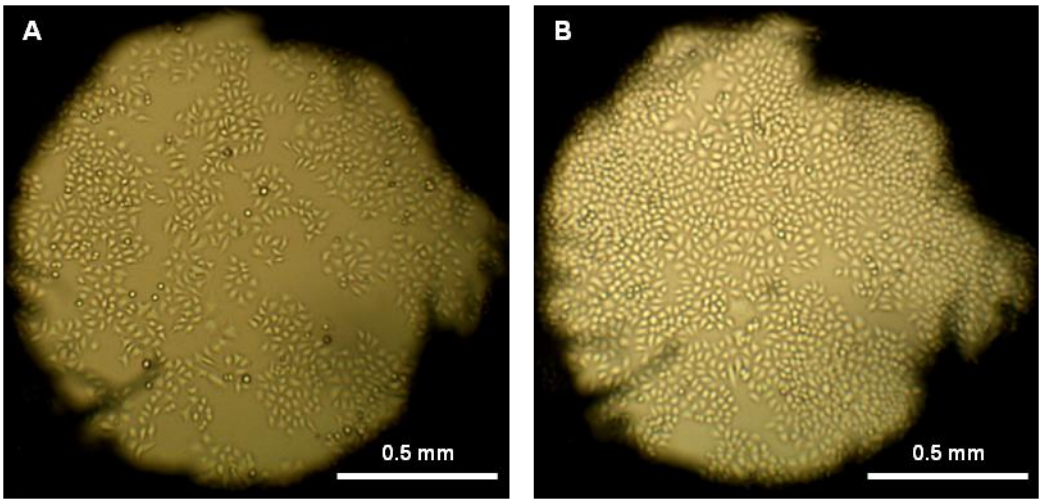

Figure 3.4: Non-irradiated control area; A) after incubation with 14 nm citrate gold NPs (3h, 2 nM) and B) 24 hours after irradiation (of areas 1-4) and trypan blue treatment.

3.2.1.2. Irradiation of Cells in the Absence of Nanoparticles

The effect of the laser irradiation on HeLa cell viability was determined by exposing cells to 3 W for 5 min, without prior incubation with gold NPs. Figure 3.5 shows HeLa cells (A) before and (B) 24 after irradiation and trypan blue treatment.

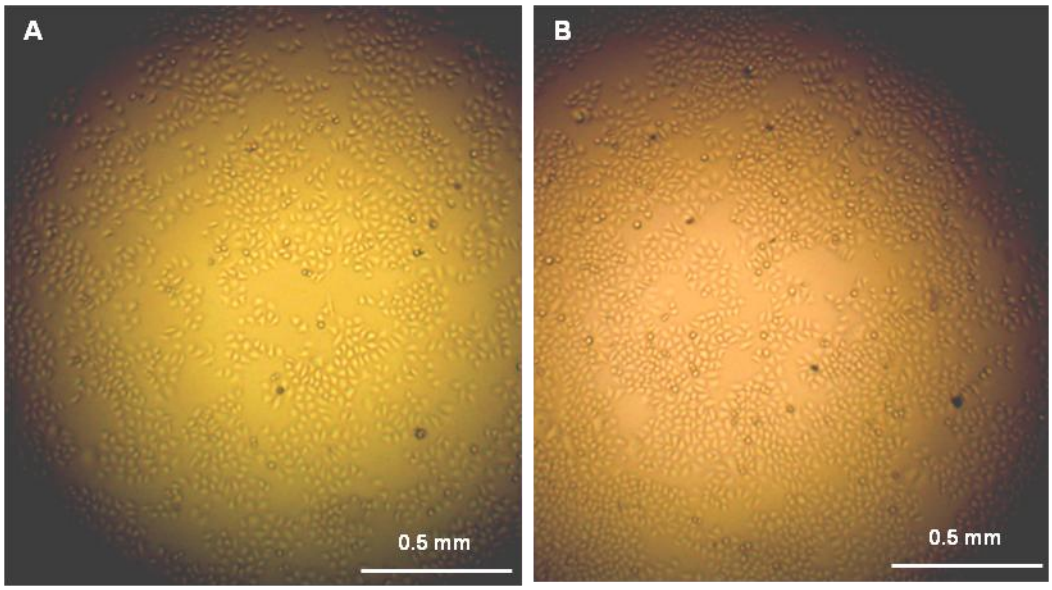

Figure 3.5: HeLa cells (without incubation with gold NPs); (A) before, and (B) 24 hours after irradiation (3 W, 5 min) and trypan blue treatment

The result of the experiment (Figure 3.5(B)) shows that there are no dead cells and the cell number has doubled overnight, as expected. The irradiation conditions used here are the highest power and longest exposure times used, the experiment was repeated several times with the same outcome and so it was concluded that in the absence of gold NPs the laser irradiation has no effect on the cell viability.

3.2.2. Irradiation of HeLa Cells after Incubation with Citrate Gold Nanoparticles

After incubation of HeLa cells with citrate gold NPs (3 hours, 2 nM), there are approximately 42,000 NPs in each cell (see Chapter 2.3.1.). Irradiation of these cells with a cw laser at 532 nm (wavelength overlapping with the NP plasmon absorbance at 520 nm) results in cell death, Figure 3.6 shows HeLa cells after incubation with citrate gold NPs (i.e. before irradiation) (A) and the same cells after trypan blue treatment at 24 hours after exposure to laser irradiation at 3 W for 3 min (B).

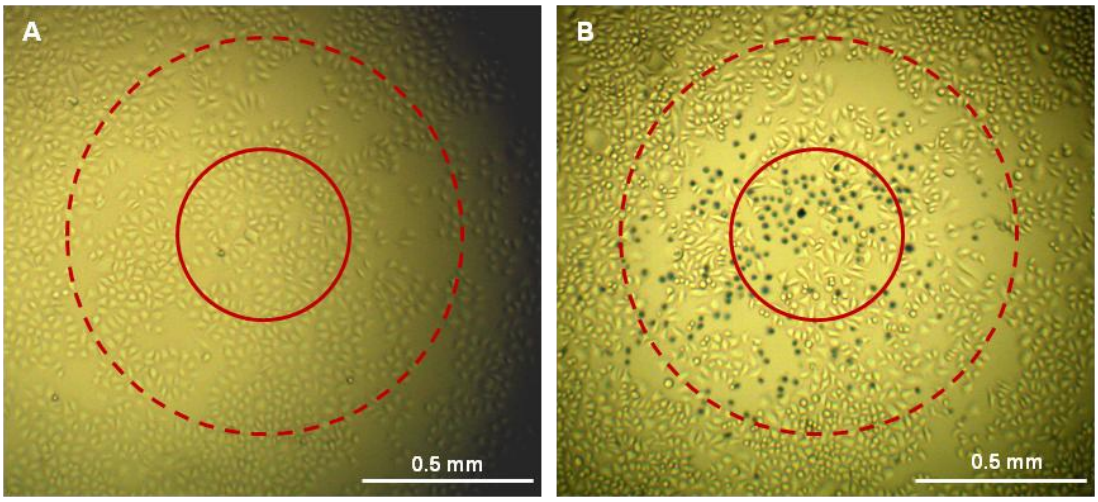

Figure 3.6: HeLa cells incubated with 14 nm citrate gold NPs (2nM, 3h), A) before and B) 24 hours after irradiation (3 W, 3 min) and trypan blue treatment. The diameter of the dashed circle is 1.2 mm and that of the solid circle is 0.5 mm which represents the affected area and the centre 0.5 mm diameter of the irradiated area, respectively.

The images in Figure 3.6 show how the areas in the results are defined, the dashed circle indicates the affected area, in this case it has a diameter of 1.2 mm, most cells within this area are either dyed blue, have distinct morphological changes, or have detached from the cell dish, and the majority of cells are not dividing at the same rate as the cells outside this area. The red solid circle with a diameter of 0.5 mm, indicates the centre of the laser beam where the laser intensity has dropped to just 14% of its maximum (Figure 3.3).

3.2.2.1 Delayed Onset of Cell Death

After irradiation, the cells do not die immediately, there is a delay. Figure 3.7 shows cells after trypan blue treatment at A) 10 min, B) 30 min and C) 24 hours after laser irradiation at 3 W for 5 min.

30 min after irradiation there are no dead cells whereas after 24 hours, *ca.* 33% of the cells have died; clearly, there is also less division in the irradiated area compared to the area outside. Further investigation into this delay was not carried out because of the extra cell death caused by the experimental procedure as described in 3.1.2.

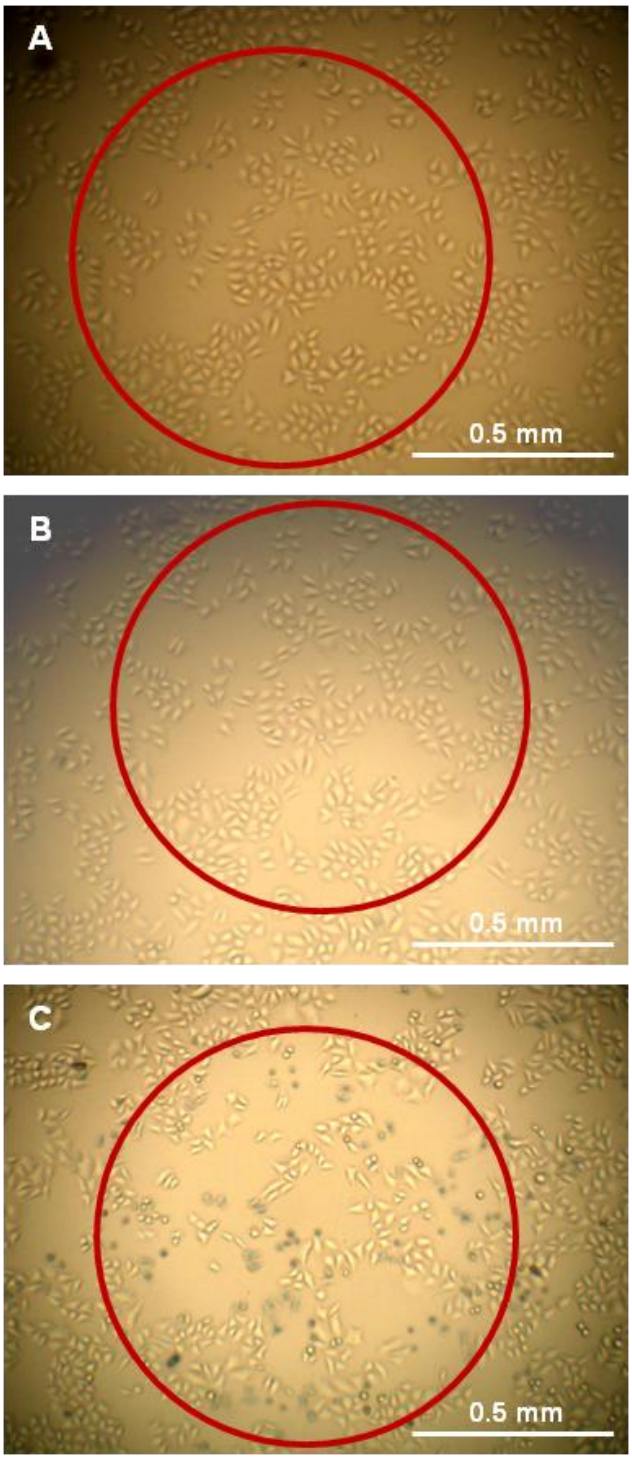

Figure 3.7: Cell viability determined A) 10 min, B) 30 min and C) 24 hours, after irradiation (1.5 W, 5 min) of HeLa cells incubated with 13 nm citrate gold NPs (3 h, 2 nM)

3.2.2.2 Variability of Effect

When cells in different areas on the same or in multiple dishes are irradiated using the same laser conditions, variation in cell viability was observed. This was observed even when analysis was restricted to the centre 0.2 mm^2 of the irradiated area (where the laser intensity is relatively constant – see Figure 3.3). This was seen in many experiments and to clearly demonstrate it, HeLa cells were seeded from the same dish into six 35 mm dishes, incubated using the same conditions (3 hours, 2 nM citrate NPs) and then three areas on each dish were exposed to 3 W laser light for 3 minutes. 24 hours later, cell viability was determined by counting the blue cells, missing cells and cells that had a dramatic morphological change. The fraction of dead cells in the centre 0.2 mm^2 of each irradiated area is given in Figure 3.8(A), the colours indicate the areas on the same dish. From the results given in Figure 3.8(A) it can be concluded that the order of irradiation (always X1, X2, X3) has no influence on the amount of cells dead or does not cause any trend in the variation.

Some examples of the results are shown in Figure 3.8(B), the red circle has a diameter of 0.5 mm and indicates the centre of the irradiated area. A1 and A2 are irradiated areas on the same dish, they had a similar number of cells in the centre, approximately 160 and 152 cells per 0.2 mm^2 (these cell counts are from before the irradiation, so 24 hours before the images presented) but the fraction of dead cells is not reproducible with 28 and 54% of the cells dead in the respective areas. Areas C3 and E2 contained approximately 120 cells in the centre circle and 24 hours after irradiation 93 and 60% of the cells are dead, respectively. This shows that cell confluency does not play a role in cell viability after irradiation; the reason for this variation is unknown.

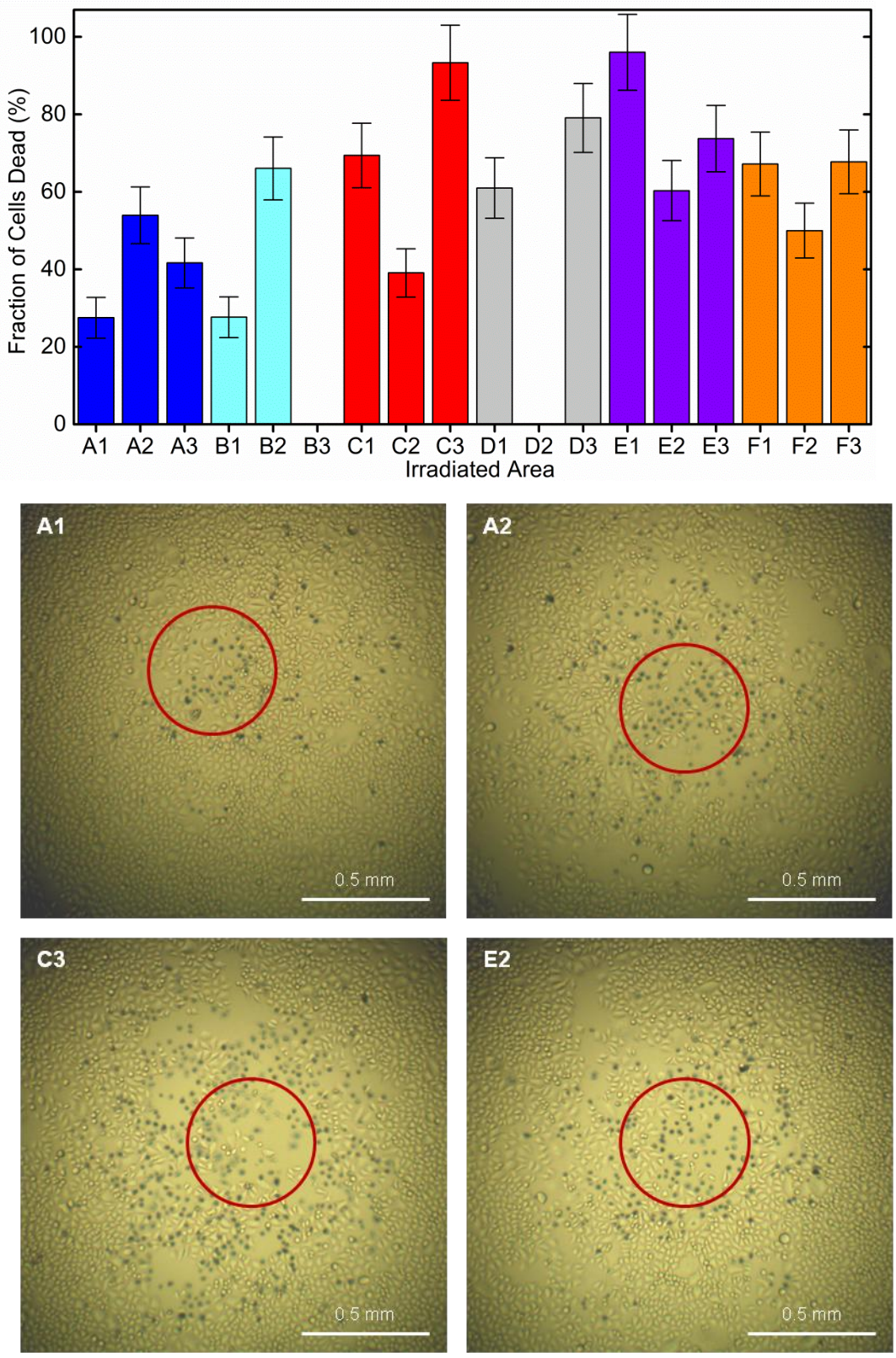

Figure 3.8: A) The percentage of dead cells in the centre 0.2 mm^2 of the irradiated area of HeLa cell cultures after incubation with citrate 15 nm gold NPs (3h, 2 nM) followed by irradiation at 3 W for 3 minutes. The colours and letters indicate the different cell dishes. The error bars are calculated from the statistical error. B) Images of 4 of the areas

3.2.1.3 Power Dependence

Despite the variations described above, a dependence of the fraction of cells killed by irradiation on the laser power can be demonstrated. Figure 3.9 shows a summary of the results, where the incubation conditions and exposure time was kept constant at (A) 3 minutes or (B) 5 minutes, respectively, and the irradiation power changed.

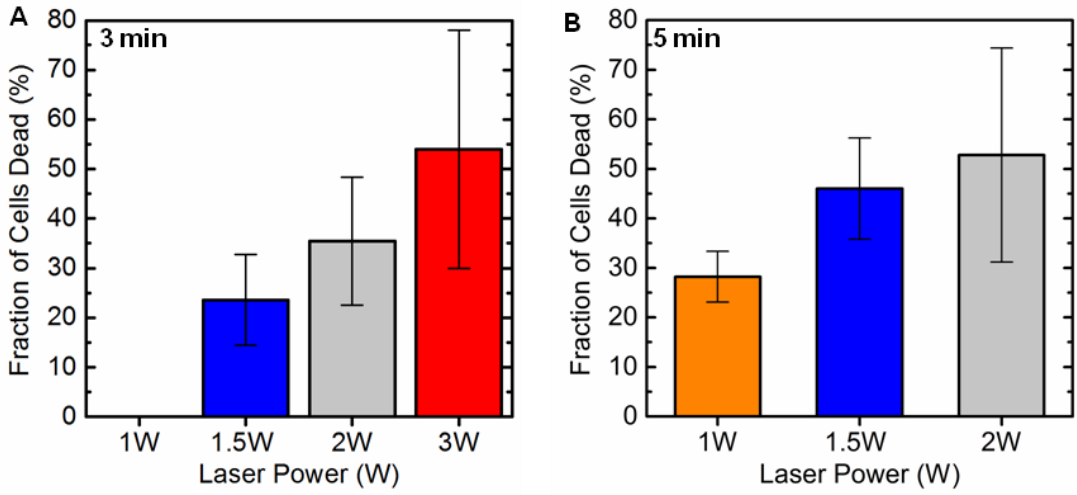

Figure 3.9: Summary of the cell viability in the centre 0.2mm^2 of the irradiated area after incubation with 14 nm citrate gold NPs (3h, 2 nM), where exposure time was constant at A) 3 minutes and B) 5 minutes and irradiation power was changed. Error bars are the standard deviation of multiple experiments, approximately 5-8 irradiated areas on 2-4 dishes.

As well as a power dependence there is also an exposure time dependence, Figure 3.9 shows that using the same power for 5 minutes increases the number of dead cells with respect to 3 minutes at the same power (2, 1.5 and 1 W), this time dependence was investigated in more detail, see next chapter. In general, increasing the irradiation power causes more cell death (the error bars in Figure 3.9 indicate the variation discussed in Chapter 3.2.2 and the conclusions drawn in this section are using the average values).

3.2.2.4 Irradiation Time Dependence

The time dependence was investigated by keeping the irradiation power constant and changing the exposure time. At 2 W, irradiating the cells for 2 minutes results in about 25% of the cells dying, increasing the time to 5 minutes increases the cell death on average to above 50% (Figure 3.10).

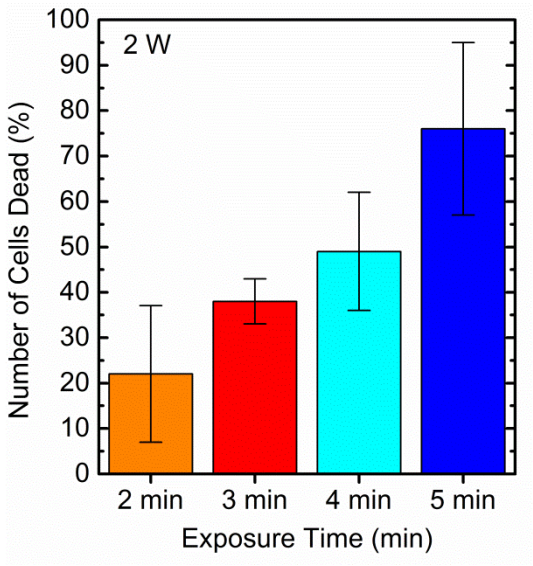

Figure 3.10: Summary of the cell viability in the centre 0.2mm^2 of the irradiated area after incubation with 14 nm citrate gold NPs (3h, 2 nM), after exposure to 2 W for different amounts of time. Error bars are the standard deviation of multiple experiments done on the same day.

In summary, irradiating HeLa cells after 3 hour incubation with citrate gold NPs results in significant cell death; there is variation in the results, but there is a general trend that higher irradiation powers and longer exposure times result in more cell death. Under all of the experimental conditions used here, viable cells were also found in the centre of the irradiated area.

3.2.2.5. 24 Hours Incubation of HeLa Cells with Citrate Gold NPs

Increasing the incubation time of HeLa cells with citrate gold NPs (2 nM) from 3 hours to 24 hours, results in approximately 320,000 NPs per cell (Chapter 2.3.1). Irradiation of these cells at 3 W for 3 min results in a well-defined area of dead cells, there is a very narrow area outside of this in which there are a mixture of dead and alive cells, and outside of that there are no dead cells (Figure 3.11).

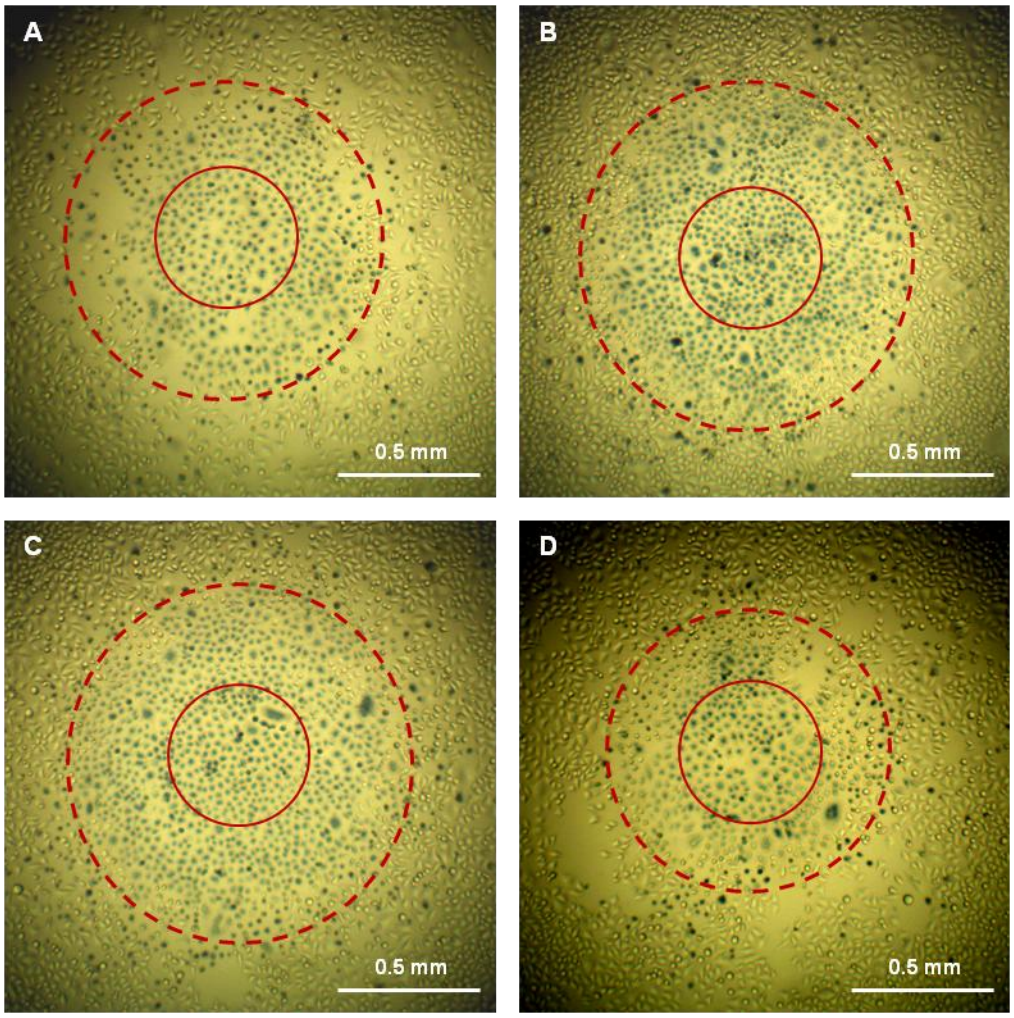

Figure 3.11: HeLa incubated with 14 nm citrate gold NPs (2nM, 24h) prior to irradiation (3W, 3 min). The images were taken 24 hours after laser exposure and after trypan blue treatment. The red solid circle indicate the centre 0.5 mm diameter of the exposed area and the dashed circle is indicating the area in which all of the cells are dead, outside of which there are a few dead cells

The examples in Figure 3.11 show that it is easier to define the centre of the exposed cells when the conditions used have caused all of the cells to die. The red solid circle indicates the centre and the dashed circle indicates the area in which all of the cells are dead, outside of this area there are a few cells dead with the majority alive. The diameter of the dashed circle in areas A-D is 1.1, 1.2, 1.2 and 1.0 mm, respectively.

Unlike the 3 hour citrate gold NP experiments, some of the cells die immediately after irradiation; Figure 3.12 shows the experiment (3 W, 3 min) with cell viability determined immediately after irradiation (A) and 24 hours later (B), the black dashed

circle has a diameter of 0.6 mm and indicates the area of cells that died during or immediately after irradiation.

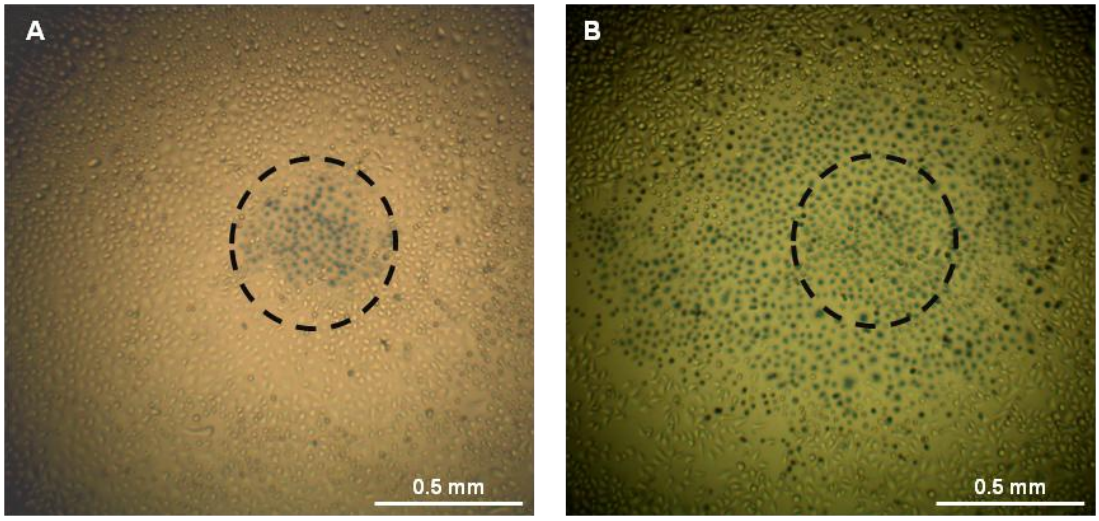

Figure 3.12: Cell viability determined A) immediately- and B) 24 hours- after irradiation (3 W, 3 min) of HeLa cells after incubation with 14 nm citrate gold NPs (24 h, 2 nM). The black dashed circle indicates area of cells that died during or immediately after irradiation (diameter = 0.6 mm).

3.2.3. Irradiation of HeLa Cells after Incubation with CALNN Gold Nanoparticles

In chapter 2, the quantitative uptake results of various incubation conditions of HeLa cells with CALNN gold NPs were investigated. However, irradiation experiments were only undertaken on cells after incubation for 3 hours at a final concentration of 4 nM, resulting in approximately 220,000 NPs/cell.

3.2.3.1. Power and Time Dependence

3W, 3 minutes: Laser irradiation of HeLa cells incubated with CALNN gold NPs result in a well defined area of dead cells in every experiment. Figure 3.13 shows the cells 24 hours after irradiation (and trypan blue treatment).

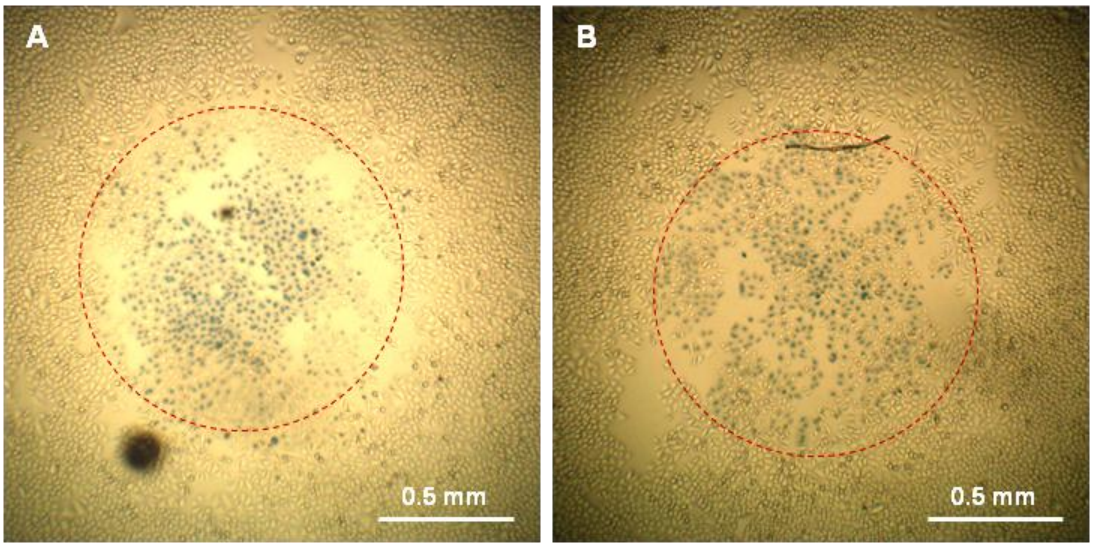

Figure 3.13: Cell viability results of HeLa cells incubated with 14 nm CALNN gold NPs (4nM, 3h) prior to irradiation (3W, 3 min). The red circle represents the area of cells that are dead, which has a dimaeter of 1.2 mm for A and B, which are areas irradiated on different cell dishes.

In the examples in Figure 3.13, it can be seen that it is not just the cells in the centre of the exposed area that are dead, each image shows a well-defined area (red dashed circles) in which all of the cells are dead, whereas cells outside this area are alive, with only a very narrow transition region where dead and alive cells are found; this contrasts with the experiments with citrate gold NPs, where the affected area contained a mixture of dead and alive cells. The diameter of the area of dead cells in Figure 3.12 is 1.2 mm for both A and B. More results are given in table 3.1 and in Appendix 3 – Table A3.9.

3 W, 1 minute: Reducing the exposure time from 3 min to 1 min (at 3 W) results in some experiments where there is a well-defined area of dead cells and other experiments where irradiation has had no effect. Examples of the results are shown in Figure 3.14. Areas A and B have no dead cells and the approximate cell confluency is 325 and 470 cells mm^{-2} (cell count done before irradiation i.e. 24 hours before these images), the cells have divided overnight and there is no indication of cell death. Areas C and D have a higher cell confluency with approximately 940 and 1250 cells mm^{-2}, laser irradiation of

these cells resulted in a well defined area with diameters of 0.68 and 0.8 mm respectively, of dead cells.

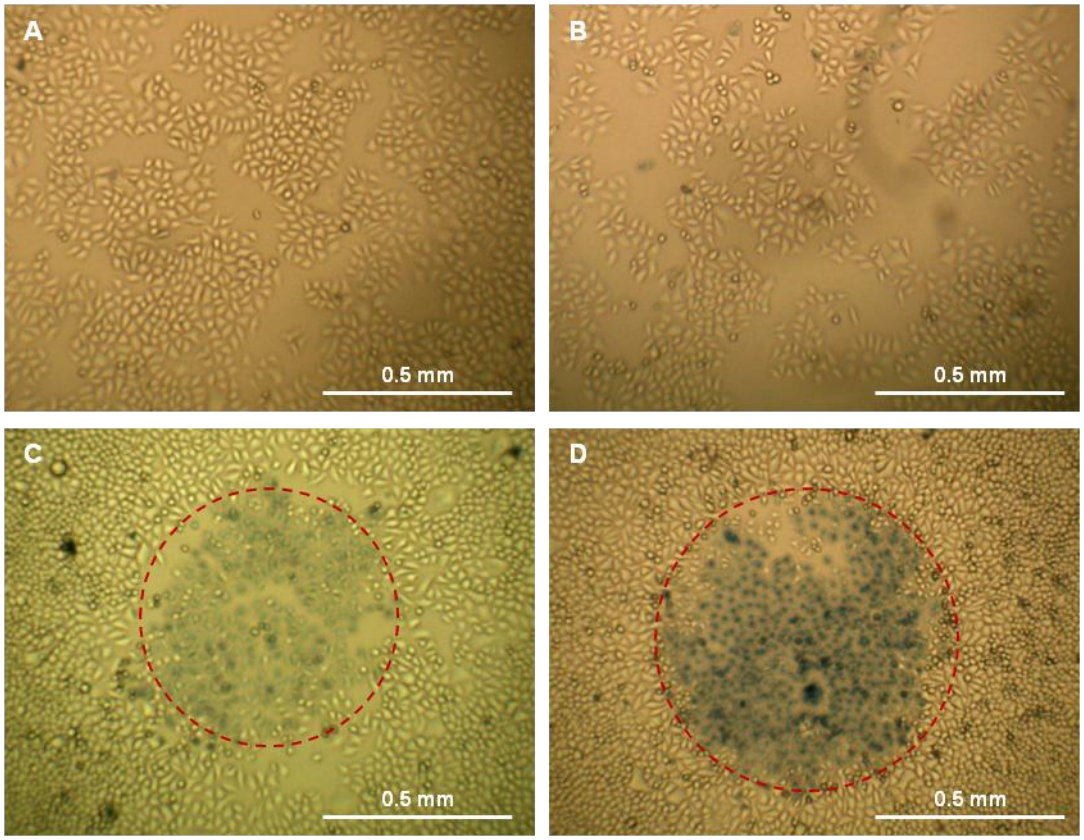

Figure 3.14: Cell viability results, 24 hours after irradiation (3 W, 1 min) of HeLa cells that had been incubated with 14 nm CALNN gold NPs (3 h, 4 nM). A and B): there are no dead cells and the confluency (before irradiation, ie. 24 hours before these images) was approximately 325 and 470 cells per mm^2. C and D) show an area of dead cells marked, with a red dashed circle with a diameter of 0.68 and 0.8 mm, respectively, the confluency of cells in these experiments was 940 and 1200 per mm^2

This pattern of confluency based cell death was seen repeatedly and all of the experimental results are given in the Appendix 3 – Table A3.7.

2 W 3 min: Reducing the irradiation power to 2 W, but keeping the irradiation time at 3 minutes, also results in confluency-dependent cell death (Figure 3.15).

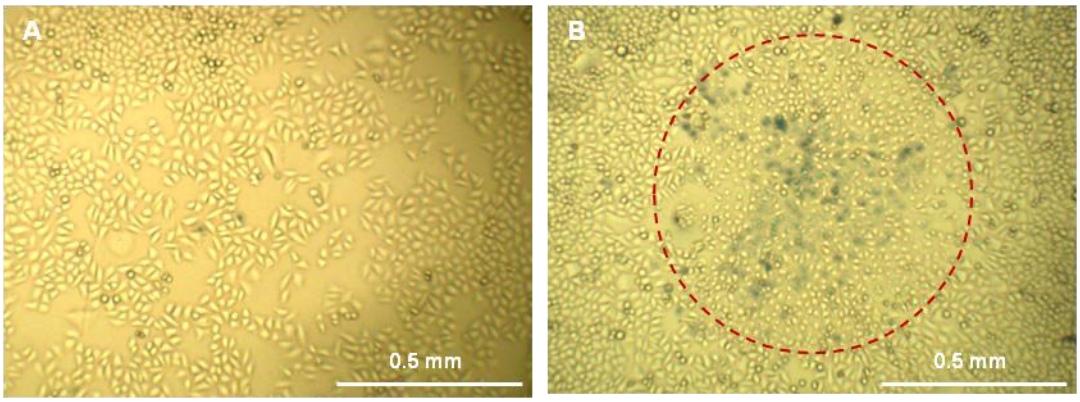

Figure 3.15: Cell viability results, 24 hours after irradiation (2 W, 3 min) of HeLa cells that had been incubated with 14 nm CALNN gold NPs (3 h, 4 nM). A) There are no dead cells and the confluency was approx. 325 cells mm^{-2}, and B) the red dashed circle indicating the area of dead cells has a diameter of 0.9 mm and the cell confluency was appox. 1350 cells mm^{-2}

The cell confluency in Figure 3.15(A), before irradiation, was *ca.* 580 cells mm^{-1} and in (B), where there is a distinct area of dead cells, the confluency was *ca.* 1350 cell mm^{-2}, the red circle indicating the affected area has a diameter of 0.9 mm.

1 W: Exposing CALNN gold nanoparticle loaded cells to irradiation at 1 W power for 3 or 5 minutes did not result in any cell death, the experiment was repeated multiple times with cells at different confluency (see appendix), but it can be concluded that an incident power of 1 W is not high enough, at least at the exposure times used here, to induce cell death.

3.2.3.1. Cell Death Delay

As with the 3 hour citrate gold NP irradiation experiments (Figure 3.7), there is a delay in cell death after exposure to 3 W for 5 min of HeLa cells incubated with CALNN gold NPs (3 h, 4 nM). Cell viability was determined 5, 15, 20, 40, 55, 70, 110, 200 min after irradiation and then 24 hours later; Figure 3.16 shows the results (5- and 15- min results not shown). The results show that the cells in the centre of the irradiated area start to die 20-40 min after irradiation.

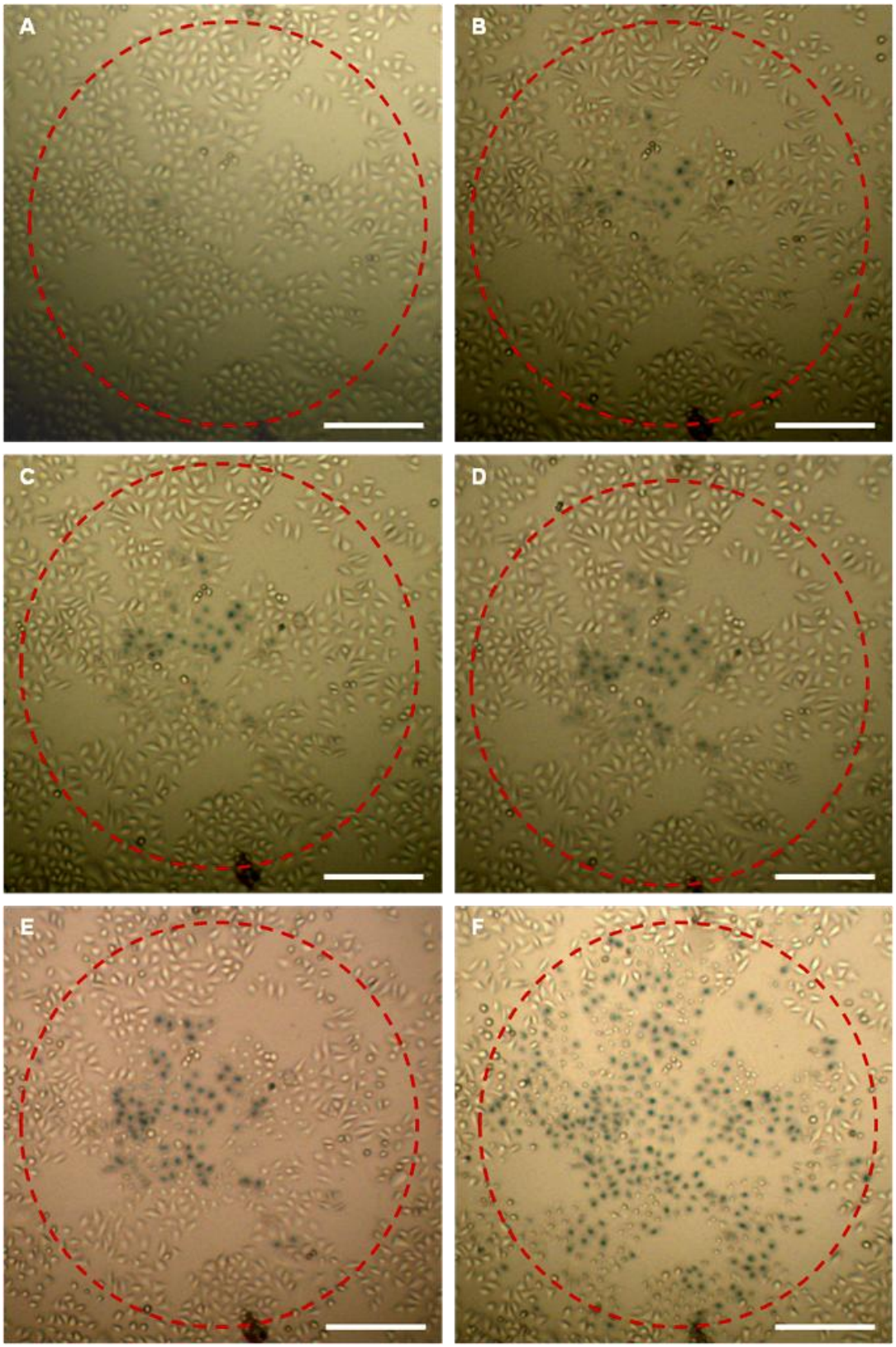

Figure 3.16: Cell viability determined; A) 20 min, B) 40 min, C) 55 min, D) 70 min, E) 200 and F) 24 h after irradiation (3 W, 5 min) of HeLa cells incubated with 13 nm CALNN gold NPs (3 h, 4 nM). The scale bar in all of the images is 0.2 mm

3.2.4 Killing HeLa Cells in a Water Bath

HeLa cells cultured in a 35 mm petri dish were taken from the incubator, the cell culture medium removed and 2 mL PBS added. The dish was then sealed with parafilm and submerged in a water bath for 5 minutes. Cell viability was determined the next day using trypan blue. When the temperature inside the dish was recorded by clamping a thermocouple to the bottom of the dish that contained 2 mL PBS, it took less than 3 minutes to reach the water bath temperature; as the cells are on the bottom of the dish, it will take less time for them to reach the temperature.

When the water bath was set to 40°C, the cells survived and cell division occurred over night. Increasing the temperature to 50°C resulted in the cells not dividing over night and increasing it to 55°C resulted in all of the cells being killed.

3.3. Discussion of the Irradiation Results

As discussed in the introduction, it has been widely reported that irradiating NPs attached to the cell surface, or internalised by the cell, at high enough laser powers to cause a large temperature increase can kill cells.[8, 28, 50] Alternatively, non-thermal irradiation routes have also been reported.[55] For this reason it is important to start the analysis estimating the temperature rise during irradiation.

3.3.1. Dynamic Simulations of Temperature Rise

Dynamic Simulations to estimate the laser-irradiation induced temperature increase for the experiments in this chapter were performed by M. Volk using the same method as published.[55] Numerical heat transport simulations were carried out which yield the explicit time-dependent temperature distribution after starting irradiation, these simulations are based on the Fourier heat equation (Equation 3.1).

$$\rho c \frac{\partial T}{\partial t} = \kappa \nabla^2 T + \frac{dq}{dt}$$

Equation 3.1: Fourier heat equation

In equation 3.1, ρ, *c* and κ are the density, heat capacity and heat conductivity of the medium and T is the temperature. dq/dt represents a source term, q is the heat that is released rapidly to the surrounding medium as a result of the absorbed laser energy. The laser light absorbed is estimated from the absorbance of the sample, which can be estimated from the NP per cell, cell per mm and the extinction coefficient (ε) of the NPs, which for 14 nm spherical NPs is 2.85 10^8 M^{-1} cm^{-1}, [70] this is shown in chapter 2.3.1.

It is the cumulative heating from the NPs in different cells that leads to an increase of the sample temperature in the area of the laser beam. Using cylindrical symmetry for the modelling, this macroscopic heating of the buffer solution above the cells is estimated. The total volume used for the simulations is a cylinder of 12 mm radius and 2.5 mm height (depth of the 2 mL buffer above the cells in a 35 mm cell culture dish). Heat is assumed to be generated proportional to the Gaussian beam profile ($1/e^2$ diameter = 1.85 mm) in a 5 μm thick layer (cell thickness). The dish base and wall were assumed to be thermally insulating.

The results of the simulation for irradiation at 3 W for a cell monolayer absorbing 0.5% (a typical value for the experiments using citrate NPs, see chapter 2.3.1.3) of the incident irradiation are given in detail here.

Figure 3.15 shows contour plots of the spatial temperature rise distributions of the buffer layer at different exposure times, the temperature rise is highest in the centre of the laser beam and heat energy flows upwards and outwards. The colour scale gives the temperature increase above the surrounding temperature (RT).

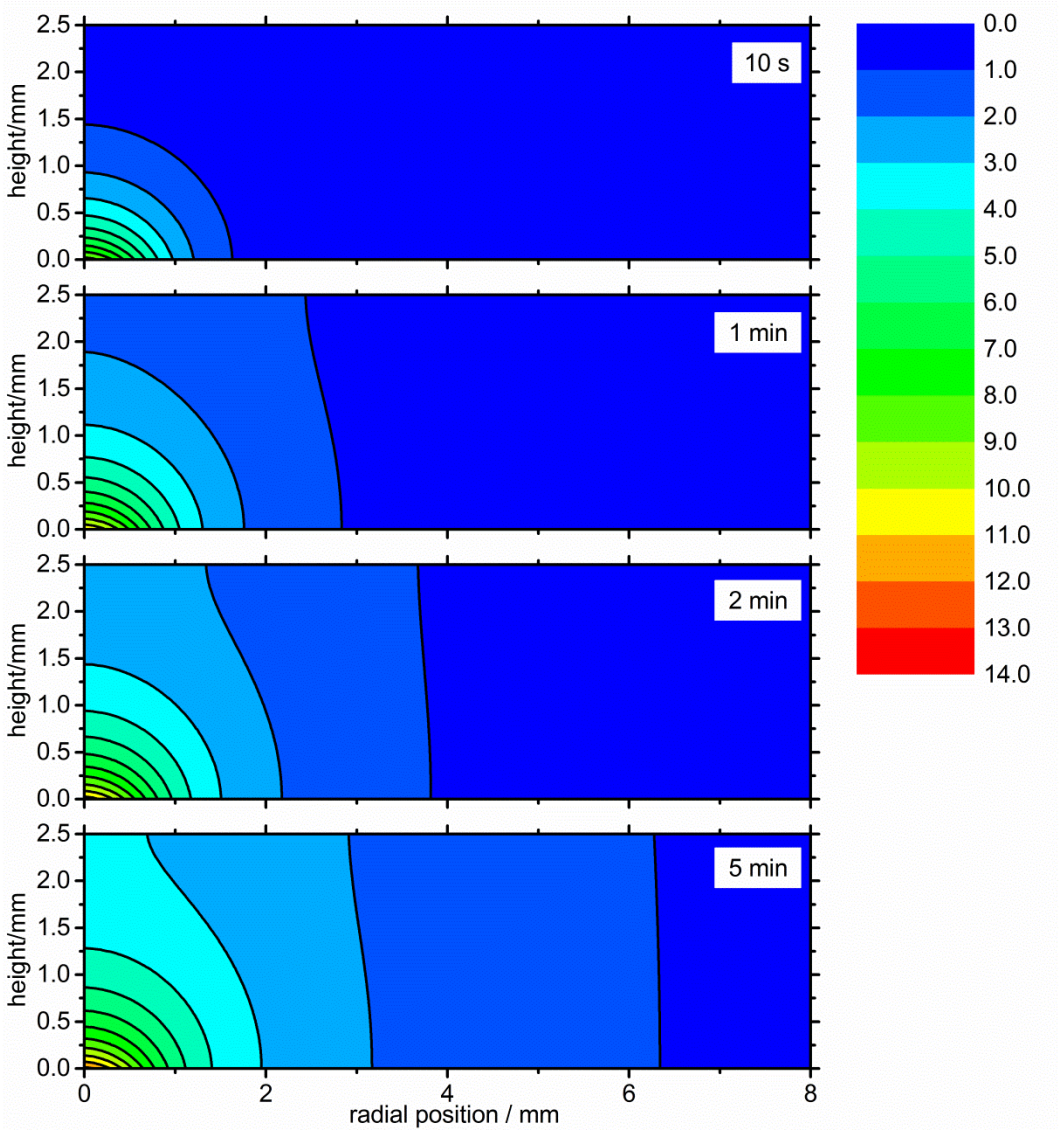

Figure 3.17 Spatial temperature rise distribution in the buffer layer above background temperature after exposure to 3 W irradiation for different amounts of time, assuming that 0.5% of the incident light is absorbed by the cell layer. The colour scale gives the temperature increase above the background temperature.

The maximum temperature rise, i.e. the temperature of the cells in the centre of the irradiated area, is given as a function of irradiation time in Figure 3.17 which shows that the temperature increases rapidly in the first 30 seconds of irradiation, after which there is not much change to the temperature. The maximum temperature rise above background at 10 seconds after turning the irradiation on is *ca*. 9°C and it increases to *ca.* 12°C after 3 minutes.

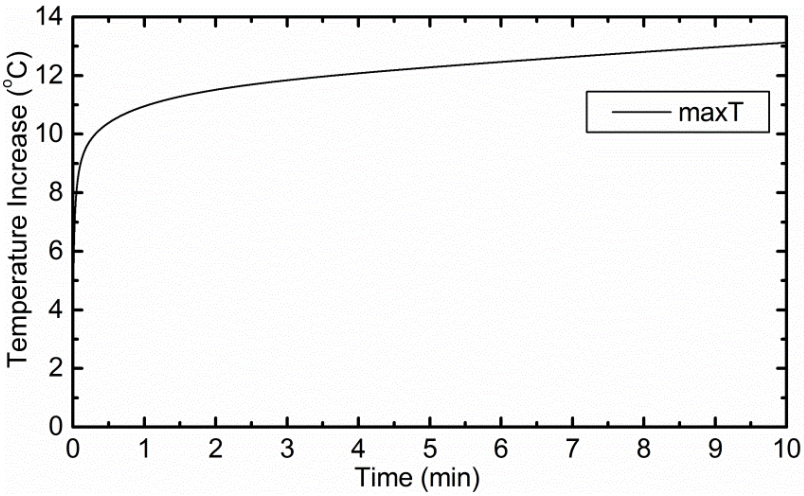

Figure 3.18: Time dependence of the temperature increase in the HeLa cell monolayer at the centre of the laser beam after turning on irradiation at 3 W, assuming that 0.5% of the incident light is absorbed by the cell layer.

Figure 3.19 shows the temperature rise at the bottom of the dish (i.e. the cell layer) as a function of distance from the centre of the laser beam, it is given for irradiation power 3 W and different exposure times.

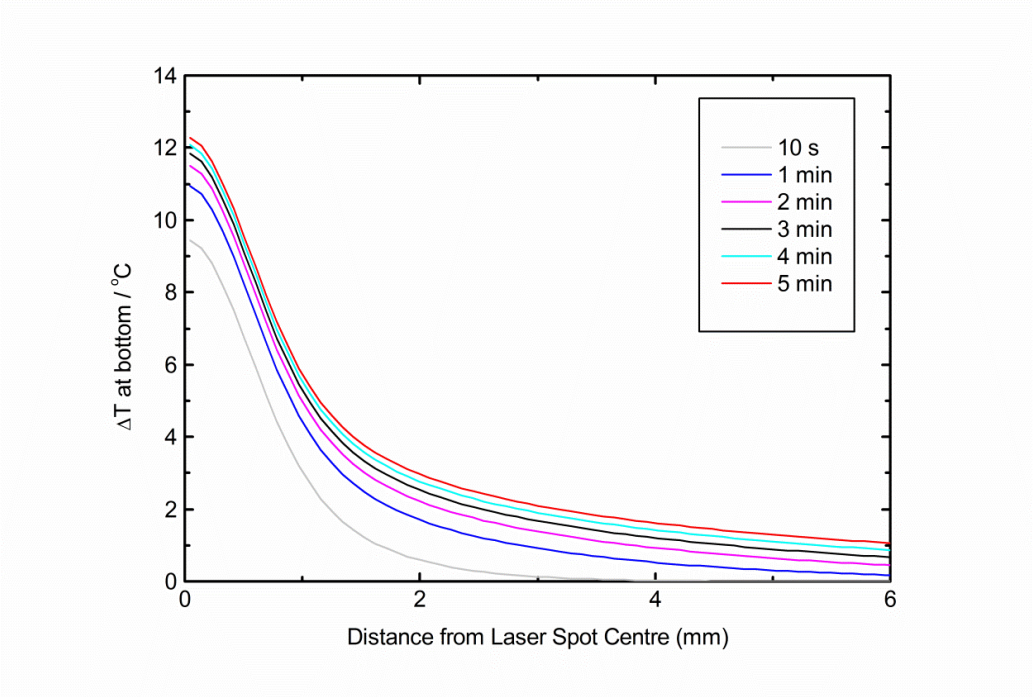

Figure 3.19: Temperature dependence in the HeLa cell monolayer as a function of distance from the centre of the laser beam after irradiation for different exposure times at 3 W, assuming that 0.5% of the incident light is absorbed by the cell layer.

Scaling the Simulation Results

The simulation results can be scaled to estimate the expected temperature increase in the experiments described in this chapter. The simulations are using an incident power of 3 W and so can be directly scaled for the power. The fraction of light absorbed (hence the scaling factor compared to 0.5% used above) can be calculated using the NP extinction coefficient, the number of NPs per cell and counting the number of cells per mm^2 in the laser beam area (Chapter 2.3.).

The estimated temperature during irradiation for every experiment with CALNN- and citrate- gold NPs are given in tables A3.1-A3.9 in appendix 3. Examples of some of these results are shown below in Tables 3.1 – 3.3. The tables include; irradiation conditions used (power and exposure time), the figure reference (where applicable), the number of cells - and the fraction dead at 24 hours after exposure - in the centre circle with 0.5 mm diameter of the exposed area and the calculated absorbance of the cell monolayer (see Chapter 2.3). Finally, the estimated maximum temperature (in the centre of the laser beam) of the cells during irradiation, calculated using the simulations above, is given for every experiment and for experiments that result in a well-defined area of dead cells, the diameter of that area and the calculated temperature of the cells at that diameter during irradiation is given.

3.3.2. Cell Killing Using CALNN Gold Nanoparticles

In section 3.2.3, irradiation of HeLa cells after incubation with CALNN gold NPs (3h, 4 nM – resulting in approx. 220,000 NPs $cell^{-1}$) showed that in some experiments cells died and in others the irradiation had no effect on cell viability.

1 W (3 min and 5 min): Irradiating the cells at 1 W for 3 or 5 minutes did not result in cell death in any of the experiments; table 3.1 gives some example results of the estimated maximum temperature of the cells during irradiation.

For the examples given in table 3.1, the estimated maximum temperatures during irradiation are 35, 39 and 28°C; as shown by the water bath experiment (3.2.4), a threshold temperature of 50-55°C is needed to kill the cells thermally, and so none of the reported temperatures are high enough to kill the cells by hyperthermia. The full results table (A3.3-A3.4) is given in Appendix 3, which shows the maximum temperature in all of the experiments is below 50°C, which is why no killing is observed in any experiments under these conditions.

			Centre (0.5 mm diam.)					
Power (W)	**Time (min)**	**Fig.**	**No. of Cells**	**Fraction of cells dead(%)**	**Diam. of Area of Dead Cells (mm)**	**Calc. Abs. (mOD)**	**Max. Temp. (°C)**	**Temp. at the Edge of Area of Dead Cells (°C)**
1 W	3 min	-	142	0	-	7.5	35	-
1 W	3 min	-	185	0	-	9.8	39	-
1 W	3 min	-	70	0	-	3.7	28	-
2W	3 min	3.15A	270	100	0.9	14.3	70	61
2W	3 min	3.15B	116	0	-	6.1	43	-
3 W	1 min	3.14A	233	100	0.8	12	80	70
3 W	1 min	3.14B	188	100	0.7	10	69	64
3 W	1 min	3.14C	65	0	-	3.4	38	-
3 W	1 min	3.14D	94	0	-	5.0	45	-
3 W	3 min	3.13A	168	100	1.2	8.9	67	54
3 W	3 min	3.13B	206	100	1.2	10.9	77	61

Table 3.1: Examples of the results and estimated temperature rise for irradiation of HeLa cells after incubation with CALNN gold NPs (3h, 4 nM) at the given conditions. The fraction of dead cells in the centre of the irradiated area and the diameter of the well-defined area of dead cells determined at 24 hours after irradiation is given. The calculated absorbance of the cell monolayer, the estimated maximum temperature and the temperature at the edge of the area of dead cells during irradiation is also given.

Table 3.1 gives the estimated maximum temperature during irradiation, at **2 W for 3 min**, for the results shown in Figure 3.15. For area A, where no cell death was observed, the estimated maximum temperature is 43°C, indeed predicting no cell death. Area B, on the other hand, results in a well-defined area of dead cells with a diameter of 0.9 mm, as indicated by the red dashed circle and indeed the maximum temperature estimated for

area B is 70°C, whereas the temperature at the edge of the area of dead cells is estimated to be 61°C, close to the 55°C at which cell death has been observed in the water bath experiments. In table A3.6 of appendix 3, all of the experimental results for 2 W irradiation are given, which show a wide variability of cell death; for the experiments that result in cell death, the average temperature at the edge of the dead cells (i.e. the lowest estimated temperature that killed the cells) is 54°C, this is in excellent agreement with the water bath experiment, where it was shown a threshold value of 50-55°C is required to kill the cells by hyperthermia.

3 W 1 min: Figure 3.14 shows the results of cell viability determination at 24 hours after irradiation at 3 W for 1 min, experiments A and B show that irradiation under these conditions had no effect on cell viability, whereas experiments C and D have a well-defined area of dead cells with a diameter of 0.7 and 0.8 mm respectively, (indicated by the red dashed circle). The estimated maximum temperature for A and B (see table 3.1) is 38 and 45°C whereas for C and D it is 80 and 69°C, again cell death only occurs when the temperature during irradiation is high enough to cause death by hyperthermia. The average temperature at the edge of the area of dead cells for these experiments (those in table 3.1 and appendix 3 – table A3.7) is 68°C, this is somewhat higher than the threshold temperature determined to kill the cells using a water bath (50-55°C, 3.2.4) or in the 2 W, 3 minute irradiation experiments. However, the cells in the water bath experiment were at the elevated temperature for at least 3 minutes, here, it takes 30 s to reach the maximum temperature during irradiation (Figure 3.18), and as the exposure time is only 1 min it means that the cells are only at those temperatures for approximately 30 s.

Irradiation at **3 W 3 min** always resulted in an area of dead cells; Figure 3.13 gives two examples of cell viability determined at 24 hours after irradiation. The estimated maximum temperature for those experiments is 67 and 77°C (see table 3.1) and the

average maximum temperature of all of the experiments at this power (see appendix 3 – Table A3.9) is 63°C. The average temperature during irradiation of the cells at the edge of the defined area of dead cells (appendix 3 - table A3.9) is 53°C; this is in excellent agreement with the threshold 50-55°C determined by the water bath experiments in 3.2.4.

Irradiation of CALNN gold NP-loaded HeLa cells was also done at **1.5 W 3 min** and **3 W 2 min**, the results are shown in appendix 3 table A3.5 and A3.8, respectively. The results of these experiments follow the trend described above, cell monolayers with a high enough absorbance to absorb enough energy and increase the temperature to at least *ca*. 50-55°C during irradiation results in cell death, if this temperature is not reached during irradiation, then cell viability is not affected.

Using all of the experimental results (see appendix and table 3.1), it can be concluded that cell death caused by laser irradiation of HeLa cells after incubation with CALNN gold NPs (3h, 4 nM) is due to thermal effects - if a threshold temperature of 50-55°C is not reached during irradiation, then cell viability is not affected. All of the cells in the area where the threshold temperature is reached die, this is unlike citrate gold NP experiments where dead and alive cells are often found in the same area.

The results above are in good agreement with those reported by El-Sayed and co-workers,[6, 8, 46] they show that a threshold temperature of 70-80°C is required to induce hyperthermia by laser irradiation of two types of cancerous cells (HOC and HSC) as well as healthy cells (HaCaT); they confirmed this temperature by heating cells in an oven. However, they determined cell viability immediately after irradiation (or heating in the oven), whereas the results above, where a much lower temperature threshold (50-55°C) to induce hyperthermia is reported, are based on cell viability results determined 24 hours after irradiation or submergence into a water bath (see 3.2.2, 3.2.3 and 3.2.4).

This indicates that temperatures of 70-80°C are required to kill cells immediately, whereas there is a delay in cell death after cells are heated to between approximately 50-70°C. This is supported by the delay in cell death after irradiation shown in Figure 3.16; cells irradiated at 3 W for 5 min, resulting in a maximum temperature of ca. 67°C during irradiation at the centre of the laser beam, start to die at 20-40 minutes after laser exposure; whereas, cells further from the centre, and thus heated to lower temperatures, only die at a later time, although 100% of the cells exposed to 50-55°C are dead after 24 hours. Similarly, the results of the experiments using 24 h incubation with citrate gold NPs shown in Figure 3.12, which also are ascribed to a photothermal mechanism (see below), where the maximum temperature during irradiation is approximately 95°C (see table 3.4 below) results in an area of cells killed during or immediately after irradiation (Figure 3.12A), the diameter of the area (indicated by the black dashed circle) is 0.6 mm and the estimated temperature at this diameter is 71°C; outside of this area, cell death occurs up to 24 hours later (Figure 3.12B).

3.3.3. Cell Killing Using Citrate Gold Nanoparticles

3.3.3.1 3 hour Incubation Experiments

In Figure 3.8, examples of the results of irradiation at **3 W for 3 min** of cells after incubation with citrate NPs (3 h, 2 nM) are given. In each area A-D, there is some degree of cell death; however, these areas are not well defined and contain a mixture of dead and alive cells. The estimated maximum temperature of these cells during irradiation is 28-30 °C (table 3.2). More results are given in the appendix 3 – tables A3.1(A&B), confirming that the maximum temperature does not even reach 37 °C for any of the experiments (the optimum temperature for cells). As there is no well-defined area of dead cells after irradiation, this column is not reported in table 3.2 (and in appendix table A3.1).

	Centre (0.5 mm diam.)			
Figure 3.8 /Area	Number of cells	Fraction of Cells Dead	Calc. Abs (mOD)	Max T. (°C)
A1	160	28	1.6	30
A2	152	54	1.5	30
C3	120	93	1.2	28
E2	121	60	1.2	28

Table 3.2: fraction of dead cells at 24 hours after laser exposure for HeLa cells incubated with citrate gold NPs (3 h, 2 nM) and irradiated (3 W, 3 min), also given are the calculated absorbance of the samples and the estimated maximum temperature during irradiation (these results correspond to those given in Figure 3.8 and the full table of results for all of the experiments is given Appendix 3 – Table 3.1(A&B))

After incubation of HeLa cells with citrate gold NPs, at a final concentration of 2 nM for 3 hours, there are approximately 42,000 NPs cell^{-1}, this number is ~5 times lower than the value reported for the CALNN incubation experiments and so the maximum temperature during irradiation is, as expected, much lower. Interestingly, the fact that cells die during irradiation, when temperatures do not reach those capable of killing cells by hyperthermia, means that the mechanism of cell killing is not photothermal and the conclusion is it must be photochemical.

Further supporting that statement are the differences between the experiments using CALNN gold NPs, where the cells were killed thermally, and the experiments using citrate gold NPs (using 3h, 2nM incubation conditions). Firstly, the experiments using citrate gold NPs resulted in an affected area which included dead cells and alive cells, whereas for the experiments using CALNN gold NPs, cell death occurred in a well defined area containing only dead cells with a very narrow transition area outside of this containing a few dead and alive cells. The contour plots (Figure 3.17) shows that the temperature rise is highest in the centre of the laser beam and heat energy flows upwards and outwards into the surrounding medium. This means that for a given volume the temperature is quite homogenous, if this temperature is above the threshold required to kill cells thermally, then all of the cells in this area are affected, giving a defined area of dead cells. A photochemical method could result in cells in the same area affected

differently, depending on the total uptake and/or the distribution of the NPs in individual cells, this is because the photochemical reaction occurs inside of the cell, and there is no cumulative effect over an area of cells like that for heating.

Secondly, cell confluency is a determining factor of cell death in the experiments using CALNN gold NP; cell death can be predicted, using the number of cells per mm^2, the number of NPs per cell and the simulations. As shown in table 3.1 there is a direct relationship between cell confluency and the amount of light energy absorbed (Chapter 2.3.1.3), a higher cell confluency means that there are more NPs per unit area and so more incident irradiation is absorbed and released as heat energy, increasing the temperature reached during irradiation. For CALNN gold NP experiments, the light absorbed has to be sufficient to raise the temperature during irradiation at least to a threshold of 50-55°C to result in cell death. On the other hand, for the experiments using citrate gold NP it was shown in 3.2.2.2 that cell death has no correlation with confluency. This is because the proposed photochemical effect is a local effect, dependent on the number of NPs per cell, independent of the cell nearby, whereas the photothermal effect rests on the cumulative effect of all cells, and so confluency obviously plays an important role.

3.3.3.2. 24 hour Incubation Experiments

Incubating HeLa cells for 24 hours with citrate gold NPs (2 nM) results in approximately 320,000 NPs $cell^{-1}$ (Chapter 2.3). Irradiation of these cells at **3 W for 3 min** results in a well defined area of dead cells at 24 hours after irradiation, examples of which are shown in Figure 3.11. The calculated maximum temperature and the temperature of the cells at the edge of the area of dead cells for these experiments are given in table 3.3 and are 68-99°C and 55-73°C, respectively. The temperatures during irradiation for these experiments and all of the results under these conditions (appendix 3

– table A3.2) are above the threshold 50-55°C reported to kill cells (3.2.4). This indeed means that these cells are killed by a photothermal method, very similar to the CALNN gold NPs experiments reported above. The number of NPs per cell is very similar for both of these conditions.

	Centre (0.5 mm diam.)					
Figure 3.11	**No. of Cells**	**Fraction of cells dead (%)**	**Diam. of Area of Dead Cells (mm)**	**Calc. Abs. (mOD)**	**Max. Temp. (°C)**	**Temp. at the Edge of Area of Dead Cells (°C)**
A	137	100	1.0	8.9	68	55
B	230	100	1.0	14.9	99	73
C	212	100	1.2	13.7	93	69
D	173	100	1.1	11.2	80	66

Table 3.3: Fraction of dead cells in the centre of the laser beam and the diameter of the well-defined are of dead cells at 24 hours after laser exposure for HeLa cells incubated with citrate gold NPs (24 h, 2 nM) and irradiated (3 W, 3 min). The calculated absorbance of the cell monolayer, the estimated maximum temperature and the temperature at the edge of the area of dead cells during irradiation is also given. (These results correspond to those given in Figure 3.11 and the full table of results for all of the experiments is given in Appendix 3 – Table A3.2)

Outside of the area of dead cells reportedly killed by hyperthermia there is only a very narrow transition area, similar to that reported for CALNN gold NPs experiments, in which there are a few dead and alive cells. The fact that the photochemical method of killing cells reported for the 3 hour citrate NP experiments (3.3.3.1), does not start to dominate outside of the area of cells killed thermally, could be due to the high NP density loading of the intracellular vesicles of cells incubated for 24 hours, compared to those incubated for 3 hours (Chapter 2.3.1.2). It has already been shown that endosomes containing fewer NPs break up more easily during irradiation,[55] thus potentially causing more damage to the cell than an intact endosome containing NPs, and so it could be that the highly aggregated state of NPs in large endosomes are less efficient at the photochemical method than the less densely packed endosomes resulting from 3 hour incubations.

Finally, another important observation of the experiment using cells that had been incubated for 24 hours with citrate NPs is that during or immediately after irradiation a well-defined area of cells die (i.e. there is no delay before cell death). This is reported in Figure 3.12, the black dashed circle indicates the area of cells that die during or immediately after irradiation, with a diameter of 0.6 mm and the temperature of the cells at the edge of this area is *ca.* 70°C (see table 3.4). This is in excellent agreement with El-Sayed et. al.[46] who report that a threshold temperature of 70-80°C is required to kill cells immediately by hyperthermia, as discussed above.

	Centre (0.5 mm diam.)					
Figure 3.12	**Number of cells**	**Fraction of Cells Dead**	**Diam. of Area of Dead Cells**	**Calc. Abs (mOD)**	**Max T. (°C)**	**Temp. at the Edge of Area of Dead Cells (°C)**
A	222	100	0.60	14.4	96	71

Table 3.4: Cell viability determined immediately after irradiation (3 W 3 min) of HeLa cells incubated with citrate gold NPs (24 h, 2 nM). The estimated maximum temperature and the temperature of the cells at the edge of the well-defined area of dead cells are given.

3.3.4 Photodynamic Killing Using Gold Nanoparticles

The mechanism of cell death caused by irradiation of gold NP-loaded HeLa cells has been distinguished between photothermal, and photochemical effects (Sections 3.3.2 - 3.3.3).

Photothermal killing is achieved when cells are highly loaded with NPs and the incident irradiation is at a high enough power to induce a temperature of at least 50-55°C (under the conditions used here). There is a delay in cell death and preliminary results indicate that the length of this delay is dependent on the temperature reached during irradiation.

Photothermal killing using gold NPs is indeed a viable alternative to photodynamic therapy as discussed in Chapter 1; however, in Chapter 3 an alternative, non-thermal route for therapy is reported, similar to traditional PDT. Based on recent literature, the

photodynamic (photochemical) method of killing the cells under conditions when there is a not a high enough temperature rise to induce hyperthermia operates via singlet oxygen, $^1O_2$,[57, 58, 61] analogous to traditional PDT. This means that traditional PDT agents could be replaced with gold NPs with benefits such as; not suffering from photobleaching, high molar absorption coefficients and the ability for bioconjugation allowing for site specific targeting. Also using different shaped NPs such as nanorods allows for absorbance of light in the NIR region of the spectrum which has a greater penetration depth.

The advantages of using gold NPs in PDT rather than using photothermal therapy are that fewer NPs per cell are needed, and so potential therapeutic applications would be cheaper. Furthermore, lower irradiation doses can be used since the effect of $^1O_2$ is cumulative, whereas the maximum temperature that can be reached is given by intensity (see 3.3.1). Chapter 4 discusses in detail the production of $^1O_2$ by irradiation of gold NPs.

Chapter 4

Singlet Oxygen Generation by Laser Irradiation of Gold Nanoparticles

Irradiation of gold NPs with continuous wave (cw) lamp or laser light has been shown to lead to photogeneration of singlet oxygen ($^1O_2$) in vitro,[58-61] suggesting that this highly reactive species, which is widely used in photodynamic therapy,[3] may be involved in the photochemical pathway of cell killing by gold NPs. More recently, *in vitro* $^1O_2$ photogeneration by irradiation of spherical gold NPs with short laser pulses has also been reported,[57] using direct detection via the characteristic singlet oxygen luminescence at 1270 nm and indirect detection via the bleaching of 1,3-Diphenylisobenzofuran (DPBF), which is widely used for singlet oxygen detection.[61, 72-75] It was suggested that the mechanism of singlet oxygen photogeneration involves "hot" electrons, i.e. the highly excited conduction band electrons which upon absorption of a short laser pulse by a NP can reach quasi-equilibrated energy distributions corresponding to temperatures of several thousand degrees.[40, 76] In the same study, photobleaching of DPBF was also reported when spherical NPs were irradiated with cw-laser light at powers comparable to the pulsed laser light, with only a minor reduction in efficiency, and it was suggested that this also indicates photogeneration of $^1O_2$.[57] This seems somewhat surprising, since cw light at the intensities used in this study does not yield "hot" electrons due to the rapid electronic relaxation occurring in gold NPs.[12, 40, 76] Here, a more detailed investigation is presented, in particular of the cw-irradiation effects and the effect gold nanoparticles of size, shape and ligand shell.

4.1 Experimental

4.1.1 Gold Nanoparticle Preparation

15 nm- citrate and PEG- gold NPs, and 45 nm citrate gold NPs are used in this study, the syntheses and characterisation of these NPs is shown in Chapter 2.1.1.1.

4.1.1.1 Au Nanorods – *Prepared by D. Salah, Faculty of Science, Ain Shams University*

Gold nanorods were synthesised using the seeded-growth method reported by Dickerson *et al.* [77] with slight modifications. The seed solution was prepared by adding 60 μL of ice-cold 100 mM $NaBH_4$ to 7.5 mL of an aqueous solution containing 0.33 mM $HAuCl_4$ and 133 mM CTAB at 27°C.The growth solution was prepared by mixing 10 mL of 1 mM $HAuCl_4$, 10 mL of 200 mM CTAB, 500 μL of 4 mM $AgNO_3$ and 140 μL of 78.8 mM ascorbic acid and kept at 27°C. After ageing for two hours, 16 μL of the seed solution was added to the growth solution and stirred for 2 hours. The resulting NR solution was centrifuged twice (14500 rpm, 20 min), discarding the supernatant and resuspending the NRs after each run to remove excess CTAB. The UV-vis absorbance spectrum (Figure 4.1) showed a transversal Plasmon resonance band at 522 nm and a longitudinal Plasmon resonance band at 798 nm and transmission electron microscopy (obtained on a FEI Tecnai Spirit microscope) revealed them to have a length of 40 nm and a diameter of 12 nm. 476 μL of 0.01 mM mPEG5000 in H_2O (100,000 Peg/NR) was then added to the NR mixture and left overnight. The NR were then centrifuged four times (14500 rpm, 20 mins.), discarding the supernatant and resuspending in H_2O after each cycle. Finally, 3000 molecules (143 μL, 1 mM) of CALNN-TAT per NR was added and left overnight, the resulting ratio of mPEG5000 to CALNNTAT per NR was 2000:500 as determined by IR spectroscopy.

(TAT is an amino acid sequence and is appended to CALNN, this ligand was chosen for cell uptake purposes in D. Salah work, for the experiments reported here it is important to note that the NRs have a dense ligand shell).

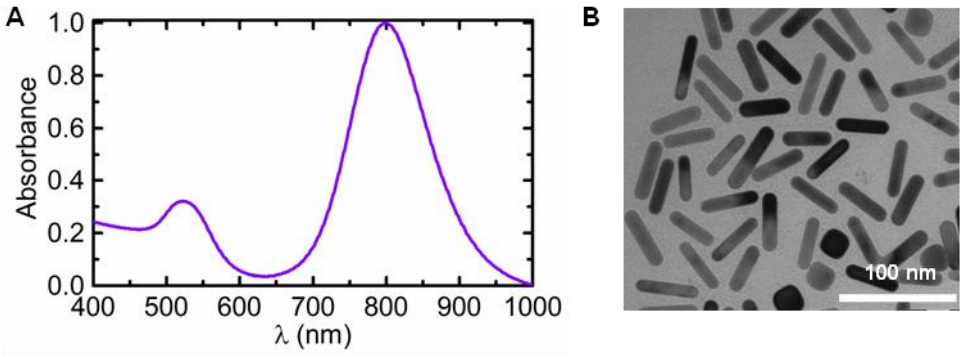

Figure 4.1: Characterisation of gold NR A) Uv-vis showing the transverse absorbance at 522 nm and the longitudinal absorbance at 798 nm and B) TEM micrographs showing the NR with a length 40 nm and diameter 12 nm

4.2.2. Singlet Oxygen Detection

All of the experiments involving DPBF were carried out in the dark.

4.2.2.1 Sample Preparation

Because DPBF is not soluble in neat water,[72] all experiments were conducted in 1/1 (v/v) mixtures of water and ethanol. A fresh solution of 3.1 mg DPBF in 100 mL EtOH (0.115 mM, A_{412nm} = 2) was kept stirring gently in the dark. A 10 mm quartz cuvette and a 3 mm stirrer bar were left in aqua regia (1:3 HNO_3:HCl) for 15 min. and thoroughly rinsed multiple times with MQ H_2O and EtOH. In the clean cuvette with stirrer bar, 600 µL MQ H_2O (with or without NPs or NRs, depending on the experiment) were mixed with 600 µL of the dye solution in EtOH. Prior to mixing, the NP concentration was adjusted to yield an absorbance of 0.4 at 532 nm in the final solution. The cuvette was sealed with a lid and parafilm and the UV-Vis absorbance spectrum measured (Genesys

10 UV). The sample was then placed on a stirring plate (in the dark) and its absorbance spectrum measured every 10 mins for 30 min to ensure the solution was stable.

4.2.2.2. Irradiation Set-Up

For the irradiation experiments, the cuvette containing 1200 µL sample solution was placed on a stirring plate in front of the laser. For experiments with NPs/NRs, the cuvette was fitted with heat fins using non-silicone heat transfer paste and cooled using a fan. No significant increase of the cell temperature beyond a slight warming was observed. For most experiments, the sample was irradiated at 1000 mW (unless stated otherwise) using a 532 nm continuous-wave diode pumped solid state laser (Laser Quantum Opus 532) with a $1/e^2$ beam diameter of 1.85 mm; for some experiments the beam was expanded to 8 mm diameter, as stated explicitly in the results section). The sample was irradiated for 10 min, then removed from the laser set-up to record the absorbance spectrum (Genesys 10 UV); this was repeated until the sample had been irradiated for 60 min in total.

Irradiation of gold NRs in the longitudinal Plasmon resonance band at 800 nm was done with the same setup, but using a Titanium:Sapphire laser (Coherent Mira 900), aligned on the auxiliary cavity, which prevents mode-locking and thus provides continuous-wave laser operation at 800 nm with 1000 mW power; the beam was expanded to 3.4 mm using two lenses.

Pulsed laser irradiation was done with the same set-up, but using the second harmonic of a Q-switched Nd:YAG-laser (Quantel Brilliant) (532 nm, 5 ns pulse length, 10 Hz repetition rate, 3.5 mm beam size, 15 mJ pulse energy).

4.2.2.3. Analysis of Results

For experiments that included NPs the absorbance of DPBF at 412 nm had to be corrected by subtracting the absorbance of the NPs at 412 nm. The concentration of DPBF used always had an absorbance close to 1 at 412 nm and for data analysis this value was normalised to 1.

4.2 Results of DPBF Photobleaching in the Presence and Absence of Gold Nanoparticles

1,3-Diphenylisobenzofuran readily undergoes a 1,4-cycloaddition addition on reaction with $^1O_2$ to form endoperoxides which irreversibly yield 1,2-dibenzoylbenzene (Figure 4.1). DPBF strongly absorbs light at 412 nm (see Figure 4.3A), but due to the loss of the π-system of isobenzofuran the product does not absorb at this wavelength; it is this loss of absorbance at 412 nm that is used to detect the presence of singlet oxygen.[78]

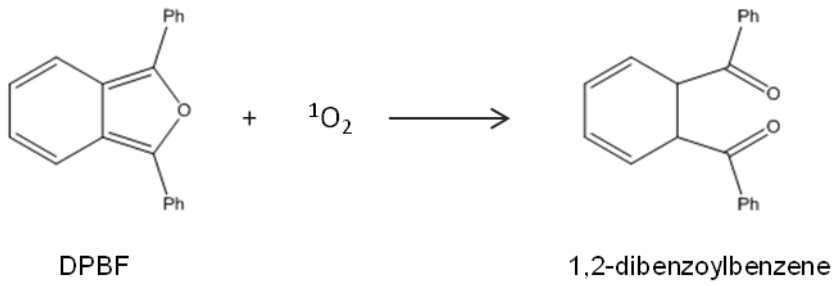

Figure 4.2: Reaction scheme of DPBF with $^1O_2$ forming 1,2,-dibenzoylbenzene

4.2.1. DPBF Photobleaching

Here, DPBF was chosen as singlet oxygen sensor as it has no absorbance at 532 nm, the wavelength used for laser irradiation of gold nanoparticles in their Plasmon resonance band, and no photobleaching of DPBF was expected to occur upon irradiation in the absence of NPs. Contrary to this expectation, some bleaching was observed under our

cw-irradiation conditions, with the DPBF absorbance decreasing by ~10% upon irradiation at 1 W for 60 minutes (Figure 4.3A).

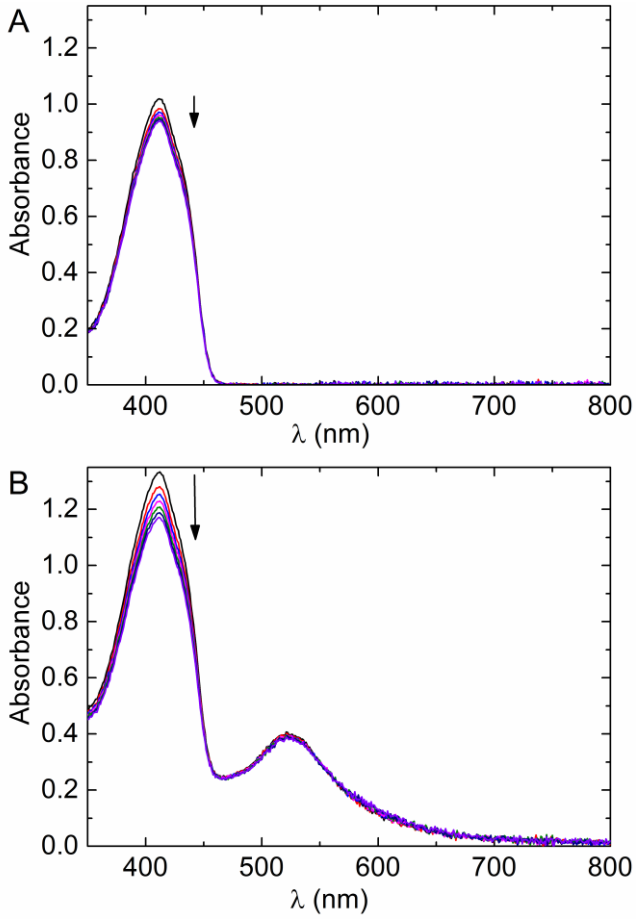

Figure 4.3: Photobleaching of the DPBF absorbance upon cw-irradiation at 532 nm, 1 W, in 50/50 ethanol/water solution. A) in the absence of NPs and B) in the presence of 13 nm gold NPs. Shown are absorbance spectra taken at intervals of 10 min from before the irradiation up to a maximum irradiation time of 60 min; the arrows indicate the direction of change.

The photobleaching of the DPBF in the absence of NPs was investigated further, it is important to note that in the absence of laser irradiation the DPBF remains stable (in the dark in 50/50 H_2O/EtOH) with no decrease in absorbance at 412 nm over time (Grey squares – Figure 4.4).

The photobleaching of DPBF with continuous irradiation at 532 nm has two phases; (i) a rapid phase, present in the first 20 min of irradiation, and (ii) a slower phase, that is linear on the time scale of this experiment.

Figure 4.4(A) shows time dependent photobleaching of DPBF at different irradiation powers, the rapid phase (present up to 20 min of irradiation) shows a power dependence, increasing the laser power increases the photobleaching. The slower phase (ii) is essentially independent of incident power unless low laser powers are used (30 mW – orange squares) which is much lower than powers used in this study.

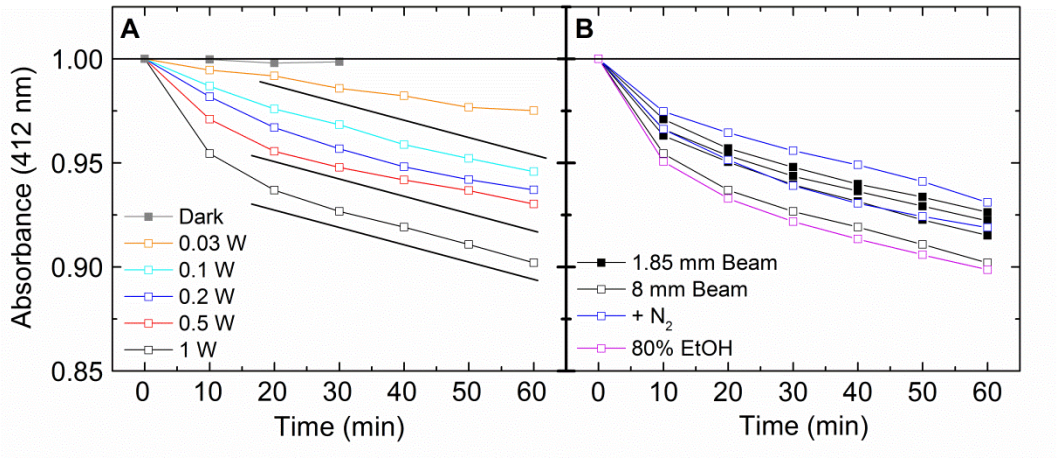

Figure 4.4: Time dependent photobleaching of DPBF absorbance at 412 nm (in the absence of gold NPs), cw-irradiation, 532 nm A) At different laser powers, and B) at 1 W, under different experimental conditions

The dependence of the photobleaching on other experimental parameters was investigated, Figure 4.4(B) shows that expanding the laser beam from 1.85 mm (filled black squares) to 8 mm (open squares) increases the photobleaching rate of the rapid phase but has no effect on the slower phase. Increasing the ethanol content from 50 – to 80% (purple squares) has a very small effect of the rapid phase but again it does not affect the slower phase. Finally, the rapid phase has oxygen dependence as bubbling the DPBF solution with nitrogen for ten mins prior to irradiation reduces the slope in the first 10 – 20 minutes (blue open squares) but this oxygen dependence is not seen from 20 to 60 mins.

In summary, the rapid phase (i) of the DPBF photobleaching depends on laser power, beam size and the presence of oxygen whereas the slower phase (ii) is independent of these parameters and essentially has a linear dependence on irradiation time.

The oxygen dependence of rapid phase (i) suggests autooxidation of DPBF which has been reported previously.[79] However, at the present moment, the mechanism of both bleaching phases remains to be solved. It should be noted that this effect has been reported previously, with cw-irradiation at 514 nm for 60 minutes at significantly lower powers than employed here (40 mW) leading to a ~5% decrease in DPBF absorbance, although no explanation was suggested in that report.[80]

4.2.2 Photogeneration of $^1O_2$ by Continuous Irradiation of Gold Nanoparticles

In presence of gold NPs, the photobleaching of DPBF is significantly increased (Figure 4.3). The time dependence of the DPBF photobleaching in the absence of NPs and in the presence of NPs with 15 and 46 nm diameter is shown in Figure 4.5(A)**.** Multiple results are shown for experiments in the presence of NPs to highlight the reproducibility of the experiment. It can be clearly seen that the presence of NPs leads to a significant increase of the DPBF photobleaching effect and that larger NPs yield a larger effect although the NP absorbance was adjusted to be the same for all samples, so that the same amount of light was absorbed.

The fact that significant DPBF photobleaching occurs even in the absence of NPs requires careful consideration for the analysis of these data. Like DPBF photobleaching in the absence of NPs, the effect in the presence of NPs shows two phases. However, subtraction of the effect observed when only the dye is present yields an essentially linear time dependence for the additional effect ascribed to the NPs on the time scale of the experiment, see Figure 4.5(B). Moreover, the second phase of DPBF photobleaching

is largely independent of the laser power, at least down to 0.1 W, i.e. significantly lower powers than those used for most of the experiments reported here (Figure 4.4), allowing a direct comparison of the results obtained in the time frame of 20 - 60 minutes. For this reason, only data starting at 20 minutes irradiation will be used for quantitative comparisons.

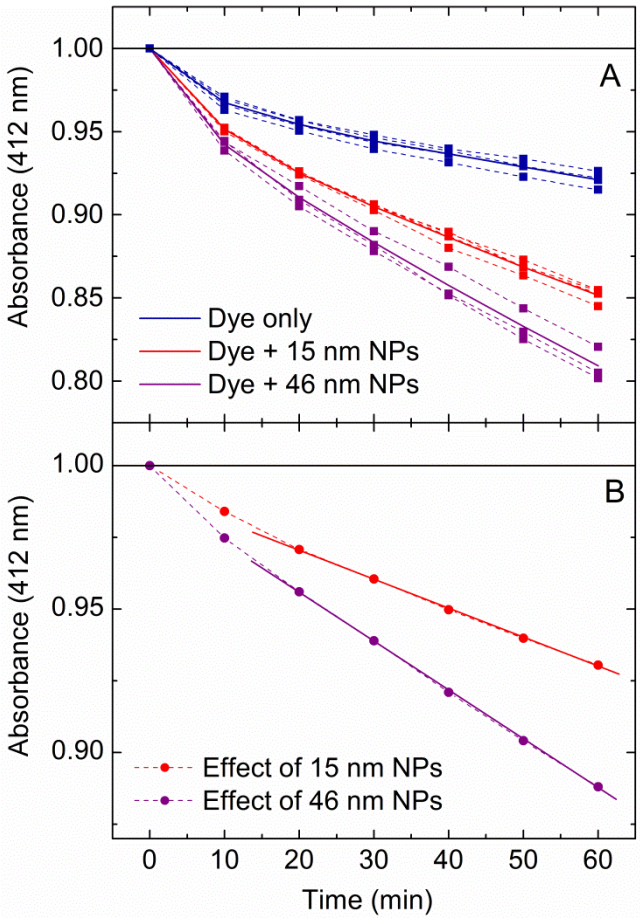

Figure 4.5: A) Time dependence of the photobleaching of the DPBF absorbance at 412 nm in the absence (blue square) and presence of NPs with 15 nm (red squares) and 46 nm (purple squares) diameter; shown here are the results from several individual experiments (dashed lines) and the average (solid lines), normalised to 1 at time zero – see section 4.2.3 for details of data treatment and analysis. B) Effect of the NPs alone, calculated by subtracting the photobleaching effect of DPBF in the absence of NPs from the results obtained in the presence of NPs.

Figure 4.6 summarises the main results obtained here. It is very obvious that gold NPs induce significantly faster DPBF photobleaching than is observed in their absence (blue); this is found for 15 nm gold nanoparticles (red), but is even more pronounced for

larger NPs with 45 nm diameter (purple). It is interesting to note that, unlike the direct DPBF photobleaching, which is not affected by nitrogen purging, the NP-induced additional bleaching is significantly reduced by N_2 purging, almost down to the level of the direct DPBF photobleaching effect. This strongly supports the conclusion that the NP-induced effect is caused by the formation of $^1O_2$ which then leads to DPBF photobleaching.

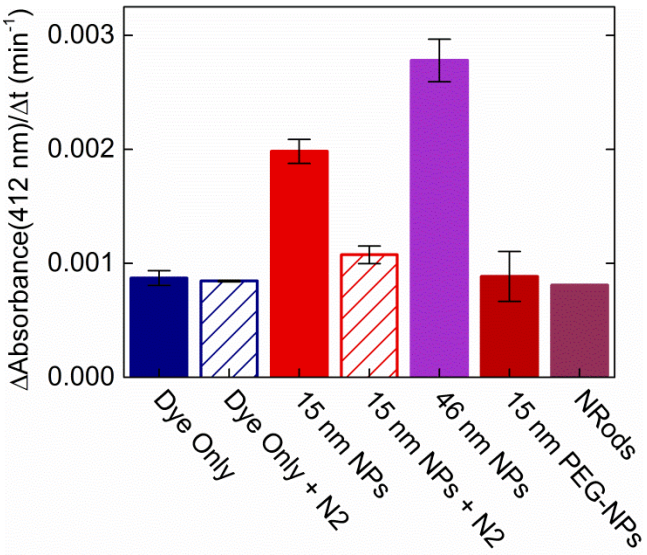

Figure 4.6: The gradient of the time-dependent DPBF photobleaching in the irradiation time window of 20-60 min for different samples under cw-irradiation at 532 nm, 1 W. Where appropriate, the NP/NR concentration was adjusted to yield an absorbance of 0.4 at 532 nm. The error bars correspond to the standard deviation of several repeat experiments; no repeat experiment was undertaken for irradiation of NRs at 532 nm, but the same result (no additional bleaching in presence of NRs) was obtained for irradiation at 800 nm, Figure 4.6. Experiments for DPBF in the absence of NPs and in the presence of 15 nm NPs were also undertaken after bubbling the sample with nitrogen for 10 min, as indicated.

Increasing the size of the NPs from 15 to 46 nm increases the NP-induced DPBF photobleaching (i.e. the additional effect, after subtracting the direct DPBF photobleaching gradient) by *ca.* 42%, indicating more $^1O_2$ formation. On the other hand, capping the 15 nm gold NPs with PEG-OH, a moderately large ligand (Chapter 2.1.1.2)

essentially removes the NP-induced bleaching and reduces the observed effect to the level of the direct DPBF photobleaching.

Gold nanorods (NRs), which have two Plasmon resonance bands, namely the transversal band at 522 nm and the longitudinal one at 798 nm (Figure 4.1), stabilized with mPEG5000 and CALNNTAT were also investigated. Irradiation of the transversal Plasmon band at 532 nm showed no additional DPBF bleaching above the direct DPBF bleaching (Figure 4.6). Irradiation at 800 nm (1 W) showed reduced direct DPBF photobleaching, compared to irradiation at 532 nm, but again no additional photobleaching was observed in the presence of NRs (Figure 4.7).

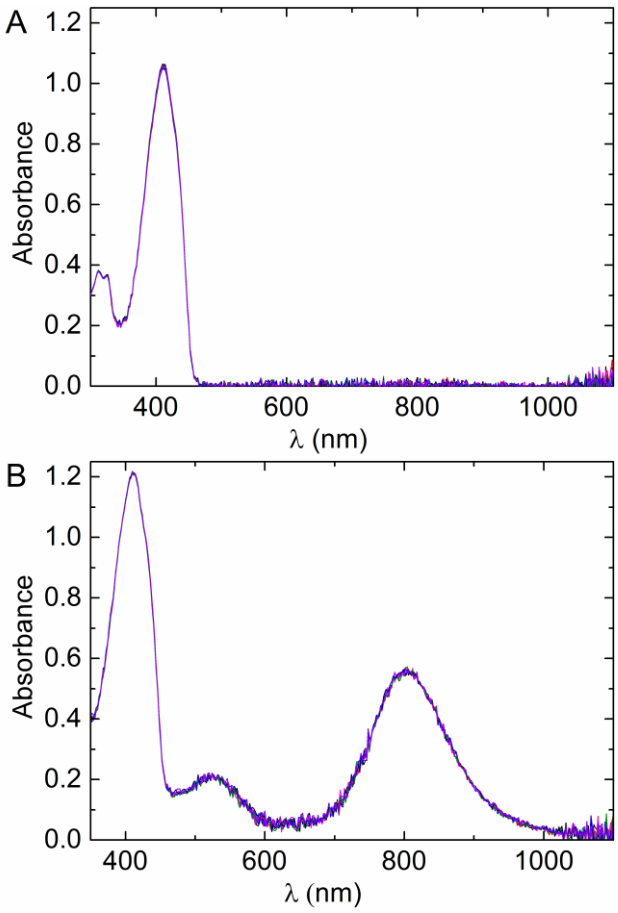

Figure 4.7: Photobleaching of the DPBF absorbance upon cw-irradiation at 800 nm, 1 W, A) in the absence of NPs and B) in the presence of gold NRs. Shown are the absorbance spectra taken at intervals of 10 min up to a maximum irradiation time of 60 min

4.2.3. Photogeneration of $^1O_2$ by Gold Nanoparticles by Pulsed Irradiation

Irradiation at 532 nm in the presence and absence of 15 nm gold NPs was also investigated using laser pulses with a pulse duration of 5 ns (Figure 4.8). In this case, the UV-vis spectra show a slight broadening of the NP Plasmon resonance band at 520 nm during the first five minutes of irradiation, suggesting that some aggregation occurs; after the initial five minutes, however, the NPs remain stable. Analysis of the spectra (Figure 4.8(B)) shows that photobleaching of DPBF in the absence of gold NPs is very similar to the results obtained using cw laser irradiation at comparable average powers (Figure 4.4(A)). In the presence of 15 nm gold NPs, on the other hand, the bleaching effect which is induced by pulsed laser irradiation is significantly larger than that caused by cw-irradiation, in spite of the significantly lower laser power employed during the pulsed irradiation experiments (0.15 W vs. 1 W).

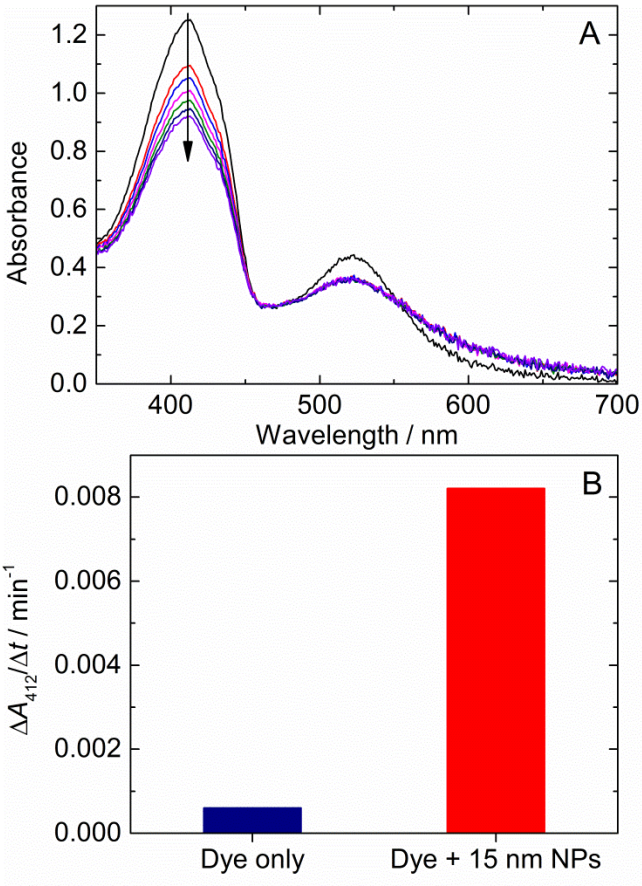

Figure 4.8: Photobleaching of the DPBF absorbance upon laser irradiation with 5 ns laser pulses at 532 nm, 0.15 W, in the presence of 15 nm gold NPs. A) Absorbance spectra taken at intervals of 5 minutes up to a maximum irradiation time of 30 minutes; the arrow indicates the direction of change. B) Gradient of the time-dependent DPBF photobleaching (measured at 412 nm) in the irradiation time window of 20 - 30 minutes in the absence and presence of NPs.

4.2.4. Quantum Yield of $^1O_2$ Photogeneration

It is straightforward to estimate the quantum yield of NP-induced DPBF photobleaching from the absorbed laser power and the observed rate of absorbance bleach. Under cw-irradiation at 532 nm, this yields values of 5 10^{-7} and 8 10^{-7} for 15 and 46 nm NPs, respectively. Thus, less than one of each one million photons absorbed by a NP leads to the photobleaching of a DPBF molecule under cw-irradiation. For irradiation of 15 nm NPs with 5 ns-laser pulses, on the other hand, the quantum yield of NP-induced DPBF

photobleaching is 3.5 10^{-5}, i.e. almost two orders of magnitude larger than for cw-irradiation, but still very small.

Diffusion of oxygen over the lifetime of $^1O_2$ (approx. 6 μs in 50/50 water/ethanol[72]) covers a distance larger than the average distance between DPBF molecules at the concentrations used here, and hence it can be concluded that a significant fraction of photogenerated $^1O_2$ should be detected. This is confirmed by literature reports showing that a DPBF concentration of ~10^{-4} M, which is close to the concentration used here, is sufficient to detect 50% of photogenerated $^1O_2$.[72] Thus, the observed low quantum yield of DPBF photobleaching indicates a very low quantum yield of $^1O_2$ photogeneration by gold NPs, having values of the order of ~10^{-6} for cw-irradiation and ~10^{-4} for irradiation with ns laser pulses.

4.3. Discussion

The results show that irradiation of citrate stabilised spherical gold NPs at 532 nm, *i.e.* in their surface Plasmon band, with pulsed *or* cw laser light leads to the production of $^1O_2$, detected here by monitoring the bleaching of DPBF absorbance. However, the rate of $^1O_2$ production is much larger when using short laser pulses than when using cw light of comparable intensity. Whereas *ca.* 24% of the dye is bleached after only 10 minutes of irradiation of 15 nm NPs with 5 ns laser pulses at an average power of 150 mW (Figure 4.8), only 1-2% of the dye is bleached over this time by irradiation of the same NPs with cw light at significantly higher power (1 W) (Figure 4.3). These differences allow important conclusions on the mechanism of $^1O_2$ production by irradiation of gold nanoparticles.

4.3.1 Pulsed Irradiation

4.3.1.1 Heating of Nanoparticles

Irradiation of spherical gold NPs at 532 nm leads to the excitation of their Plasmon resonance, which can be described as a coherent oscillatory motion of the conduction band electrons; this oscillation dephases and decays on the sub-100 fs timescale, with only a very small radiative contribution, so that most of the excitation energy is retained as electronic excitation in the form of electron-hole pairs. Since the photon energy is close to the minimum energy required for direct excitation of d-band electrons into the conduction band of gold, a minor contribution of this excitation mechanism cannot be ruled out; however, d-band holes are filled by conduction band electrons on the 10-fs time scale, yielding essentially the same outcome as excitation of the Plasmon resonance band.[40] The excited electrons initially have a non-thermal energy distribution, and often are referred to as "primary hot electrons", although the concept of temperature does not strictly apply to such a distribution. They rapidly (within less than 500 fs) equilibrate by electron-electron scattering to yield a Fermi distribution corresponding to an elevated temperature, and can then be referred to as "hot electrons".[12, 40, 76] Hot electrons have been shown to cause gold-thiol bond dissociation at the surface of gold NPs [46] and have been suggested to be responsible for the creation of $^1O_2$ by irradiation of gold NPs with nanosecond laser pulses.[57] They lose their energy on the time scale of a few picoseconds by interaction with the lattice (electron-phonon scattering) with coupling times that are essentially size-independent for NPs above 10 nm in diameter, although they strongly depend on the amount of energy deposited due to the temperature-dependent electronic heat capacity.[40, 76] Because the lattice heat capacity is much larger than the electronic heat capacity, this leaves the electrons and the lattice in equilibrium at a temperature which is significantly lower than the initial electronic temperature; finally, cooling occurs by heat transfer to the solvent and heat diffusion on the time scale of 10 to a few 100 picoseconds, strongly depending on NP size.[56]

Since the dissipation of the absorbed energy proceeds on the picosecond time scale, excitation with a nanosecond laser pulse yields a highly non-equilibrium situation during the duration of the laser pulse where energy is continuously deposited into the electronic system and at the same time flows through the lattice into the surrounding solvent. It is, therefore, not straightforward to predict the temperature of the hot electrons achieved in such experiments. The simulations to estimate this temperature were performed by M. Volk using the standard "two-temperature model" for the electron and phonon heat baths,[14, 40, 76, 81] coupled to finite-element heat transfer and diffusion simulations in the surrounding solvent, details are given in Appendix 4.1 As shown in Figure 4.8, under the conditions used here, the electrons are expected to reach a temperature of 2100 °C, although the lattice only reaches temperatures of the order of 1400 °C and the solvent in the immediate vicinity of the NP a temperature of about 900 °C.

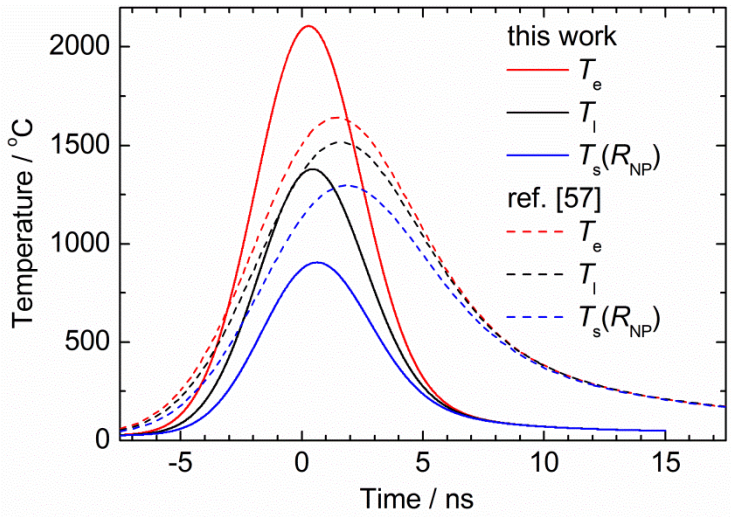

Figure 4.9: Time-dependent temperatures of the conduction band electrons (red), lattice (black) and first solvent layer (blue), calculated for our experiments using ns-laser pulse excitation (15 nm spherical NPs in 50/50 EtOH/water, 5 ns laser pulses with 0.15 J cm^{-2} intensity, solid lines), and for the experiments described in ref. [57] (40 nm spherical NPs in 80/20 EtOH/water, 7 ns laser pulses with 0.03 J cm^{-2} intensity, dashed lines) using the "two-temperature model" for the electron and phonon heat baths, coupled to finite-element heat transfer and diffusion simulations in the surrounding solvent, see Supporting Information for details; time-zero corresponds to the center of the laser pulse.

A lattice temperature of 1400 ^{o}C, which is above the melting temperature for solid gold, albeit present for only a few nanoseconds, might be sufficient to cause temporary melting of the nanoparticle,[40] although the pulse intensities used here are still below the reported threshold for size reduction of gold NPs of 15 nm diameter by nanosecond laser pulses.[82] Nevertheless, a minor effect on the shape and/or size of the NPs, especially at the upper end of the size distribution, cannot be ruled out, and may be related to the minor NP spectral changes observed upon irradiation which suggest some aggregation to occur, see above. Due to the slower heat dissipation around larger NPs, these are heated to higher temperatures and hence are more likely to fragment, in agreement with experimental results on ns-laser pulse induced fragmentation, which also show that fragmentation is finished after five minutes under conditions similar to the ones used here.[82] Since our NPs were prepared without excess citrate, the resulting increase in the ratio of surface area to volume may indeed cause some aggregation. It also cannot be ruled out that the solvent near the NP surface temporarily forms bubbles,[83] although the pulse intensities used here are still below the reported threshold for bubble formation by nanosecond pulses for 15 nm NPs.[84] Such bubbles could lead to better thermal insulation, thus potentially increasing the maximum temperatures, but on the other hand they might prevent oxygen from reaching the NP surface, thus reducing the chance of $^{1}O_2$ formation.

4.3.1.2 $^{1}O_2$ photogeneration by Equilibrated Hot Electrons

The formation of $^{1}O_2$ from the triplet ground state by interaction with a photoexcited sensitizer requires a change of the electron spin and hence cannot result from dipole-dipole (Förster) interaction, but only from Dexter-type electron exchange coupling; the latter can be described as simultaneous transfers of an electron from one of the $2\pi^*$ molecular orbitals on oxygen to a photogenerated hole on the sensitizer and of an electron with opposite spin from a high-energy excited sensitizer level to the same or the

other $2\pi^*$ orbital, resulting in the formation of the $^1\Sigma$ or $^1\Delta$ singlet oxygen state, respectively.[85] This mechanism requires significant overlap of the relevant electronic wavefunctions and hence only occurs at short distances of at most 10 Å. Since the photoexcited hot electrons have such a short lifetime, this reaction therefore can only occur if an oxygen molecule happens to be in the vicinity of the NP or is temporarily adsorbed to its surface at the moment of excitation. A similar reaction occurs on photoexcited Si nanocrystals, [80, 85] although in this case the reaction is more efficient than for Au NPs due to the much longer lifetime of the photoexcited excitons in Si. Thus, the short lifetime of hot electron excitation in gold nanoparticles easily explains the low quantum yield of $^1O_2$ photogeneration which is observed here.

The excitation of electrons to temperatures exceeding 2000 ^oC means that a significant number have sufficient energy to excite an oxygen molecule to the $^1\Delta$ state, which has an energy of 0.98 eV above the $^3\Sigma$ state,[3] see Figure 4.9. The absolute number of hot electrons available at the higher energy – and the number of holes available at the lower energy involved in this two-electron exchange reaction – can be estimated from the density of states of gold and the Fermi distribution, as described in more detail in Appendix 4. For example, for a spherical NP with 15 nm diameter at an electron temperature of 2100 ^oC, there are 260 electrons within an energy interval of 0.1 eV around the $^1\Delta$ state (it should be noted that the relevant energy interval is the width of this state for an oxygen in the vicinity or temporarily adsorbed onto a NP, which is not known). Thus, the electron temperatures achieved in our experiment are sufficient for a significant population of hot electrons and holes at the relevant levels.

The large number of equilibrated hot electrons available during a ns-laser pulse also rules out the primary hot electrons as the main source of $^1O_2$ photogeneration. The number of primary hot electrons available during the pulse duration can be estimated from the number of photons which are absorbed per nanosecond, multiplied by their

lifetime, which is less than 500 fs.[76] However, these primary hot electrons populate NP states at energies from the Fermi level E_F to E_F + 2.34 eV (the energy of a photon at 532 nm), see Figure 4.8(C). For 15 nm NPs and excitation with 5 ns laser pulses with 0.15 J cm^{-2} intensity, this predicts that not more than three primary hot electrons are available within an energy interval of 0.1 eV around the $^1\Delta$ level at any time during the laser pulse, assuming that all levels are equally populated and taking into account that the density of states for gold has an essentially constant value in the relevant energy range around E_F.[86] This is significantly less than the number of hot (equilibrated) electrons available at the maximum electron temperature, which was estimated to be on the order of 260 for the same energy interval, see above. Thus, we can conclude that it is indeed the hot electrons which are responsible for the observed $^1O_2$ photogeneration when using short laser pulses for excitation.

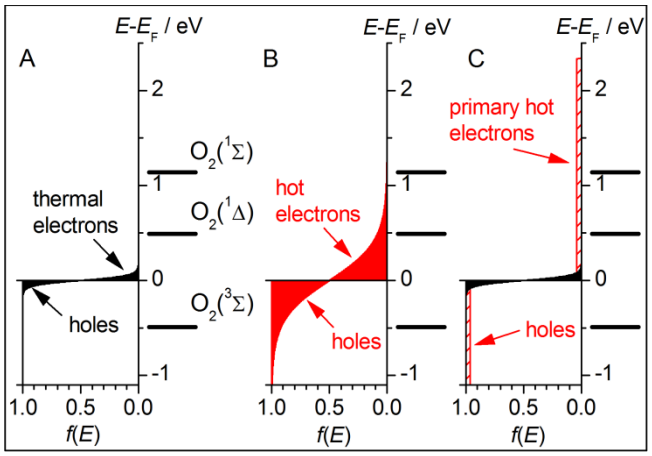

Figure 4.10: Schematic diagram showing the population probability $f(E)$ for NP states near the Fermi level, E_F, under different conditions: (A) in equilibrium at room temperature, (B) at an electron temperature of T_e = 2100 ^{0}C after electron-electron equilibration ("hot electrons"), and (C) immediately after the absorption of photons by single electrons ("primary hot electrons", with population changes highly exaggerated to make them visible). Also shown are the energies of the ground-state triplet ($^3\Sigma$) and lowest-excited singlet state ($^1\Delta$) of oxygen, as well as the next singlet state ($^1\Sigma$) under the assumption that E_F is equidistant from the $^3\Sigma$ and $^1\Delta$ energies. Excitation of an oxygen molecule to $^1O_2$ requires the simultaneous transfer of an electron from the oxygen to a hole at the energy of the $^3\Sigma$ state and of a hot electron with the opposite spin and an energy at the $^1\Delta$ (or $^1\Sigma$) level to the oxygen molecule.

Similar results to those obtained here using pulsed irradiation have recently been reported for spherical gold NPs with 40 nm diameter.[57] Although a significantly lower laser pulse energy density (0.03 J cm^{-2}, compared to 0.15 J cm^{-2} here) was used under otherwise similar experimental conditions, slightly faster $^1O_2$ photogeneration was observed in this study, with the DPBF absorbance decreasing by ~40% over 10 minutes of irradiation, compared to the ~20% decrease observed here in the first 10 minutes, Figure 4.7(A). In this context, it is interesting to note that in spite of the lower laser pulse energy density the NPs are heated to almost the same electron temperature as in our experiments, see Figure 5. This is largely due to (i) heat dissipation from larger NPs being slower[56] and (ii) the use of 80/20 EtOH/water as solvent in ref. [57], which has slower heat transport than a 50/50 EtOH/water mixture. An explicit calculation of the number of hot electrons available at the energy of the oxygen $^1\Delta$ state for the two experiments is given in Appendix 4; together with a detailed consideration of all other experimental differences, this yields very good agreement between the expected and the observed relative $^1O_2$ photogeneration rates, see the Supporting Information for details. This provides further support for the conclusion that $^1O_2$ photogeneration is mediated by the equilibrated hot electrons of gold nanoparticles under ns-pulsed laser irradiation.

4.3.2 Continuous Irradiation - $^1O_2$ photogeneration by Primary Hot Electrons

Compared to the effect of pulsed irradiation, the rate of $^1O_2$ photogeneration is much smaller when using cw light of comparable intensity. Whereas ca. 24% of the dye is bleached after only 10 minutes of irradiation of spherical NPs with 15 nm diameter with 5 ns laser pulses at an average power of 150 mW (Figure 4.8), only 1-2% of the dye is bleached over this time by irradiation of the same NPs with cw light at significantly higher power (1 W) (Figure 4.5). In a previous publication,[57] significantly higher rates of

DPBF photobleaching had been reported under conditions which appear to be similar to the ones used here. Such significantly higher rates of bleaching have been observed, but only when the protocol described in Section 4.2.2 was not followed accurately; for example, the use of dye solution that had not been freshly prepared or of a cuvette that had not been cleaned thoroughly and rinsed multiple times with MQ water, or the use of a cell that was not sealed during the irradiation, leading to some loss of ethanol from the solution, all resulted in larger and highly irreproducible bleaching of DPBF under cw-irradiation.

In the following, we will show that photogeneration of $^1O_2$ under cw-irradiation, unlike pulsed irradiation, is mediated by the initially created "primary hot" electrons, i.e. it occurs during the short time during which the excited electrons have not yet relaxed to a thermal distribution, see Figure 4.10(C).

Under the cw-irradiation conditions used here (1 W, 1.85 mm beam diameter), a spherical NP with 15 nm diameter absorbs photons at an average rate of $1.3\ 10^8\ s^{-1}$, as estimated from the absorption cross section[70] and the beam intensity. This means that after absorption of a photon there is enough time for full relaxation and transfer of the photon energy into the solvent, which occurs in less than 100 ps,[56] before absorption of the next photon. Absorption of one photon by a 15 nm NP yields "hot" electrons at a temperature of 10 K above the surrounding after electron-electron equilibration; these "hot" electrons lose their energy by electron-phonon scattering within a few picoseconds to yield a NP whose temperature is only 80 mK above the surrounding. Neither of these effects are expected to yield any significant photochemical effects; estimates analogous to those described above predict that for a spherical 15 nm NP with an electron temperature of 305 ^oC there are $\sim 2.6\ 10^{-5}$ electrons within an energy interval of 0.1 eV around the oxygen $^1\Delta$ state, and the same number of holes around the $^3\Sigma$ state energy. This means that there are on the order of 10^7 times less hot electrons and 10^7 times less

holes available for the photoreaction, which rules out any significant reaction; this is also confirmed by the fact that these population numbers are less than a factor 2 larger than those for room temperature, where no $^1O_2$ is generated in the absence of light.

This leaves only the primary hot electrons, i.e. those electrons which are excited upon absorption of a photon but have not yet equilibrated by electron-electron scattering, as potential cause for photogeneration of $^1O_2$. Absorption of a single photon can potentially excite electrons to energies of up to 2.34 eV above the Fermi level. If one assumes excitation of only one electron by each photon and equal excitation probability for all available electrons, as shown in Figure 4.10(C), on average there will be 0.043 electrons within an energy interval of 0.1 eV around the oxygen $^1\Delta$ state, which is approx. 5000 times less than during a single laser pulse in the pulsed experiments, see above. Taking into account that the same factor also applies to the holes required for the Dexter mechanism, but correcting for the lifetime of the excitation (~500 fs for primary hot electrons created during cw-irradiation[12, 40, 76], ~3 ns for the hot electron distribution induced by a single laser pulse, see Appendix 4 - Figure A4.1) and the repetition rates ($1.3\ 10^8\ s^{-1}$ for single photon absorption during cw-irradiation, $10\ s^{-1}$ for the pulsed laser irradiation), one would predict a rate of $^1O_2$ photogeneration under our cw-irradiation conditions which is smaller than that expected for our pulsed irradiation conditions by a factor of ~ 10^4. This is significantly closer to the experimental results (ratio of $^1O_2$ photogeneration rates under pulsed vs. cw-irradiation of 10 - 20) than any estimate based on the equilibrated "hot" electrons after the absorption of a single photon. The main discrepancy between the predicted and observed cw-results arises from the assumption of direct excitation of single electrons in the above estimate, which is not valid for irradiation at 532 nm, i.e. in the gold NP Plasmon resonance band, since this leads to the coherent excitation of many electrons which rapidly dephases without the electrons exchanging energy. Thus, absorption of a single photon yields more than one primary

hot electron, with the photon's energy distributed over all of them. Consequently, the energy distribution even of the primary hot electrons will not extend up to 2.34 eV above E_F, but will be shifted towards the states nearer the Fermi level, thus increasing the population of states around the oxygen $^1\Delta$ energy and hence the yield of $^1O_2$.

In conclusion, cw-irradiation is less efficient than pulsed laser irradiation in photogenerating $^1O_2$ since the (equilibrated) hot electrons, which are the main mediator of the photochemistry in the case of pulsed irradiation, do not have sufficient energy/temperature to drive $^1O_2$ photogeneration. Nevertheless, our results confirm that cw-irradiation of spherical gold NPs produces detectable amounts of $^1O_2$.[57, 58] The absence of significant amounts of (equilibrated) hot electrons means that $^1O_2$ photogeneration proceeds via a different mechanism under cw-irradiation compared to pulsed laser generation; the above estimates indicate that it is the primary hot electrons, i.e. the directly photoexcited electrons, which are responsible for the photochemistry here, and that the photochemical reaction must occur before these equilibrate by electron-electron thermalisation.

Chapter 5

Conclusions and Future Work

Continuous irradiation of HeLa cells loaded with gold NPs results in cell death, experimental results in this thesis have distinguished between situations when photothermal effects dominate and those when only photodynamic effects are responsible.

It was shown that the incubation of HeLa cells with citrate gold NPs resulted in cell uptake via endocytosis with the NPs remaining in vesicles once internalised. Capping the NPs with the pentapeptide CALNN and using higher NP concentrations resulted in 5 times higher NP uptake by the cells, with a significant proportion of the NPs remaining on the cell surface. Irradiation of these cells resulted in phenomenological differences in the distribution of the dead cells 24 hours later.

Those experiments with citrate gold NPs resulted in cell death with some degree of variation, even when the irradiated areas of cells were on the same dish, viable cells were seen amongst the cells killed by irradiation and the confluency of the cells had no effect on the outcome of the experiment. CALNN gold NP experiments, on the other hand, resulted in a well-defined area of only dead cells if the confluency of the exposed area was high enough. Numerical simulations used to estimate the temperature of the cells during irradiation revealed that the cells irradiated in the presence of citrate NPs experienced a temperature increase of only a few degrees, not high enough to kill the cells thermally. In the case of the CALNN gold NP experiments, the temperature of the cells during irradiation for the experiments that resulted in dead cells was high enough to kill the cells thermally, and for those that did not result in cell death the temperature estimated was not high enough to kill the cells thermally. The conclusion drawn was that

the mechanism killing the cells in the citrate NP experiments is photochemical and for the CALNN gold NP experiments a photothermal route dominates cell death induction.

In vitro experiments to further investigate the non-thermal photodynamic effect show that continuous irradiation of gold nanoparticles yields $^1O_2$,

This raised the question, why cells in the CALNN gold NP experiments that do not reach temperatures high enough to induce hyperthermia during irradiation do not die due to the photodynamic method. Further investigation into $^1O_2$ generation by irradiation of gold NPs *in vitro* revealed that the yield of $^1O_2$ was much lower than that previously reported[57] and that a moderately thick, but dense capping layer could reduce the efficiency of the $^1O_2$ production, which is the reason that the irradiation of the cells loaded with CALNN gold NPs did not kill the cells via a photodynamic mechanism. The yield of singlet oxygen could be increased by using larger NPs.

The use of gold NPs as PDT agents is promising; the design implications that should be considered from results concluded in this work are NP size and capping layer. A future consideration would be the localisation of the NPs in the cell, as the lifetime of $^1O_2$ is short; it reacts with the cell contents in its immediate vicinity. If the NPs were, for example, in the nucleus, then $^1O_2$ may be more detrimental to the cell. It has been demonstrated NPs are delivered to the nucleus when conjugated to cell penetrating peptides which include a nuclear localisation signal peptide.[69, 87]

Experiments to further investigate the differences between photothermal and photodynamic effects would include determining whether the laser induced cell death was apoptotic or necrotic, this could be done by live cell imaging using annexin V and propidium iodide (PI). PI does not stain live or early apoptotic cells due to the presence of an intact plasma membrane, whereas annexin V detects cells that have expressed phosphatidylserine (PS) on the cell surface, an event found in apoptosis. It would be

interesting to see if photodynamic and photothermal effects cause different modes of cell death. This method would also be interesting for the investigation into the cell death delay observed in Chapter 3 (3.2.2.1 & 3.2.3.1). For the photothermal cell death delay it was suggested that there is a possibility that the delay time is dependent on the temperature the cells are heated to during irradiation, however this was based only on a few experiments and further work would help to confirm this. Preliminary work using this method was done, but unfortunately due to time constraints the protocol could not be fully developed to obtain useful results.

Another technique that was attempted was serial block face scanning electron microscopy (SBF-SEM). The aim of this technique is to obtain high resolution 3D images of the cell; for this method, the cells are processed into resin (similar to the procedure described in chapter 2.1.2.2), the SEM collects an image of the block face and the resin block is cut by an ultramicrotome that is mounted inside the vacuum chamber of the SEM exposing the next layer to be imaged 15-200 nm below the surface. It was intended to image the cell after incubation with gold NPs to show the 3D distribution of the NPs and then to show the damage to whole cells after irradiation. The difficulty of this technique is the requirement to stain the sample with heavy metals during processing, multiple attempts were made to process the cells, but aggregation of the chemicals always occurred and this made it impossible to image the cell by SEM.

Finally, to establish the basics for a cancer therapy, evaluate whether findings can be used in therapy by developing an appropriate animal model.

References

1. D. Dolmans, D. Fukumura and R. K. Jain, *Nat. Rev. Cancer*, 2003, **3**, 380-387.

2. P. Agostinis, K. Berg, K. A. Cengel, T. H. Foster, A. W. Girotti, S. O. Gollnick, S. M. Hahn, M. R. Hamblin, A. Juzeniene, D. Kessel, M. Korbelik, J. Moan, P. Mroz, D. Nowis, J. Piette, B. C. Wilson and J. Golab, *Ca-a Cancer Journal for Clinicians*, 2011, **61**, 250-281.

3. M. C. DeRosa and R. J. Crutchley, *Coord. Chem. Rev.*, 2002, **233**, 351-371.

4. A. B. Ormond and H. S. Freeman, *Materials*, 2013, **6**, 817-840.

5. M. O. Senge and J. C. Brandt, *Photochem. Photobiol.*, 2011, **87**, 1240-1296.

6. P. K. Jain, I. H. El-Sayed and M. A. El-Sayed, *Nano Today*, 2007, **2**, 18-29.

7. E. C. Dreaden, M. A. Mackey, X. Huang, B. Kang and M. A. El-Sayed, *Chem. Soc. Rev.*, **40**, 3391-3404.

8. I. H. El-Sayed, X. H. Huang and M. A. El-Sayed, *Cancer Letters*, 2006, **239**, 129-135.

9. I. H. El-Sayed, X. H. Huang and M. A. El-Sayed, *Nano Letters*, 2005, **5**, 829-834.

10. K. L. Kelly, E. Coronado, L. L. Zhao and G. C. Schatz, *Journal of Physical Chemistry B*, 2003, **107**, 668-677.

11. P. Mulvaney, *Langmuir*, 1996, **12**, 788-800.

12. S. Link and M. A. Ei-Sayed, *Annual Review of Physical Chemistry*, 2003, **54**, 331-366.

13. G. Mie, *Annalen Der Physik*, 1908, **25**, 377-445.

14. S. Link and M. A. El-Sayed, *Journal of Physical Chemistry B*, 1999, **103**, 4212-4217.

15. S. Link and M. A. El-Sayed, *J. Phys. Chem. B*, 1999, **103**, 8410-8426.

16. P. K. Jain, K. S. Lee, I. H. El-Sayed and M. A. El-Sayed, *J. Phys. Chem. B*, 2006, **110**, 7238-7248.

17. S. Underwood and P. Mulvaney, *Langmuir*, 1994, **10**, 3427-3430.

18. C. Burda, X. B. Chen, R. Narayanan and M. A. El-Sayed, *Chemical Reviews*, 2005, **105**, 1025-1102.

19. L. M. Liz-Marzan, *Langmuir*, 2006, **22**, 32-41.

20. C. J. Murphy, T. K. San, A. M. Gole, C. J. Orendorff, J. X. Gao, L. Gou, S. E. Hunyadi and T. Li, *J. Phys. Chem. B*, 2005, **109**, 13857-13870.

21. A. P. Castano, T. N. Demidova and M. R. Hamblin, *Photodiagnosis and Photodynamic Therapy*, 2004, **1**, 279-293.

22. P. Agostinis, K. Berg, K. A. Cengel, T. H. Foster, A. W. Girotti, S. O. Gollnick, S. M. Hahn, M. R. Hamblin, A. Juzeniene, D. Kessel, M. Korbelik, J. Moan, P. Mroz, D. Nowis, J. Piette, B. C. Wilson and J. Golab, *Ca-a Cancer Journal for Clinicians*, **61**, 250-281.

23. R. A. Sperling, P. Rivera gil, F. Zhang, M. Zanella and W. J. Parak, *Chem. Soc. Rev.*, 2008, **37**, 1896-1908.

24. E. Boisselier and D. Astruc, *Chem. Soc. Rev.*, 2009, **38**, 1759-1782.

25. J. Turkevich, P. C. Stevenson and J. Hillier, *Discussions of the Faraday Society*, 1951, 55-&.

26. G. Frens, *Nature-Physical Science*, 1973, **241**, 20-22.

27. M. C. Daniel and D. Astruc, *Chemical Reviews*, 2004, **104**, 293-346.

28. C. Loo, A. Lowery, N. J. Halas, J. West and R. Drezek, *Nano Lett.*, 2005, **5**, 709-711.

29. E. E. Connor, J. Mwamuka, A. Gole, C. J. Murphy and M. D. Wyatt, *Small*, 2005, **1**, 325-327.

30. C. Brandenberger, B. Rothen-Rutishauser, C. Muhlfeld, O. Schmid, G. A. Ferron, K. L. Maier, P. Gehr and A. G. Lenz, *Toxicol. Appl. Pharmacol.*, 2010, **242**, 56-65.

31. C. J. Murphy, A. M. Gole, J. W. Stone, P. N. Sisco, A. M. Alkilany, E. C. Goldsmith and S. C. Baxter, *Accounts Chem. Res.*, 2008, **41**, 1721-1730.

32. Y. Pan, S. Neuss, A. Leifert, M. Fischler, F. Wen, U. Simon, G. Schmid, W. Brandau and W. Jahnen-Dechent, *Small*, 2007, **3**, 1941-1949.

33. B. D. Chithrani, A. A. Ghazani and W. C. W. Chan, *Nano Lett.*, 2006, **6**, 662-668.

34. J. Rejman, V. Oberle, I. S. Zuhorn and D. Hoekstra, *Biochem. J.*, 2004, **377**, 159-169.

35. C. Brandenberger, C. Muehlfeld, Z. Ali, A.-G. Lenz, O. Schmid, W. J. Parak, P. Gehr and B. Rothen-Rutishauser, *Small*, 2010, **6**, 1669-1678.

36. F. Zhao, Y. Zhao, Y. Liu, X. Chang, C. Chen and Y. Zhao, *Small*, 2011, **7**, 1322-1337.

37. S. D. Conner and S. L. Schmid, *Nature*, 2003, **422**, 37-44.

38. G. J. Doherty and H. T. McMahon, in *Annual Review of Biochemistry*, Annual Reviews, Palo Alto, Editon edn., 2009, vol. 78, pp. 857-902.

39. J. M. Besterman and R. B. Low, *The Biochemical Journal*, 1983, **210**, 1-13.

40. S. Link and M. A. El-Sayed, *International Reviews in Physical Chemistry*, 2000, **19**, 409-453.

41. H. Hovel, S. Fritz, A. Hilger, U. Kreibig and M. Vollmer, *Physical Review B*, 1993, **48**, 18178-18188.

42. C. M. Pitsillides, E. K. Joe, X. B. Wei, R. R. Anderson and C. P. Lin, *Biophysical Journal*, 2003, **84**, 4023-4032.

43. V. P. Zharov, V. Galitovsky and M. Viegas, *Applied Physics Letters*, 2003, **83**, 4897-4899.

44. J. F. Hainfeld, D. N. Slatkin and H. M. Smilowitz, *Phys. Med. Biol.*, 2004, **49**, N309-N315.

45. V. P. Zharov, E. N. Galitovskaya, C. Johnson and T. Kelly, *Lasers Surg. Med.*, 2005, **37**, 219-226.

46. X. H. Huang, P. K. Jain, I. H. El-Sayed and M. A. El-Sayed, *Photochemistry and Photobiology*, 2006, **82**, 412-417.

47. X. Huang, I. H. El-Sayed, W. Qian and M. A. El-Sayed, *Journal of the American Chemical Society*, 2006, **128**, 2115-2120.

48. V. Raji, J. Kumar, C. S. Rejiya, M. Vibin, V. N. Shenoi and A. Abraham, *Experimental Cell Research*, 2011, **317**, 2052-2058.

49. T. B. Huff, L. Tong, Y. Zhao, M. N. Hansen, J. X. Cheng and A. Wei, *Nanomedicine*, 2007, **2**, 125-132.

50. L. R. Hirsch, R. J. Stafford, J. A. Bankson, S. R. Sershen, B. Rivera, R. E. Price, J. D. Hazle, N. J. Halas and J. L. West, *Proc. Natl. Acad. Sci. U. S. A.*, 2003, **100**, 13549-13554.

51. J. Kim, S. Park, J. E. Lee, S. M. Jin, J. H. Lee, I. S. Lee, I. Yang, J. S. Kim, S. K. Kim, M. H. Cho and T. Hyeon, *Angew. Chem.-Int. Edit.*, 2006, **45**, 7754-7758.

52. J. Y. Chen, C. Glaus, R. Laforest, Q. Zhang, M. X. Yang, M. Gidding, M. J. Welch and Y. N. Xia, *Small*, 2010, **6**, 811-817.

53. D. P. O'Neal, L. R. Hirsch, N. J. Halas, J. D. Payne and J. L. West, *Cancer Lett.*, 2004, **209**, 171-176.

54. J. L. Li, D. Day and M. Gu, *Advanced Materials*, 2008, **20**, 3866-+.

55. Z. Krpetic, P. Nativo, V. See, I. A. Prior, M. Brust and M. Volk, *Nano Lett.*, 2010, **10**, 4549-4554.

56. M. Hu and G. V. Hartland, *Journal of Physical Chemistry B*, 2002, **106**, 7029-7033.

57. G. Pasparakis, *Small*, 2013, **9**, 4130-4134.

58. R. Vankayala, A. Sagadevan, P. Vijayaraghavan, C.-L. Kuo and K. C. Hwang, *Angew. Chem.-Int. Edit.*, 2011, **50**, 10640-10644.

59. T. T. Zhao, X. Q. Shen, L. Li, Z. P. Guan, N. Y. Gao, P. Y. Yuan, S. Q. Yao, Q. H. Xu and G. Q. Xu, *Nanoscale*, 2012, **4**, 7712-7719.

60. R. Vankayala, Y.-K. Huang, P. Kalluru, C.-S. Chiang and K. C. Hwang, *Small*, 2014, **10**, 1612-1622.

61. R. Vankayala, C.-C. Lin, P. Kalluru, C.-S. Chiang and K. C. Hwang, *Biomaterials*, 2014, **35**, 5527-5538.

62. T. Mironava, M. Hadjiargyrou, M. Simon, V. Jurukovski and M. H. Rafailovich, *Nanotoxicology*, 2010, **4**, 120-137.

63. G. Maiorano, S. Sabella, B. Sorce, V. Brunetti, M. A. Malvindi, R. Cingolani and P. P. Pompa, *ACS Nano*, **4**, 7481-7491.

64. N. G. Bastus, J. Comenge and V. Puntes, *Langmuir*, 2011, **27**, 11098-11105.

65. S. K. Sivaraman, S. Kumar and V. Santhanam, *J. Colloid Interface Sci.*, 2011, **361**, 543-547.

66. Z. Krpetic, A. M. Davidson, M. Volk, R. Levy, M. Brust and D. L. Cooper, *ACS Nano*, **7**, 8881-8890.

67. R. Levy, N. T. K. Thanh, R. C. Doty, I. Hussain, R. J. Nichols, D. J. Schiffrin, M. Brust and D. G. Fernig, *Journal of the American Chemical Society*, 2004, **126**, 10076-10084.

68. D. A. Giljohann, D. S. Seferos, W. L. Daniel, M. D. Massich, P. C. Patel and C. A. Mirkin, *Angew. Chem., Int. Ed.*, **49**, 3280-3294.

69. P. Nativo, I. A. Prior and M. Brust, *ACS Nano*, 2008, **2**, 1639-1644.

70. W. Haiss, N. T. K. Thanh, J. Aveyard and D. G. Fernig, *Anal. Chem. (Washington, DC, U. S.)*, 2007, **79**, 4215-4221.

71. V. See, P. Free, Y. Cesbron, P. Nativo, U. Shaheen, D. Rigden, D. G. Spiller, D. G. Fernig, M. R. H. White, I. A. Prior, M. Brust, B. Lounis and R. Levy, *ACS Nano*, 2009, **3**, 2461-2468.

72. P. B. Merkel and D. R. Kearns, *Journal of the American Chemical Society*, 1972, **94**, 7244-&.

73. A. Gomes, E. Fernandes and J. Lima, *Journal of Biochemical and Biophysical Methods*, 2005, **65**, 45-80.

74. W. Spiller, H. Kliesch, D. Wohrle, S. Hackbarth, B. Roder and G. Schnurpfeil, *Journal of Porphyrins and Phthalocyanines*, 1998, **2**, 145-158.

75. I. B. Matheson, J. Lee, Yamanash.Bs and Wolbarsh.Ml, *Journal of the American Chemical Society*, 1974, **96**, 3343-3348.

76. G. V. Hartland, *Chem. Rev.*, 2011, **111**, 3858-3887.

77. E. B. Dickerson, E. C. Dreaden, X. H. Huang, I. H. El-Sayed, H. H. Chu, S. Pushpanketh, J. F. McDonald and M. A. El-Sayed, *Cancer Lett.*, 2008, **269**, 57-66.

78. X.-F. Zhang and X. Li, *Journal of Luminescence*, 2011, **131**, 2263-2266.

79. A. Singh, N. R. McIntyre and G. W. Koroll, *Photochemistry and Photobiology*, 1978, **28**, 595-601.

80. M. Fujii, M. Usui, S. Hayashi, E. Gross, D. Kovalev, N. Kunzner, J. Diener and V. Y. Timoshenko, *Journal of Applied Physics*, 2004, **95**, 3689-3693.

81. J. H. Hodak, A. Henglein and G. V. Hartland, *Journal of Physical Chemistry B*, 2000, **104**, 9954-9965.

82. A. Takami, H. Kurita and S. Koda, *Journal of Physical Chemistry B*, 1999, **103**, 1226-1232.

83. V. Kotaidis, C. Dahmen, G. von Plessen, F. Springer and A. Plech, *J. Chem. Phys.*, 2006, **124**, 7.

84. A. Siems, S. A. L. Weber, J. Boneberg and A. Plech, *New Journal of Physics*, 2011, **13**.

85. D. Kovalev and M. Fujii, *Advanced Materials*, 2005, **17**, 2531-2544.

86. Z. Lin, L. V. Zhigilei and V. Celli, *Phys. Rev. B*, 2008, **77**, 17.

87. A. G. Tkachenko, H. Xie, D. Coleman, W. Glomm, J. Ryan, M. F. Anderson, S. Franzen and D. L. Feldheim, *Journal of the American Chemical Society*, 2003, **125**, 4700-4701.

Appendix 2

A2.1: ICP-AES: Determination of Intracellular Gold Content – Results

Citrate Gold Nanoparticles – 3 hours

	Dish Size	AES Result (ppb)	Number of Cells	No. NPs	NPs/Cell
1	35mm	170	*585,000*	2.60E+10	44,484
2	35mm	157	*635,000*	2.40E+10	37,847
3	35mm	200	*715,000*	3.06E+10	42,819
4	35mm	164	*570,000*	2.51E+10	44,043
5	100mm	1159	*4,360,000*	1.77E+11	40,692
6	100mm	1152	*5,750,000*	2.18E+11	37,831
7	100mm	1185	*4,720,000*	2.24E+11	47,406
8	100mm	1221	*5,170,000*	2.31E+11	44,595
9	100mm	972	*3,650,000*	1.49E+11	40,765
10	100mm	920	*3,450,000*	1.41E+11	40,820
11	100mm	922	*3,500,000*	1.41E+11	40,325

Table A2.1: The number of NPs per cell calculated from the gold content analysed by ICP-AES after HeLa cell incubation with 13 – 15 nm citrate gold NPs at a final incubation concentration of 2 nM and an incubation time of 3 hours

Citrate Gold Nanoparticles – 24 hours

	Dish Size	AES Result (ppb)	Number of Cells	No. NPs	NPs/Cell
1	100mm	12204	*6,000,000*	1.87E+12	311,358
2	100mm	12878	*4,770,000*	1.97E+12	413,275
3	100mm	12734	*5,670,000*	1.95E+12	343,788
4	100mm	8378	*4,375,000*	1.58E+12	361,595
5	100mm	9178	*6,000,000*	1.73E+12	288,840
6	100mm	7430	*4,770,000*	1.40E+12	294,124
7	100mm	6770	*5,675,000*	1.28E+12	225,259

Table A2.2: The number of NPs per cell calculated from the gold content analysed by ICP-AES after HeLa cell incubation with 13 – 15 nm citrate gold NPs at a final incubation concentration of 2 nM and an incubation time of 24 hours

CALNN Gold Nanoparticles – 3 hours (2 nM)

	Dish Size	AES Result (ppb)	Number of Cells	No. NPs	NPs/Cell
1	35mm	181	*655,000*	4.60E+10	70,211
2	35mm	186	*655,000*	4.73E+10	72,150
3	35mm	159	*655,000*	4.04E+10	61,677
4	35mm	120	*400,000*	3.05E+10	76,223
5	35mm	143	*400,000*	3.63E+10	90,833
6	35mm	124	*400,000*	3.15E+10	78,764
7	35mm	123	*400,000*	3.13E+10	78,129

Table A2.3: The number of NPs per cell calculated from the gold content analysed by ICP-AES after HeLa cell incubation with 13 – 15 nm CALNN gold NPs at a final incubation concentration of 2 nM and an incubation time of 3 hours

CALNN Gold Nanoparticles – 3 hours (4 nM)

	Dish Size	AES Result (ppb)	Number of Cells	No. NPs	NPs/Cell
1	35mm	695	400,000	1.06E+11	265,971
2	35mm	664	365,000	1.02E+11	278,474
3	35mm	298	*273,055*	4.56E+10	167,061
4	35mm	376	*301,419*	5.76E+10	190,953
5	35mm	375	*273,517*	5.74E+10	209,873

Table A2.4: The number of NPs per cell calculated from the gold content analysed by ICP-AES after HeLa cell incubation with 13 -1 5 nm CALNN gold NPs at a final incubation concentration of 4 nM and an incubation time of 3 hours

CALNN Gold Nanoparticles – 24 hours (4 nM)

	Dish Size	AES Result (ppb)	Number of Cells	No. NPs	NPs/Cell
1	35mm	1964	*520,000*	3.01E+11	578,159
2	35mm	2145	*540,000*	3.28E+11	608,055

Table A2.3: The number of NPs per cell calculated from the gold content analysed by ICP-AES after HeLa cell incubation with 13 – 15 nm CALNN gold NPs at a final incubation concentration of 4 nM and an incubation time of 24 hours

Appendix 3

A3.1 Citrate Gold Nanoparticle Irradiation Results

3 hour Incubation (Citrate Gold NPs)

			Centre (0.5 mm diam.)			
Power	**Exposure Time**	**Area**	**No. of Cells**	**Fraction of cells dead(%)**	**Calc. Abs. (mOD)**	**Max. Temp. (°C)**
1 W	3 min	A1	150	0	1.5	25
1 W	3 min	A2	158	0	1.6	25
1 W	5 min	A1	106	22	1.1	24
1 W	5 min	A2	77	35	0.8	23
1 W	5 min	A1	151	26	1.5	25
1 W	5 min	A1	73	26	0.7	23
1 W	5 min	A2	98	32	1.0	24
1.5 W	3 min	A1	168	24	1.7	26
1.5 W	3 min	A2	161	37	1.6	26
1.5 W	3 min	A3	194	9	2.0	27
1.5 W	5 min	A1	111	33	1.1	25
1.5 W	5 min	A2	89	52	0.9	24
1.5 W	5 min	A1	107	59	1.1	25
1.5 W	5 min	A2	72	40	0.7	24
1.5 W	5 min	A1	148	59	1.5	26
1.5 W	5 min	A2	230	33	2.3	28
1.5 W	5 min	A1	100	47	1.0	25
1.5 W	5 min	A2	112	46	1.1	25
2 W	2 min	A1	75	11	0.8	24
2 W	2 min	A2	55	33	0.6	24
2 W	3 min	A1	90	28	0.9	25
2 W	3 min	A2	84	35	0.8	25
2 W	3 min	A3	84	42	0.8	25
2 W	4 min	A1	68	47	0.9	25
2 W	4 min	A2	58	40	0.6	24
2 W	4 min	A3	86	58	0.9	25
2 W	5 min	A1	83	24	0.8	25
2 W	5 min	A2	91	43	0.9	25
2 W	5 min	A1	80	63	0.8	25
2 W	5 min	A2	116	90	1.2	26

Figure A3.1(A): fraction of dead cells at 24 hours after laser exposure for HeLa cells incubated with citrate gold NPs (3 h, 2 nM) and irradiated at given power and exposure times, also given are the calculated absorbance of the samples and the estimated maximum temperature during irradiation

3 hour Incubation (Citrate Gold NPs)

			Centre (0.5 mm diam.)			
Power	**Exposure Time**	**Area**	**No. of Cells**	**Fraction of cells dead(%)**	**Calc. Abs. (mOD)**	**Max. Temp. (°C)**
3 W	1 min	A1	128	0	1.3	28
3 W	1 min	A2	203	0	2.0	32
3 W	3 min	A1	160	28	0.1	30
3 W	3 min	A2	152	54	0.1	30
3 W	3 min	A3	120	42	0.1	28
3 W	3 min	B1	188	28	0.1	32
3 W	3 min	B2	162	66	0.1	30
3 W	3 min	B3	234	0	0.0	34
3 W	3 min	C1	206	69	0.1	33
3 W	3 min	C2	220	39	0.1	33
3 W	3 min	C3	120	93	0.2	28
3 W	3 min	D1	159	61	0.1	30
3 W	3 min	D2	207	0	0.0	33
3 W	3 min	D3	134	79	0.2	29
3 W	3 min	E1	151	100	0.2	30
3 W	3 min	E2	121	60	0.1	28
3 W	3 min	E3	141	74	0.1	29
3 W	3 min	F1	125	67	0.1	28
3 W	3 min	F2	138	50	0.1	29
3 W	3 min	F3	93	68	0.1	27
3 W	5 min	A1	134	100	1.4	29
3 W	5 min	A2	183	100	1.8	32

Figure A3.1(B): Fraction of dead cells at 24 hours after laser exposure for HeLa cells incubated with citrate gold NPs (3 h, 2 nM) and irradiated at 3 W power and given exposure times, also given are the calculated absorbance of the samples and the estimated maximum temperature during irradiation

24 hour Incubation (Citrate gold NPs)

	Centre (0.5 mm diam.)					
Area	No. of Cells	Fraction of cells dead(%)	Diam. of Area of Dead Cells (mm)	Calc. Abs. (mOD)	Max. Temp. (°C)	Temp. at the Edge of Area of Dead Cells (°C)
A1	237	100	1.0	15.4	100	74
A2	115	100	0.9	7.5	60	52
A3	168	100	1.2	10.9	78	57
B1	173	100	1.1	11.2	80	66
B2	179	100	0.9	11.6	82	68
B3	171	100	0.8	11.1	79	66
C1	96	100	1.0	6.2	54	40
C2	80	100	1.0	5.2	49	40
C3	155	100	1.1	10.0	74	54
D1	165	100	1.0	10.7	77	64
D2	230	100	1.0	14.9	99	73
D3	154	100	1.1	10.0	73	56
E1	144	100	1.0	9.3	70	54
E2	93	100	1.1	6.0	53	43
E3	212	100	1.2	13.7	93	69
F1	137	100	1.0	8.9	68	55
F2	231	100	1.1	15.0	99	73
F3	222	100	1.2	14.4	96	67

Table A3.2: Fraction of dead cells in the centre of the laser beam and the diameter of the well-defined are of dead cells at 24 hours after laser exposure for HeLa cells incubated with citrate gold NPs (24 h, 2 nM) and irradiated (3 W, 3 min). The calculated absorbance of the cell monolayer, the estimated maximum temperature and the temperature at the edge of the area of dead cells during irradiation is also given.

A3.2 CALNN Gold Nanoparticle Irradiation Results

1 W 3 min (CALNN Gold NPs)

	Centre 0.2mm^2					
Area	Number of Cells	Number of Dead Cells (%)	Diam. of Area of Dead Cells (mm)	Calculated Absorbance (mOD)	Max. Temp. (°C)	Temp. at the Edge of Area of Dead Cells (°C)
A1	110	0	-	5.8	32	-
A2	142	0	-	7.5	35	-
A3	164	0	-	8.7	37	-
A4	121	0	-	6.4	33	-
B1	111	0	-	5.9	32	-
B2	119	0	-	6.3	33	-
B3	212	0	-	11.2	41	-
B4	106	0	-	5.6	32	-
C1	191	0	-	10.1	39	-
C2	185	0	-	9.8	39	-
C3	149	0	-	7.9	36	-
D1	56	0	-	3.0	27	-
D2	92	0	-	4.9	30	-
D3	70	0	-	3.7	28	-
E1	149	0	-	7.9	36	-
E2	223	0	-	11.8	42	-
E3	157	0	-	8.3	36	-
F1	76	0	-	4.0	29	-
F2	60	0	-	3.2	27	-
F3	79	0	-	4.2	29	-
F4	65	0	-	3.4	28	-

Table A3.3: Results and estimated temperature rise for irradiation (1 W 3 min) of HeLa cells after incubation with CALNN gold NPs (3h, 4 nM). The fraction of dead cells in the centre of the irradiated area and the diameter of the well-defined area of dead cells determined at 24 hours after irradiation is given. The calculated absorbance of the cell monolayer, the estimated maximum temperature and the temperature at the edge of the area of dead cells during irradiation is also given

3h 1.0W 5m (CALNN Gold NPs)

	Centre (0.5 mm diam.)					
Area	No. of Cells	Fraction of cells dead(%)	Diam. of Area of Dead Cells (mm)	Calc. Abs. (mOD)	Max. Temp. (°C)	Temp. at the Edge of Area of Dead Cells (°C)
A1	106	0	-	5.6	32	-
A2	146	0	-	7.7	36	-

Table A3.4: Results and estimated temperature rise for irradiation (1 W 5 min) of HeLa cells after incubation with CALNN gold NPs (3h, 4 nM). The fraction of dead cells in the centre of the irradiated area and the diameter of the well-defined area of dead cells determined at 24 hours after irradiation is given. The calculated absorbance of the cell monolayer, the estimated maximum temperature and the temperature at the edge of the area of dead cells during irradiation is also given

1.5 W 3 min (CALNN Gold NPs)

	Centre 0.2mm^2					
Area	Number of Cells	Number of Dead Cells (%)	Diam. of Area of Dead Cells (mm)	Calculated Absorbance (mOD)	Max. Temp. (°C)	Temp. at the Edge of Area of Dead Cells (°C)
A1	385	100	0.7	20.3	73	69
A2	220	100	0.5	11.6	51	47
A3	213	100	0.5	11.2	50	46
B1	133	0	-	7.0	40	-
B2	122	0	-	6.4	38	-
B3	92	0	-	4.9	34	-
B4	66	0	-	3.5	31	-

Table A3.5: Results and estimated temperature rise for irradiation (1.5 W 3 min) of HeLa cells after incubation with CALNN gold NPs (3h, 4 nM). The fraction of dead cells in the centre of the irradiated area and the diameter of the well-defined area of dead cells determined at 24 hours after irradiation is given. The calculated absorbance of the cell monolayer, the estimated maximum temperature and the temperature at the edge of the area of dead cells during irradiation is also given

2 W 3 min (CALNN Gold NPs)

	Centre 0.2mm^2					
Area	Number of Cells	Number of Dead Cells (%)	Diam. of Area of Dead Cells (mm)	Calculated Absorbance (mOD)	Max. Temp. (°C)	Temp. at the Edge of Area of Dead Cells (°C)
A1	113	100	0.5	6.0	42	31
A2	158	0	-	8.3	50	-
A3	162	100	0.5	8.6	51	34
A4	84	0	-	4.4	37	-
B1	270	100	0.8	14.3	70	40
B2	275	100	0.6	14.5	71	43
B3	204	100	0.5	10.8	59	38
B4	130	0	-	6.9	45	-
C1	91	0	-	4.8	38	-
C2	195	7	0.2	10.3	57	38
D1	176	100	0.5	9.3	54	36
D2	110	0	-	5.8	42	-
D3	178	57	0.4	9.4	54	36
D4	113	0	-	6.0	42	
E1	49	0	-	2.6	31	-
E2	95	0	-	5.0	39	-
E3	62	0	-	3.3	33	-
E4	87	0	-	4.6	38	-
F1	116	0	-	6.1	43	-
F2	59	0	-	3.1	33	-
F3	96	0	-	5.1	39	-
F4	105	0	-	5.5	41	-

Table A3.6: Results and estimated temperature rise for irradiation (2 W 3 min) of HeLa cells after incubation with CALNN gold NPs (3h, 4 nM). The fraction of dead cells in the centre of the irradiated area and the diameter of the well-defined area of dead cells determined at 24 hours after irradiation is given. The calculated absorbance of the cell monolayer, the estimated maximum temperature and the temperature at the edge of the area of dead cells during irradiation is also given

3h 3.0W 1m (CALNN Gold NPs)

	Centre (0.5 mm diam.)					
Area	No. of Cells	Fraction of cells dead(%)	Diam. of Area of Dead Cells (mm)	Calc. Abs. (mOD)	Max. Temp. (°C)	Temp. at the Edge of Area of Dead Cells (°C)
A1	275	100	0.8	14.5	90	77
A2	275	100	1.0	14.5	90	73
B2	275	100	0.8	14.5	90	78
B3	275	100	0.7	14.5	90	80
C1	233	100	0.8	12.3	80	69
C2	230	100	0.7	12.1	79	71
D1	188	100	0.7	9.9	69	64
D2	126	100	0.6	6.7	53	50
D3	235	100	0.6	12.4	80	75
E1	105	100	0.8	5.5	48	44
E2	145	100	0.6	7.7	58	54
E3	129	100	0.5	6.8	54	52
F1	246	100	0.6	13.0	83	76
F2	209	100	0.5	11.0	74	70
F3	196	100	0.8	10.3	71	63
F4	252	100	0.5	13.3	84	79
G1	65	0	-	3.4	38	-
G2	30	0	-	1.6	30	-
H1	94	0	-	5.0	45	-
H2	94	0	-	5.0	45	-
I1	57	0	-	3.0	36	-
I2	79	0	-	4.2	42	-

Table A3.7: Results and estimated temperature rise for irradiation (3 W 1 min) of HeLa cells after incubation with CALNN gold NPs (3h, 4 nM). The fraction of dead cells in the centre of the irradiated area and the diameter of the well-defined area of dead cells determined at 24 hours after irradiation is given. The calculated absorbance of the cell monolayer, the estimated maximum temperature and the temperature at the edge of the area of dead cells during irradiation is also given

3h 3.0W 2m (CALNN Gold NPs)

	Centre (0.5 mm diam.)					
Area	**No. of Cells**	**Fraction of cells dead(%)**	**Diam. of Area of Dead Cells (mm)**	**Calc. Abs. (mOD)**	**Max. Temp. (°C)**	**Temp. at the Edge of Area of Dead Cells (°C)**
A1	229	92	0.8	12.1	82	53
A2	219	100	0.9	11.6	79	48
B1	136	100	1.0	7.2	58	49
B2	152	100	0.7	8.0	62	46
B3	121	100	1.0	6.4	54	46
B4	165	100	0.5	8.7	65	55

Table A3.8: Results and estimated temperature rise for irradiation (3 W 2 min) of HeLa cells after incubation with CALNN gold NPs (3h, 4 nM). The fraction of dead cells in the centre of the irradiated area and the diameter of the well-defined area of dead cells determined at 24 hours after irradiation is given. The calculated absorbance of the cell monolayer, the estimated maximum temperature and the temperature at the edge of the area of dead cells during irradiation is also given

3 W 3 min (CALNN Gold NPs)

	Centre (0.5 mm diam.)					
Area	**No. of Cells**	**Fraction of cells dead(%)**	**Diam. of Area of Dead Cells (mm)**	**Calc. Abs. (mOD)**	**Max. Temp. (°C)**	**Temp. at the Edge of Area of Dead Cells (°C)**
A1	118	100	1.3	6.2	54	43
A2	148	100	1.1	7.8	62	52
A3	158	100	1.1	8.3	64	53
A4	158	100	1.2	8.3	64	52
B1	124	100	1.0	6.5	55	48
B2	86	100	0.8	4.5	45	41
C1	294	100	1	15.5	100	75
C2	178	100	0.1	9.4	70	59
C3	168	100	1.2	8.9	67	54
D1	97	100	1.1	5.1	48	42
D2	174	100	1.2	9.2	69	55
E1	145	100	1.1	7.7	61	51
E2	108	100	1.2	5.7	51	43
E3	206	100	1.2	10.9	77	61
E4	172	100	1.2	9.1	68	55
F1	148	100	1.05	7.8	62	52
F2	88	100	0.1	4.6	46	40
F3	202	100	0.9	10.7	76	66
F4	178	100	0.8	9.4	70	62
G1	117	100	0.7	6.2	54	49

Table A3.8: Results and estimated temperature rise for irradiation (3 W 3 min) of HeLa cells after incubation with CALNN gold NPs (3h, 4 nM). The fraction of dead cells in the centre of the irradiated area and the diameter of the well-defined area of dead cells determined at 24 hours after irradiation is given. The calculated absorbance of the cell monolayer, the estimated maximum temperature and the temperature at the edge of the area of dead cells during irradiation is also given

Appendix 4

A4.1 Heat Dissipation Dynamics during Irradiation with Nanosecond Laser Pulses

Irradiation of spherical gold NPs at 532 nm results in highly excited non-thermal electrons ("primary hot electrons") which equilibrate with a time constant of less than 500 fs to yield a Fermi distribution corresponding to an elevated temperature ("hot electrons").[1-3] After excitation with femtosecond laser pulses, the hot electrons lose their energy on the time scale of a few picoseconds by interaction with the lattice (electron-phonon scattering).[1, 2] Because the lattice heat capacity is much larger than the electronic heat capacity, this leaves the electrons and the lattice in equilibrium at a temperature which is significantly lower than the initial electronic temperature and cooling occurs by heat transfer to the solvent and heat diffusion on the time scale of 10 to a few 100 picoseconds, strongly depending on the size of the nanoparticle.[4] Excitation with a nanosecond laser pulse, on the other hand, yields a highly non-equilibrium situation during the duration of the laser pulse, since energy is continuously deposited into the electrons and at the same time heat flows through the lattice into the surrounding solvent. This makes it difficult to predict the temperature of the hot electrons achieved in such experiments, which determines the efficiency of any hot-electron induced chemical reaction.

Here, we used the standard "two-temperature model" for the conduction band electrons and the lattice,[1, 2, 5, 6] coupled to finite-element heat transfer and diffusion simulations in the surrounding solvent to estimate this temperature. This model assumes electron and lattice temperatures which are homogeneous over the nanoparticle. Laser excitation, electron-phonon scattering and heat transfer into the solvent change the energies, E_e and E_l, and hence the temperatures, T_e and T_l, of the electrons and the lattice with time, t, according to

$$\frac{\partial E_e}{\partial t} = c_e(T_e) V_{NP} \frac{\partial T_e}{\partial t} = \sigma_{NP} I_{laser}(t) - g V_{NP}(T_e - T_l)$$
$$\frac{\partial E_l}{\partial t} = c_l V_{NP} \frac{\partial T_l}{\partial t} = g V_{NP}(T_e - T_l) - A_{NP} G(T_l - T_s(R_{NP})) \quad \text{(A4.1)}$$

Here, $c_e(T_e) = \gamma\ T_e$ (with γ = 66 $Jm^{-3}K^{-2}$)[1, 2, 5, 6] and c_l = 2.49 10^6 $Jm^{-3}K^{-1}$ denote the heat capacities of the electrons and the lattice, V_{NP}, A_{NP}, and R_{NP} the volume, surface area and radius of the nanoparticle, respectively, g = 2.95 10^{16} $Wm^{-3}K^{-1}$ the gold electron-phonon coupling constant, G = 110 10^6 $Wm^{-2}K^{-1}$ the thermal conductance at the gold-water interface for citrate-stabilised nanoparticles,[2] and $T_s(R_{NP})$ the temperature of the solvent layer which is in contact with the nanoparticle. The time-dependent laser light intensity $I_{laser}(t)$ (in Wm^{-2}) is assumed to have a Gaussian temporal profile with a half-width given by the laser pulse width and a time-integrated intensity corresponding to the experimental pulse energy density (0.15 J cm^{-2} in our experiments). The nanoparticle absorption cross section, σ_{NP}, was calculated from the size-dependent extinction coefficient.[7]

Finally, the heat deposited into the first solvent layer diffuses outward into the solvent, as described by Fourier heat equation,

$$c_s \frac{\partial T_s(r)}{\partial t} = \kappa \nabla^2 T_s(r) + \frac{dq}{dt} \quad \text{(A4.2)}$$

where $T_s(r)$ denotes the temperature of the solvent at a distance r from the center of the nanoparticle, c_s the heat capacity of the water/ethanol mixture,[8] and κ its heat conductivity.[9] The last term represents a source term, which here is due to energy transferred from the nanoparticle, *i.e.* the last term in the second line of Equation A4.1.

The simulations were implemented using a finite-element method with discrete time and spatial steps, making use of the spherical symmetry of the system under consideration. Spatial discretization was only applied to the solvent, since the electron and lattice

temperatures can be assumed to be essentially constant over the nanoparticle due to fast heat transport in metals. The total spatial size was chosen large enough to ensure that no significant temperature increase was observed at the edge of the simulation volume over the integration time; time steps and spatial simulation cell sizes were chosen to be small enough so that further reduction did not affect the results.

A simulation of the electron-phonon relaxation after excitation with laser pulses of ~100 fs pulse length using this method resulted in hot electron relaxation times of 0.6-0.8 ps for low energy pulses, increasing to several picoseconds at higher energies, essentially independent of the NP diameter in the relevant range 10-100 nm, all of which is in good agreement with experimental observations.[2] Similarly, the experimentally observed phonon-phonon relaxation dynamics, which follow a stretched exponential time dependence $\sim \exp(-(t/\tau)^{\beta})$ with a stretching parameter $\beta \sim 0.7$ and time constants τ which are proportional to the square of the NP diameter,[4] are perfectly reproduced, which confirms the validity of the method.

Figure 4.8 (Chapter 4) shows the time-dependent temperatures of the conduction band electrons, lattice, and the first solvent layer calculated for our experiments using ns-laser pulse excitation (spherical NPs with 15 nm diameter, 5 ns laser pulses with 150 mJ/cm^2 intensity, in 50/50 EtOH/water, c_s = 3.55 JK^{-1}cm^{-3} and κ = 0.339 WK^{-1}m^{-1}), as well as for the experiments described in ref. [10] (spherical NPs with 40 nm diameter, 7 ns laser pulses with 30 mJ/cm^2 intensity, in 80/20 EtOH/water, c_s = 2.61 JK^{-1}cm^{-3} and κ = 0.225 WK^{-1}m^{-1}). It can be seen that in both experiments the electrons, the lattice, and even the surrounding solvent reach significant temperatures. Although in our experiments, the laser intensity was larger by a factor of 5, the maximum temperatures achieved are only slightly larger than those simulated for the experiments of ref. [10]. This results from a combination of two effects which slows down the cooling in the latter experiments: (i) heat diffusion away from larger NPs takes longer due to geometric effects of diffusion,[4]

and (ii) the heat capacity and conductivity of a 80/20 EtOH/water mixture are significantly smaller than those of a 50/50 mixture, both of which lead to slower heat diffusion. The consequences of heating nanoparticles to such high temperatures are discussed in more detail in the main text.

A4.2. Hot Electron Density during Irradiation with Nanosecond Laser Pulses

Excitation of an oxygen molecule to the $^1O_2$ state requires a simultaneous transfer of an electron from one of the $2\pi^*$ molecular orbitals on O_2 to a photogenerated hole on the sensitizer and of a hot electron with opposite spin from a high-energy excited sensitizer level to the same or the other $2\pi^*$ orbital (Dexter mechanism). The excitation of conduction band electrons to temperatures exceeding 2000 ^oC means that a significant number have sufficient energy to excite the $^1\Delta$ state of the oxygen molecule, which has an energy of 0.98 eV above the $^3\Sigma$ ground state,[11] and at the same time there is a significant number of holes at the ground state level, compare Figure 4.9 (Chapter 4), thus allowing the generation of $^1O_2$ to take place, provided that the oxygen molecule is within a short distance (< 10 Å) from the NP surface.

The number of hot electrons available at the energy of the $^1\Delta$ level and the number of holes available at the energy of the $^3\Sigma$ level at the electron temperature T_e can be estimated from the Fermi distribution, using the following expressions for $n_{e,1\Delta}(T_e)$, the density of occupied states at the $^1\Delta$ energy, $E_{1\Delta}$, and $n_{h,3\Sigma}(T_e)$, the density of unoccupied states (holes) at the $^3\Sigma$ energy, $E_{3\Sigma}$ (where "density" refers to the number of (un)occupied states per energy interval, in eV^{-1}):

$$n_{e,1\Delta}(T_e) = N \cdot DOS(E_{1\Delta}) \cdot \frac{1}{e^{(E_{1\Delta} - E_F)/kT_e} + 1}$$
$$n_{h,3\Sigma}(T_e) = N \cdot DOS(E_{3\Sigma}) \cdot \left(1 - \frac{1}{e^{(E_{3\Sigma} - E_F)/kT_e} + 1}\right) \quad \text{(A4.3)}$$

Here, N denotes the number of atoms in the NP, $DOS(E)$ is density of states for gold, which has an essentially constant value of ~0.3 eV^{-1} $atom^{-1}$ in the relevant energy range around E_F, [12] and k is the Boltzmann constant.

In the following, E_F will be assumed to be in the middle of the $^1\Delta$-$^3\Sigma$ gap of the oxygen molecule, which means that essentially the same number of hot electrons are available at the $^1\Delta$ energy as there are holes for accepting electrons at the $^3\Sigma$ energy, $n_{e,1\Delta}(T_e) \approx n_{h,3\Sigma}(T_e)$. For example, for a spherical NP with 15 nm diameter (N = 104,000) at an electron temperature of 2100 ^oC (the maximum value of T_e in our experiments, see Figure 4.8-Chapter 4), $n_{e,1\Delta}(T_e) = n_{h,3\Sigma}(T_e)$ = 2600 eV^{-1}, or 260 electrons within an energy interval of 0.1 eV around the ^{1}□ level. Although the exact positioning of the $^1\Delta$ and $^3\Sigma$ levels with respect to E_F significantly affects the values of $n_{e,1\Delta}(T_e)$ and $n_{h,3\Sigma}(T_e)$, it hardly affects the product of the two densities, which is the relevant quantity here since electron transfer of a hot electron from the NP to the oxygen and that of an electron of opposite spin to a hole on the NP occur simultaneously in the Dexter mechanism; shifting E_F from the middle of the $^1\Delta$-$^3\Sigma$ gap as far as to make it coincide either with $E_{1\Delta}$ or $E_{3\Sigma}$ decreases this product by less than a factor of 2 for the temperatures of relevance here.

Using the time-dependence of the electron temperature T_e, calculated as described in the preceding section and shown in Figure 4.8 in Chapter 4, Equation A4.3 can be used to calculate the time-dependence of the density of hot electrons available at the $^1\Delta$ level (and holes at the $^3\Sigma$ level) during a ns-laser pulse, see Figure A4.1. For calculating the number of hot electrons available for transfer to the oxygen $2\pi^*$ molecular orbital which results in the excitation of the $^1\Delta$ state, these values need to be multiplied by the number of gold atoms in the NP and by the width of the $^1\Delta$ state. Although these results do not allow a direct prediction of the quantum yield of $^1O_2$ photogeneration by gold nanoparticles, since neither the width of the $^1\Delta$ or $^3\Sigma$ states, nor the absolute yields for

electron transfer to/from these orbitals are known, they allow a semi-quantitative estimate of the relative yields obtained under different conditions, as shown in the following section, or a comparison with the effect of primary hot electrons, as discussed in detail in the main text.

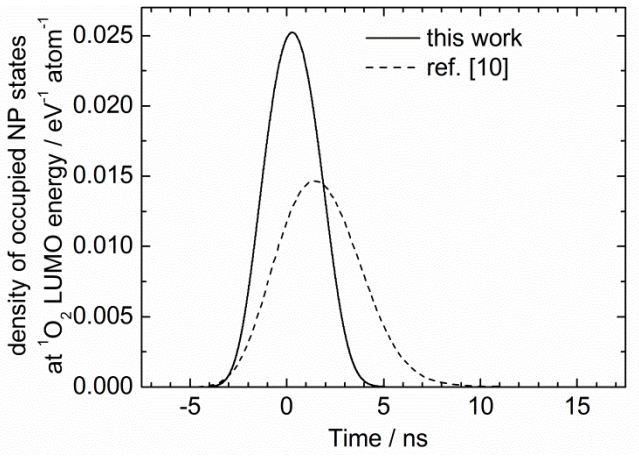

Figure A4.1: Time-dependent density (normalized to the number of gold atoms) of the occupied NP electronic states at the energy of the oxygen $^1\Delta$ state, calculated from the time-dependent electron temperatures shown in Figure 4.8 (Chapter 4), assuming the Fermi level to be in the middle of the $^1\Delta$-$^3\Sigma$ gap. Shown are the results for our experiments using ns-laser pulse excitation (spherical 15 nm NPs in 50/50 EtOH/water, 5 ns laser pulses with 0.15 J cm^{-2} intensity, solid line), and for the experiments described in ref. [10] (spherical 40 nm NPs in 80/20 EtOH/water, 7 ns laser pulses with 0.03 J cm^{-2} intensity, dashed line); time-zero corresponds to the center of the laser pulse. For calculating the number of hot electrons available for transfer to the oxygen, these values need to be multiplied by the number of gold atoms in the NP and by the width of the $^1\Delta$ state.

A4.3. Comparison of the Results of Pulsed Irradiation Observed Here and in Reference [10]

Similar results to those obtained here using pulsed irradiation have recently been reported for spherical gold NPs with 40 nm diameter.[10] Although a significantly lower laser pulse energy density (0.03 J cm^{-2}, compared to 0.15 J cm^{-2} here) was used under otherwise similar experimental conditions, slightly faster $^1O_2$ photogeneration was observed in this study, with the DPBF absorbance decreasing by ~40% over 10 minutes

of irradiation, compared to the ~20% decrease observed here in the first 10 minutes, Figure 4.7(A) – Chapter 4.

The simulations shown in Figure 4.8 (Chapter 4) show that similar electron temperatures are achieved in the two experiments. Figure A4.1 shows that consequently almost the same number of hot electrons are available at the oxygen $^1\Delta$ level during the laser pulse, when normalized to the number of gold atoms, which were almost identical in the two experiments, as indicated by the almost identical absorbance in the Plasmon resonance band.[7] Furthermore, ref. [10] used slightly longer laser pulses than used here, and consequently the integral of the hot electrons at the oxygen $^1\Delta$ level over time yields highly similar values, which are within 10% of each other, which suggests essentially the same efficiency for each NP-O_2 interaction.

For an explicit comparison of the results, all other experimental conditions need to be considered carefully. This includes in particular the number of excitation events, given by the lower pulse repetition rate (1.7 vs. 10 Hz) and larger laser spot size (0.5 vs. 0.1 cm^2) used in ref. [10], as well as the number of oxygen molecules that are expected within reaction distance of a NP surface, given by the smaller total NP surface area of the 40 nm NPs used in ref. [10], compared to the 15 nm NPs used here, and the higher O_2 content of solutions containing more ethanol (approx. a factor of 2.5 for 80% vs. 50% EtOH). Other factors to take into account are the different total sample volume (1 vs. 1.2 mL) and the longer lifetime of $^1O_2$ in solutions containing more ethanol (approx. a factor of 2 for 80% vs. 50% EtOH [13]), which increases the probability of DPBF bleaching by a photogenerated $^1O_2$. Taken together, this predicts that the experiments of ref. [10] should show bleaching of DPBF which is faster by a factor of approx. 1.7 compared to the results presented here. This compares very well with the observed factor 2, with the DPBF absorbance decreasing by ~40% over 10 minutes of irradiation in ref. [10], compared to the ~20% decrease observed here in the first 10 minutes, Figure 4.7(A).

References

1. S. Link and M. A. El-Sayed, *International Reviews in Physical Chemistry*, 2000, **19**, 409-453.

2. G. V. Hartland, *Chem. Rev.*, 2011, **111**, 3858-3887.

3. S. Link and M. A. Ei-Sayed, *Annual Review of Physical Chemistry*, 2003, **54**, 331-366.

4. M. Hu and G. V. Hartland, *Journal of Physical Chemistry B*, 2002, **106**, 7029-7033.

5. S. Link and M. A. El-Sayed, *Journal of Physical Chemistry B*, 1999, **103**, 4212-4217.

6. J. H. Hodak, A. Henglein and G. V. Hartland, *Journal of Physical Chemistry B*, 2000, **104**, 9954-9965.

7. W. Haiss, N. T. K. Thanh, J. Aveyard and D. G. Fernig, *Anal. Chem. (Washington, DC, U. S.)*, 2007, **79**, 4215-4221.

8. G. C. Benson and O. Kiyohara, *J. Solut. Chem.*, 1980, **9**, 791-804.

9. M. J. Assael, E. Charitidou and W. A. Wakeham, *Int. J. Thermophys.*, 1989, **10**, 793-803.

10. G. Pasparakis, *Small*, 2013, **9**, 4130-4134.

11. M. C. DeRosa and R. J. Crutchley, *Coord. Chem. Rev.*, 2002, **233**, 351-371.

12. Z. Lin, L. V. Zhigilei and V. Celli, *Phys. Rev. B*, 2008, **77**, 17.

13. P. B. Merkel and D. R. Kearns, *Journal of the American Chemical Society*, 1972, **94**, 7244-&.